ARCHIVES OF ACOUSTICS
17, 4, 453–510 (1992)

REVIEW OF ACOUSTICAL METHODS OF PROBING THE ATMOSPHERIC BOUNDARY LAYER

J. FORTUNA and E. KOZACZKA

Military Technical Academy
Department of Civil Engineering and Geodesy
(01-489 Warszawa 49)
Naval Academy
(81-929 Gdynia)

The paper presents the review of the methods of remote probing of the lower atmosphere by using the acoustic sounders. Sodar's constructions, their possibilities and usefulness are also presented. By leading to an understanding of the mechanisms underlying the origin of acoustic echoes, sodars provide new insight into the physical processes affecting the lower atmosphere.

1. Introduction

At 1946 GILMAN *et al.* [45] built a precursor of the acoustic sounder, a device acting like an "acoustic radar" which they named the "sodar" for sonic detection and ranging. In the sodar a loudspeaker transmitted sound pulses upwards into the atmosphere, a microphone received the scattered waves and, after filtering and detection, a motion picture camera recorded the display of the received signal on an oscilloscope. Since calculation showed that even in a strong conversion the gradient could not account for the strength of the returned signal, the authors ascribed the scattering of sound to some unknown inhomogeneities or turbulence in the atmosphere.

Pursuit of the same problem, understanding of the radio propagation, induced Mc ALLISTER [80] to return to the earlier concept of the sodar, but with three major changes: a vastly improved transmitting antenna permitting operation just below 1000 Hz and at ranges up to 1.5 km; use of the transmitting antenna itself (with a transmit-receive switching circuit) for the receiver and, perhaps most important, use of the facsimile recorder, adopted from sonar, for the received signal. In the facsimile recorder, each pulse produced a vertical trace whose darkness varies with the received signal strength from a particular height in the atmosphere, a height proportional to the ordinate on the chart. With his new instrument, which he preferred to call an "acoustic sounder" Mc Allister obtained very clear pictures, including one showing the striking presence of internal waves ("gravity waves"). Following Gilman et al. Mc Allister attributed the scattering of the sound waves to "temperature discontinuities" or atmospheric inhomogeneities.

During this period, LITTLE [66] initiated a program at the Wave Propagation Laboratory of the National Oceanic and Atmospheric Administration for the study of optical propagation and remote sensing of the atmosphere by means of laser beams. The program resulted in a new acquaintance with the work of the Russian school, e.g. with the monograph of TATARSKI [104] and the related acoustic studies of KALLISTRATORA [61] and MONIN [82]. In the following year a pair of coordinated papers by LITTLE [67] and MC ALLISTER [83] appeared. Using the turbulent scattering theory, Little for the first time obtained quantitative estimates of the received signal strength, the estimates being in good agreement with later experimental results. Little suggested certain improvements of the echosonde techniques which in addition to the display of atmospheric structure, would give vertical profiles of winds (by using the Doppler effect), three-dimensional spectra of temperature and wind fluctuations, and vertical profiles of humidity (by using a multifrequency system). Later research has followed up all of these suggestions. Figure 1 shows thermal plumes detected by MC ALLISTER [81].

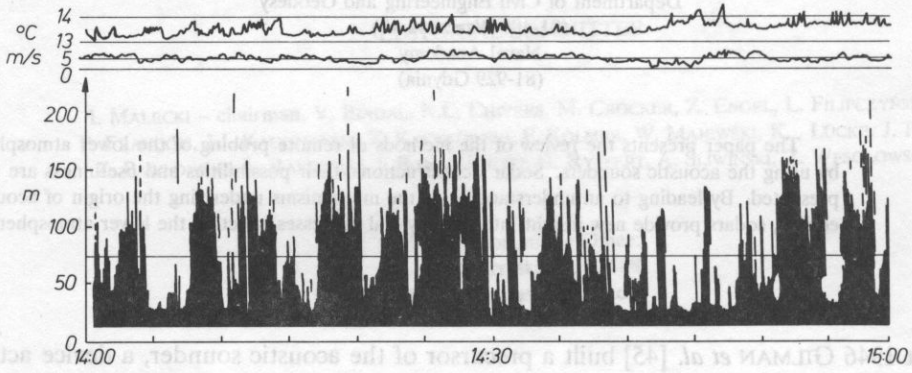

FIG. 1. The first thermal plumes shown by an sodar [81].

2. Propagation of sound in the atmosphere

2.1. Estimating refractive effects in acoustic sounding

Inhomogeneities in the atmospheric wind and temperature fields introduce refractive errors in the measured Doppler shift, in the angular dependence of scatter by irregularities, and in the location of the atmospheric volume. The appoaches to solve the problems of refraction belong to two classes 1) full solution of the generalized wave equation for particularly simple boundary conditions, usually using the method of expansion into modes [102, 52], and 2) — treatment of refraction by the ray theory method in which (under the criterion that dimensions, such as beam diameters and reciprocals of refractive index gradients, remain much larger then the wavelength) only the paths of energy and the energy flow density retain any significance [43, 44, 90]. GEORGES and CLIFFORD [43] have obtained correction formulas for the effect of refraction on Doppler echo-sounding of wind. They [44] found that the correction remained small up to at least 1 km range, and that the correction depended on the square of the wind Mach number M.

In producing a relatively complex ray tracing model it is necessary to differentiate between two important quantities — the wave-number vector and the ray-path vector of the sound [90]. There is a simple relationship connecting the two vectors (see Fig. 2).

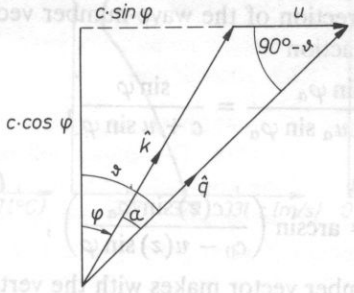

FIG. 2. The relationship between the unit wave-number vector $\hat{k}$, the unit ray-path vector $\hat{q}$, the local speed of sound c, and the wind speed u.

Obviously, the wave-number vector and the ray-path vector are parallel only when there is no wind. The local speed of sound is assumed to be a function of temperature only

$$c = (\gamma RT)^{1/2}, \tag{2.1}$$

where $\gamma = c_p/c_v = 1.40$ (ratio of specific heats), $R = 287$ J kg^{-1} K^{-1} (gas constant for dry air), yielding $c = 20.05T^{1/2}$.

Differentiating (2.1) with respect to z and eliminating the constant we obtain

$$\frac{dc}{dz} = \frac{1}{2}\frac{c}{T}\frac{dT}{dz}, \tag{2.2}$$

showing that a constant temperature gradient within a layer leads to a constant sound-speed gradient within the layer if the variations in these quantitiens are much smaller that their absolute values.

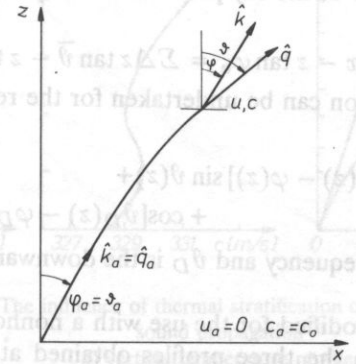

FIG. 3. φ and ϑ as a function of height showing that the wave number vector and ray-path vector are parallel at the antenna.

The wind speed within the antenna (not necessarily at the "ground" is taken as zero so that the wave number vector and ray-path vector are parallel there, thus defining the interrogation angle (see Fig. 3). The antenna radiates not only along its axis but also off axis within a cone of angles. They ray-path is interpreted as the path of biased mean of all the energy radiated. The direction of the wave-number vector at any level can be calculated using Snell's law of refraction

$$\frac{\sin\varphi_a}{c_a + u_a \sin\varphi_a} = \frac{\sin\varphi}{c + u\sin\varphi}, \tag{2.3}$$

which can be solved to give

$$\varphi(z) = \arcsin\left(\frac{c(z)\sin\varphi_a}{c_0 - u(z)\sin\varphi}\right), \tag{2.4}$$

where φ is the angle the wave-number vector makes with the vertical and $u(z)$ the (horizontal) wind velocity at height z. The subscripts (a) refer to the conditions at or within the antenna, whereas the subscript (0) refer to the conditions at the ground.

The time necessary for the sound to travel across the layer is given by

$$t = \Delta z/\bar{c}\cos\overline{\varphi}(z) \tag{2.5}$$

where Δz is the thickness of the layer, and the bars refer to the average value of the variable within the layer which is simply the arithmetic mean of their values at the top and bottom of the slice.

The angle between the wave-number and ray-path vectors is given by

$$\alpha = \arctan\left(\frac{u\cos\varphi}{c + u\sin\varphi}\right). \tag{2.6}$$

The angle between the ray-path vector and the vertical direction is then simply at any height z equal to

$$\vartheta(z) = \varphi(z) + \alpha(z). \tag{2.7}$$

Now the additional displacement of the ray downwind after traversinf the slice is

$$\Delta x = \Delta z \tan\overline{\vartheta}. \tag{2.8}$$

Horizontal displacement δx of the ray-path from its expected rectilinear path can be calculated

$$\delta x = \Sigma\Delta x - z\tan\varphi_a = \Sigma\Delta z\tan\overline{\vartheta} - z\tan\vartheta_a \tag{2.9}$$

A similar series of calculation can be undertaken for the reflected ray [43]

The Doppler shift Δf is

$$\Delta f = f_0[u(z)/c(z)]\{\cos[\vartheta(z) - \varphi(z)]\sin\vartheta(z) + \\ + \cos[\vartheta_D(z) - \varphi_D(z)]\sin\vartheta_D(z)\}, \tag{2.10}$$

where f_0 is the interrogating frequency and ϑ_D is the downward scattered ray-path direction.

The model can be easily modified for the use with a nonhorizontal wind field [90].

The model was applied to the three profiles obtained at 13.00, 19.00 GMT on 15 January 1990, at 0.1.00, 16 January 1990 at Malbork. An interrogation angle 20° was used.

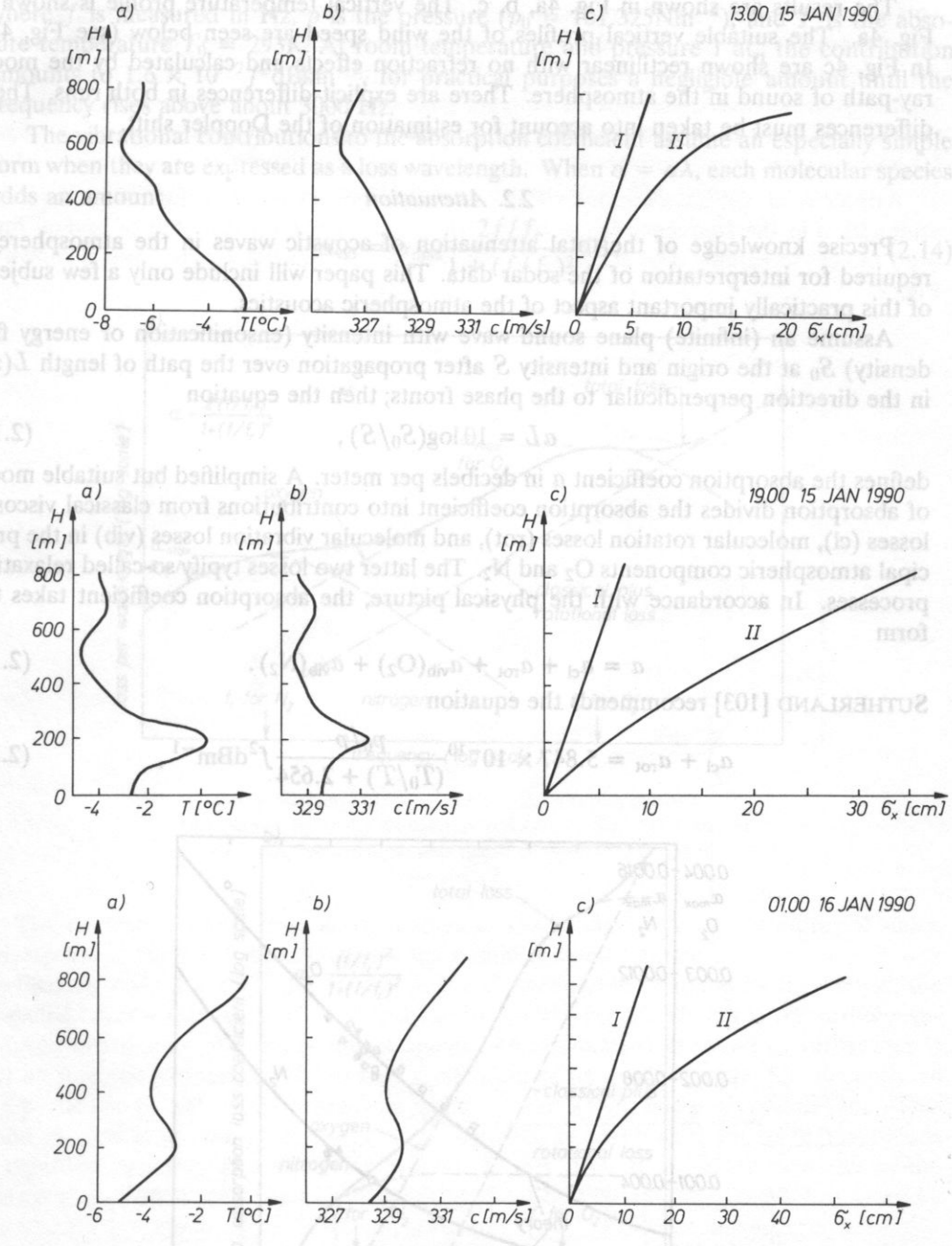

FIG. 4. The influence of thermal stratification of atmosphere on sound propagation

a) vertical temperature profile,

b) vertical profiles of wind speed,

c) differences between the rectilinear and calculated path of sound.

The results are shown in Fig. 4a, b, c. The vertical temperature profile is shown in Fig. 4a. The suitable vertical profiles of the wind speed are seen below (see Fig. 4b). In Fig. 4c are shown rectilinear with no refraction effects and calculated by the model ray-path of sound in the atmosphere. There are explicit differences in both runs. These differences must be taken into account for estimation of the Doppler shift.

2.2. *Attenuation*

Precise knowledge of the total attenuation of acoustic waves in the atmosphere is required for interpretation of the sodar data. This paper will include only a few subjects of this practically important aspect of the atmospheric acoustics.

Assume an (infinite) plane sound wave with intensity (ensonification or energy flux density) S_0 at the origin and intensity S after propagation over the path of length $L(m)$ in the direction perpendicular to the phase fronts; then the equation

$$aL = 10\log(S_0/S)\,, \tag{2.11}$$

defines the absorption coefficient a in decibels per meter. A simplified but suitable model of absorption divides the absorption coefficient into contributions from classical viscosity losses (cl), molecular rotation losses (rot), and molecular vibration losses (vib) in the principal atmospheric components O_2 and N_2. The latter two losses typify so-called relaxation processes. In accordance with the physical picture, the absorption coefficient takes the form

$$a = a_{\mathrm{cl}} + a_{\mathrm{rot}} + a_{\mathrm{vib}}(O_2) + a_{\mathrm{vib}}(N_2)\,. \tag{2.12}$$

SUTHERLAND [103] recommends the equation

$$a_{\mathrm{cl}} + a_{\mathrm{rot}} = 5.847 \times 10^{-10} \frac{p_0/p}{(T_0/T) + 2.654} f^2 \mathrm{dBm}^{-1}\,, \tag{2.13}$$

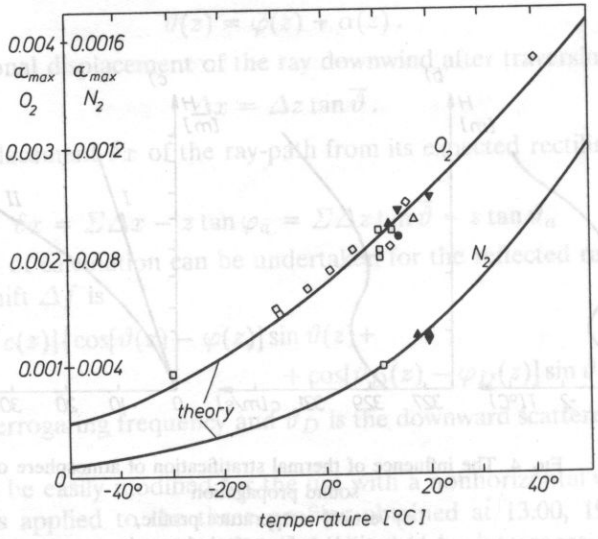

FIG. 5. Maximum absorption coefficient per wavelength due to O_2 and N_2 [17].

where f is measured in Hz, p is the pressure ($p_0 = 101.325\text{Nm}^{-2}$), and T is the absolute temperature $T_0 = 293\text{K}$. At room temperature and pressure 1 at., the contribution amounts to $1.6 \times 10^{-7} f^2 \text{dBkm}^{-1}$, for practical purposes a negligible amount until the frequency rises above about 3000 Hz.

The vibrational contributions to the absorption coefficient assume an especially simple form when they are expressed as a loss wavelength. When $\alpha = a\lambda$, each molecular species adds an amount

$$\alpha_{\text{vib}} = \alpha_{\max} \frac{2f/f_r}{1 + (f/f_r)^2} \text{dB}. \tag{2.14}$$

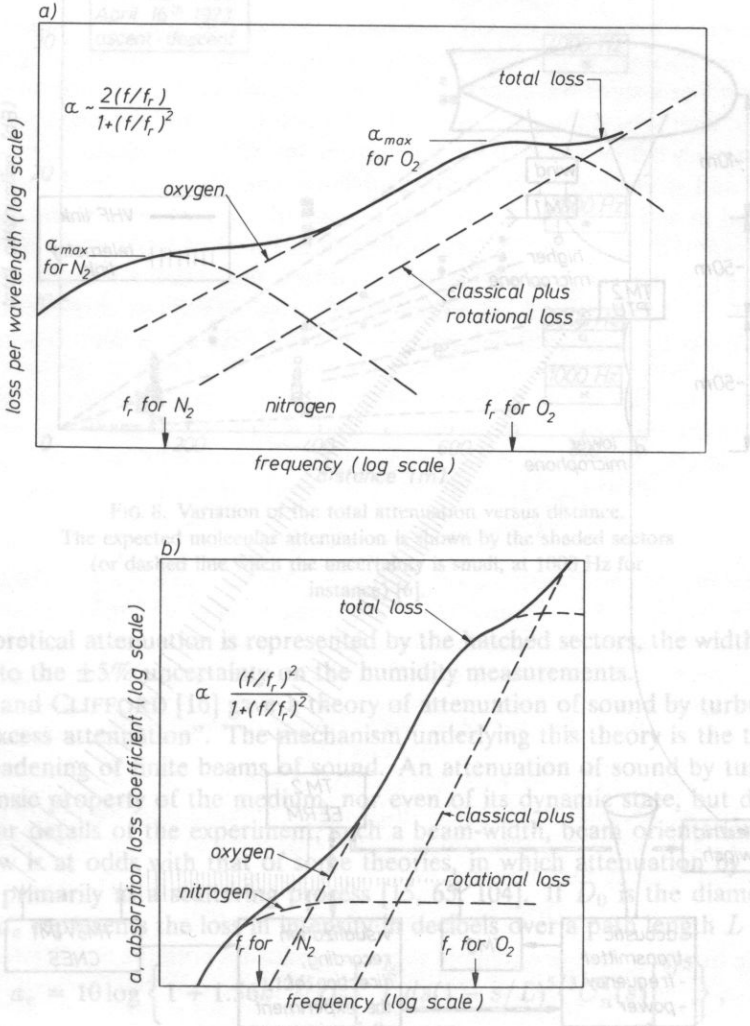

FIG. 6. Frequency dependence of absorption coefficient a) per unit wavelength α and b) per unit distance a [103].

Here f_r represents the frequency of the particular absorption peak and α_{max} — the magnitude of α_{vib} at the peak. Most of the literature uses the dimensionless loss in nepers per wavelength $\hat{\alpha}_{max}$, in place of α_{max} in decibels; thus $\alpha_{max} = 10 \ln \hat{\alpha}_{max} = 4.343\alpha_{max}$. Figure 5 shows the behaviour of $\alpha_{max}O_2$ and $\alpha_{max}N_2$. Figure 6 shows the qualitative behaviour of both the total absorption coefficient a and the absorption per wavelength α.

AUBRY *et al.* [6] have conducted a tethered balloon experiment for measuring total attenuation in the frequency range 1000–5600 Hz along the vertical path of several hundred meters in extent. The arrangement of the elements in the experiments is shown in Fig. 7.

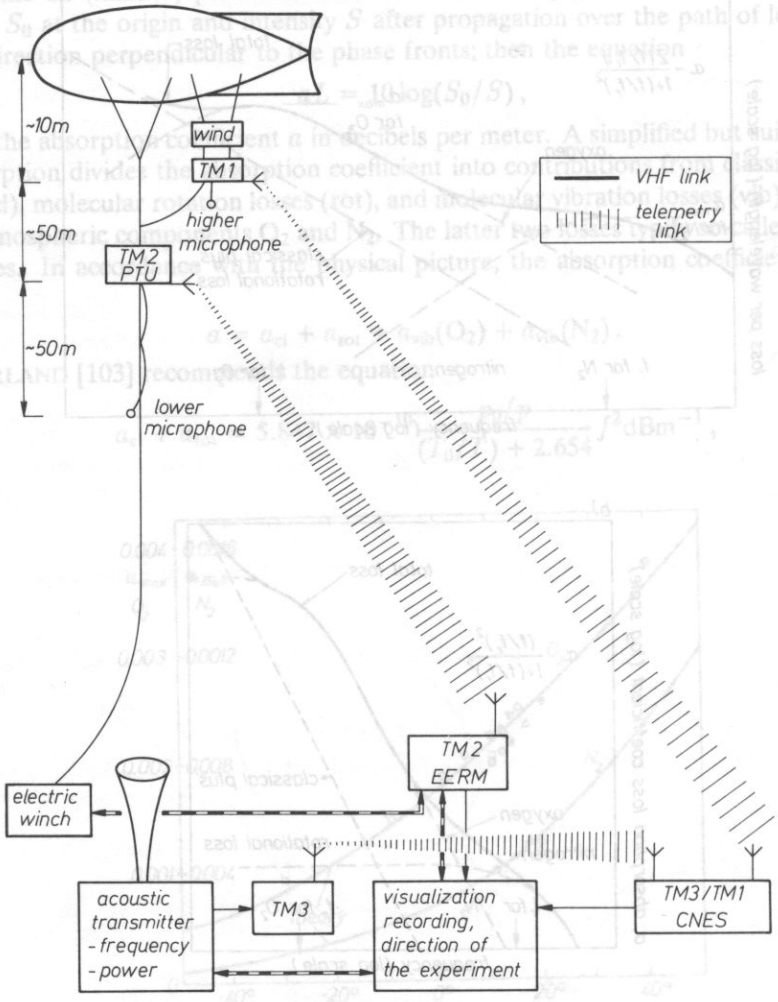

FIG. 7. Functional relation between the various telemetry systems and the operation of the experiment.

An experiment was conducted as follows: the balloon is stopped at a predetermined level, and each frequency is transmitted continuously for about 2 min. After about 15 min, when the complete set has been transmitted, the altitude of the balloon is changed. Application of two microphones separated by 100 m allowed to probe the acoustic field every 100 m stopping the balloon at 200 m intervals. When measurements are performed during both the ascent and descent, a complete sequence of measurements required about 3 hours. The total attenuation versus distance is presented in Fig. 8 [6].

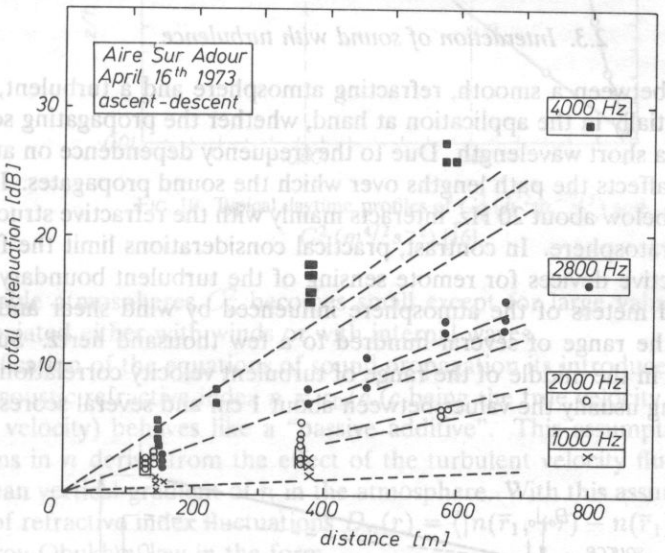

FIG. 8. Variation of the total attenuation versus distance. The expected molecular attenuation is shown by the shaded sectors (or dashed line when the uncertainty is small, at 1000 Hz for instance) [6].

The theoretical attenuation is represented by the hatched sectors, the widths of which correspond to the $\pm 5\%$ uncertainty on the humidity measurements.

BROWN and CLIFFORD [16] gave a theory of attenuation of sound by turbulence, the so-called "excess attenuation". The mechanism underlying this theory is the turbulence-induced broadening of finite beams of sound. An attenuation of sound by turbulence is not an intrinsic property of the medium, nor even of its dynamic state, but depends on the particular details of the experiment, such a beam-width, beam orientation etc. This point of view is at odds with that of some theories, in which attenuation by turbulence is regarded primarily as a scattering process [15, 65, 104]. If D_0 is the diameter of the source and a_e represents the loss in intensity in decibels over a path length L is given by

$$a_e = 10 \log \left\{ 1 + 1.56 k^{12/5} D_0^2 \left[\int_0^L ds (1 - s/L)^{5/3} C_n^2(s) \right]^{6/5} \right\}, \tag{2.15}$$

or, for the case of constant C_n^2

$$a_e L = 10 \log(1 + 0.48 k^{12/5} D_0^2 L^{6/5} C_n^{12/5}), \tag{2.16}$$

where L is the path length of sound beam, S is the distance from transmitter along the path, C_n^2 is the structure parameter of refractive index fluctuations, and k is instantaneous wave number $k = \omega/c_0 = 2\pi/\lambda$. It was shown that the theory of BROWN and CLIFFORD [16] yields results which are in qualiative agreement with observations. When inertial range scattering cross-section (2.22) and echosounder equation (2.23) are used for measurements of the structure parameter for temperature fluctuations C_T^2 and the structure parameter velocity fluctuations C_v^2 excess attenuation can introduce considerable errors into the results.

2.3. *Interaction of sound with turbulence*

The distinction between a smooth, refracting atmosphere and a turbulent, scattering atmosphere lies partially in the application at hand, whether the propagating sound has a long wavelength or a short wavelength. Due to the frequency dependence on attenuation, this distortion also affects the path lengths over which the sound propagates. Infrasound, having a frequency below about 20 Hz, interacts mainly with the refractive structure of the troposphere and stratosphere. In contrast, practical considerations limit the frequencies of sound used in active devices for remote sensing of the turbulent boundary layer (the lowest few hundred meters of the atmosphere influenced by wind shear and heat flow at the surface) to the range of several hundred to a few thousand hertz. Such shorter wavelengths lie just in the middle of the range of turbulent velocity correlation lengths or "eddy" scales, having usually the values between about 1 cm and several scores of meters.

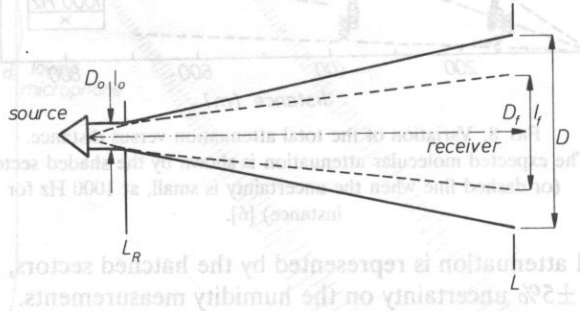

FIG. 9. Geometry of an acoustic beam propagation through turbulence [16].

Because of the acoustic wavelengths ordinarily found in problems of the propagation of sound throught turbulence one can almost always assume that the structure function of the turbulent velocity fluctuations

$$D(\overline{r}_1, \overline{r}) = \langle |v(\overline{r}_1 + \overline{r}) - v(\overline{r}_1)|^2 \rangle , \tag{2.17}$$

(where angle brackets denote ensemble averaging) satisfies both the conditions of isotropy and local homogeneity $D(\overline{r}_1, \overline{r}) = D(r)$, and the Kolmogorov-Obukhov inertial range law

$$D(r) = C_v^2 r^{2/3} , \tag{2.18}$$

where $r = |\overline{r}|$. Equation (2.18) also defines the turbulent velocity fluctuation "structure constant" C_v^2. Figure 10 shows that for the unstable case, C_v^2 varies with altitude.

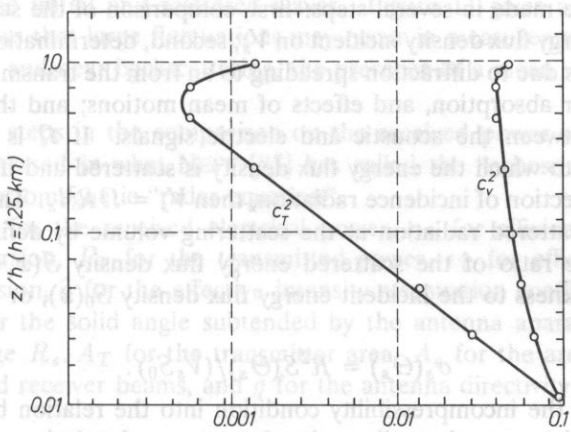

FIG. 10. Typical daytime profiles of $C_T^2(K^2m^{-2/3})$ and $C_V^2(m^{4/2}s^{-2})$ [16].

For stable atmospheres C_v^2 becomes small except for large values in layers of large shear associated either with winds or with internal waves.

Simplification of the equations of sound propagation its introduced by the assumption that the acoustic refractive index $n = c_0/c$ (c being the true velocity of sound and c_0 the reference velocity) behaves like a "passive additive". This assumption implies that the fluctuations in n derive from the effect of the turbulent velocity fluctuation field acting on the mean vertical gradient of n in the atmosphere. With this assumption the structure function of refractive index fluctuations $D_n(r) = \langle |n(\overline{r}_1, +\overline{r}) - n(\overline{r}_1)|^2 \rangle$ also satisfies the Kolmogorov-Obukhov law in the form

$$D_n(r) = C_n^2 r^{2/3}. \tag{2.19}$$

The velocity of sound in a mixture of perfect gases depends on the temperature T and the combined molecular weight m according to the formula $c^2 = \gamma kT/m$, where γ is the combined specific heat ratio and k the Boltzmann constant. Writing $T = T_0 + T'$, where T_0 is the equilibrium temperature end e/p_0 for the ratio of the vapour pressure of water to the total pressure, WESELY [112], obtained the formula for the structure constant for refractivity fluctuations

$$C_n^2 = C_T^2/4T_0^2 + 2(0.307)C_{eT}/4p_0T_0 + (0.307)^2C_e^2/4p_0^2, \tag{2.20}$$

where C_{eT}^2 is the parameter of cross-correlation of humidity and the temperature fluctuations.

2.4. *Scattering*

Scattering of sound by atmospheric fluctuation in "turbulence Mach number" and acoustic refractive index is the physical mechanism underlying the operation of the echo-sounder. Measurement of the characteristics of the received signal and comparison with the known properties of the transmitted signal provide all the acoustically obtainable information about the atmosphere in the scattering volume V_s at the range R. Such a

comparison must be made in several steps: first, comparison of the scattered energy flux density with the energy flux density incident on V_s; second, determination of changes in the energy flux densities due to diffraction spreading to an from the transmitting and receiving antennas, molecular absorption, and effects of mean motions; and third, determination of the relations between the acoustic and electric signals. If Ω is the solid angle in the direction Θ_s into which the energy flux density is scattered and if l_s is the thickness measured in the direction of incidence radiation, then $V_s = \Omega R^2 l_s$. Thus we can compare the incident and scattered radiation at the scattering volume by defining the scattering cross-section as the ratio of the scattered energy flux density $S(x, \Theta_s)$ per unit solid angle and unit thickness to the incident energy flux density $S_0(x)$, or by using the above expression for V_s:

$$\sigma_s(\Theta_s) = R^2 S(\Theta_s)/(V_s S_0)\,. \tag{2.21}$$

If we introduce the incompressibility condition into the relation between wave scattering and the inertial range three-dimensional spectrum of turbulence, and use the Born approximation to the acoustic equation, we can obtain an exact solution for $\sigma_s(\Theta_s)$.

MONIN [69] expressed the inertial range scattering cross-section as

$$\sigma_s(\Theta_s) = 1.52 k_0^{1/3} \cos^2\Theta_s \{a13 C_n^2 + \cos^2(\Theta_s/2) C_v^2/4C_0^2\} \cdot [2\sin(\Theta_s/2)]^{-11/3}, \tag{2.22}$$

where C_n^2 depends on temperature and water vapour fluctuation intensities according to (2.20). We see that when $\Theta = 90^\circ$ the scattering cross-section vanishes, and when $\Theta_s = 180^\circ$ (monostatic sounding), only the fluctuation in N contributes to σ_s. We should expect some changes in $\sigma_s(\Theta_s)$ when the mean wind is no langer zero, even if the frozen turbulence condition is applied to a coordinate system moving with the mean wind. CLIFFORD and BROWN [29] have found the principal effect a shift in the position of the zero cross-section at $\Theta_s = 90^\circ$ to a nearby angle, resulting from rotations of the

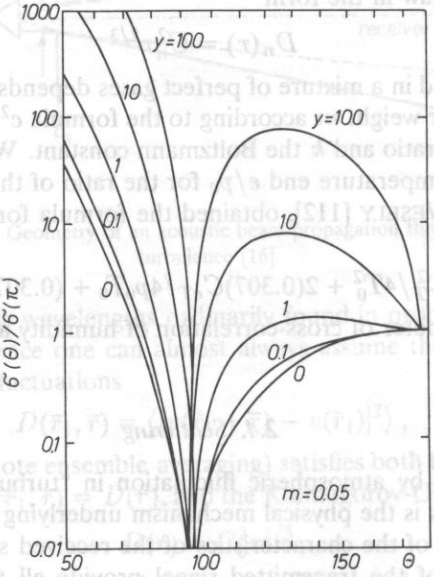

FIG. 11. Typical deformation in a scattering cross-section due to a 15ms^{-1} mean wind, where $\gamma = C_V^2 T_0^2 / C_T^2 C_0^2$ [29].

wave vectors of the initial and scattered waves. Figure 11 gives a typical example of the effect and shows that large fluctuations may occur in measurements near $\Theta_s = 90°$. For backscattering and near backscattering, the presence of a mean wind produces small changes in σ_s.

The remaining steps in the comparison on the received power with the transmitted power can be expressed in what NEFF [85] has called the "echosounder equation", in analogy to the electromagnetic "radar equation".

If we use P_M for the received electrical power, ϵ_R for efficiency of the acoustic-to-electrical conversion, P_T for the transmitted power, ϵ_T for efficiency of electrical-to-acoustic conversion, $\hat{a}$ for the effective intensity attenuation coefficient in nepers per meter, A_R/R_s^2 for the solid angle subtended by the antenna aparature A_R in square meters at the range R_s, A_T for the transmitter area, A_c for the area common to both the transmitter and receiver beams, and g for the antenna directivity gain factor, we can write

$$P_R/\epsilon_R = \epsilon_T P_T \exp[-\hat{a}(R_0 + R_s)] \cdot$$
$$\cdot[(1 + \bar{e}_s \cdot \overline{\mathrm{M}})A(\Theta_s(l_p/2)(gA_R/R_s^2)\sigma_s(\Theta_s)]\,. \qquad (2.23)$$

Here $\overline{\mathrm{M}}$ is the turbulence Mach vector, the $\bar{e}_s$ — unit vector in the direction of the scattered wave, l_p — length of scattered signal. The dimensionless aspect factor $A(\Theta_s)$ equals 1 for monostatic echosounders and approximately equals A_c/A_T for angles near 180°. For the general bistatic case, exact value of A requires computer solutions. Equation (2.23) represents the key link between the theory and experiment, the link between echosonde electrical power measurements and the values of C_n^2 and C_V^2 appearing in the theoretical relationship between wave scattering and turbulence.

3. Acoustic systems and constructions

MCALLISTER [80] used a sounder in the monostatic configuration in which the transmitting and receiving transducers are identical or, at least, nearly collocated. The simplified block diagram shown in Fig. 12 describes the equipment of McAllister.

In this system an acoustic tone burst is amplified, and the audio-signal P_T is sent through a switching device to the transmission transducer. After a suitable delay the transducer is switched to the receiving mode, in which the echo signal P_R is passed to the receiver amplifier and then to a display or recording device.

The present-day acoustic sounding arrangements are shown in Fig. 13.

In the case of a bistatic sounder, the scattering angle is less than 180°, and so the system is sensitive to scattering from both the temperature and velocity fluctuations.

In order to produce detectable echo signals, a high acoustic transmission power is desirable. This can be achieved with high electrical power to the antenna, implying high power handling capability and high antenna efficiency. For a high receiving power it is necessary to use an antenna with a large collecting area and to use the frequencies at which the atmospheric absorption is small, the acoustic absorption increasing rapidly with frequency. However, if the antenna is too large, the width of the beam becomes to narrow, what results in significant sound energy being lost due to refraction by wind [50, 73].

It is usually possible to construct amplifier with noise level well below the environmental noise contribution. However, in very quiet environments, the thermal noise in the

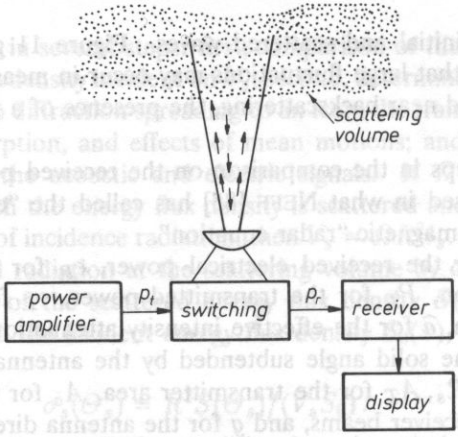

FIG. 12. Simplified block diagram of a monostatic sounder.

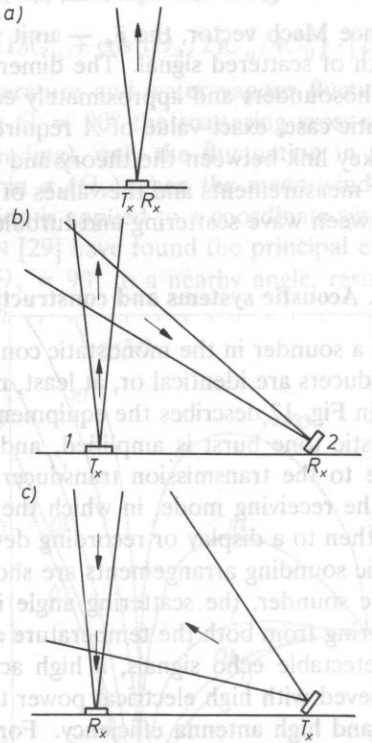

FIG. 13. Common acoustic sounding arrangements a) Monostatic single antenna used for transmission and reception b) narrow beam bistatic system for measurements at a single height, c) Broad beam transmitter probed by a narrow beam receiver used for obtaining profile information. Tx — transmitter; Rx — receiver.

receiver transducer may impose the limit on sensitivity. The intrusion of environmental noise can be minimized by a good antenna design, e.g. low side lobes and screening. Often a low-noise pre-amplifier is used in close proximity to the antenna to eliminate the problems caused by electrical pick-up when long cables (50–200 m) are used to connect the antenna to the receiver. The pre-amplifier incorporates a step-up transformer to match the antenna impedance of a few ohms to the inlet impedance of the receiver a few kilo-ohms.

In the desing of the receiver electronics the most important requirement is to separate the wanted narrow-band acoustic signal from the strong, usually broad-band, noise signal and thus a narrow-band filter is necessary.

Most conventional acoustic sounders use a carrier frequency in the region of 1 to 2 kHz with maximum useful ranges of a few hundred meters to a few kilometers. Operation at higher frequencies, greater than about 4 kHz, has a number of advantages [31, 74, 5]. However, these advantages are at the expense of reduced range because of the greater atmospheric acoustic attenuation at these frequencies.

The main limitations in the performance of an acoustic sounder often depend to a great extent on the characteristics of the antenna, since present-day electronics techniques are capable of achieving almost ideal performance in a sounding system.

There are three types of antenna in common use at frequency in the range of 1–5 kHz:

1) Conical horn antenna

This consist of one or more transducers acoustically coupled to a large impedance matching horn. The aperture diameter is usually 1–2 m to give a beam width of 5–10° and this kind of antenna is reported to have an efficiency of up to 50% [50].

2) Single horn and reflector

In this arrangement a transducer is mounted at or near the focus of a parabolic reflector. Acoustically damped microwave–type antenna reflectors of 1–2 m diameter are often used [50]. The side lobes levels of a horn and reflector system may be determined by the radiation from the transducer itself and hence extra care must be exercised in constructing the acoustic screening.

3) Array antennas

Here the antenna consists of a number of transducers usually in the form of a uniform planar array. The array characteristics, depend on both the array geometry and transducer properties, and wide variations are possible in both of these properties [73]. The polar characteristic of an array can easily be adjusted by changing the array element separation. In Fig. 14 are given the computed mean sound power levels over all azimuth angels as functions of elevation for three arrays.

These calculations are valid for square arrays of identical omnidirectional elements with a spacing of 0.15 m at a frequency of 1500 Hz and velocity of sound of 343 ms^{-1}. The improvement in beam characteristics with increasing numbers of elements is evident.

In the modern acoustic Doppler systems a system of three antennas is commonly used: one is vertical Fig. 15 and two are slanting.

There acoustic pulses had 100 ms lifetime, with a repetition rate of 4 s, corresponding to a range of about 650 m, with an observation every 17 m in height. The signals were digitized and a fast Fourier transform was performed to calculate the Doppler shift.

The electronic configuration of the FFT–type sodar is given in Fig. 16.

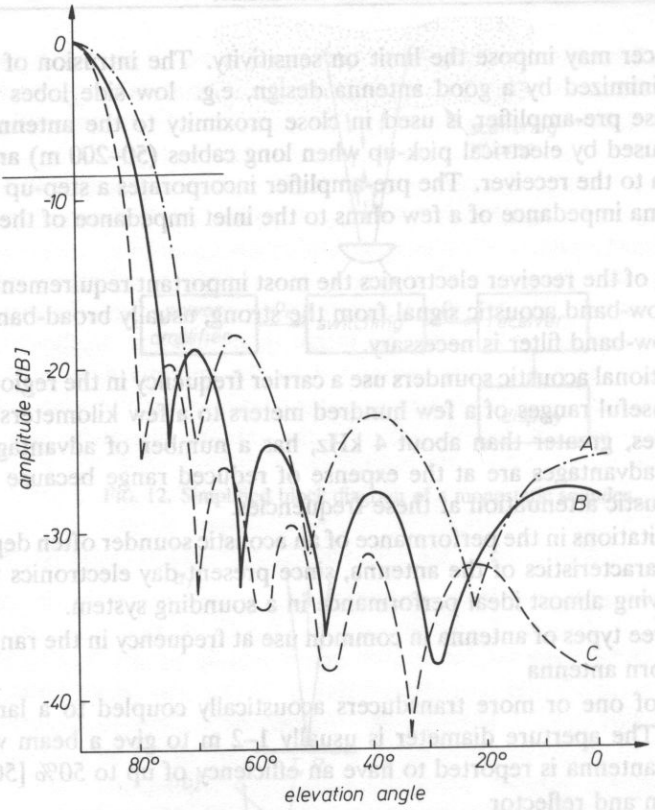

FIG. 14. The polar diagrams of three square arrays of 0.15 m spacing at 1500 Hz showing average level against of elevation A, 5 × 5; B, 7 × 7; C, 9 × 9 [73].

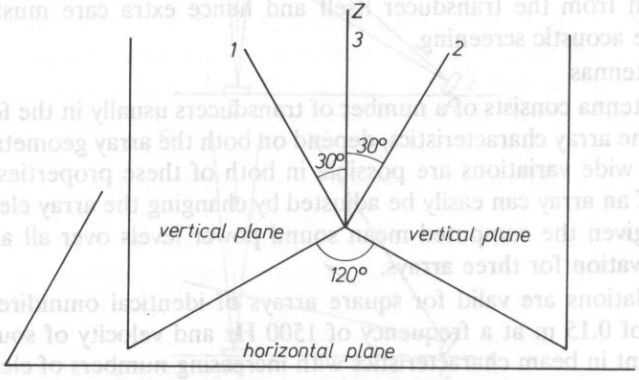

FIG. 15. Geometric configuration of the acoustic sounder three-antenna system. Antenna 1 and 2 are slanting, antenna 3 is vertical collinear with the vertical direction Z [108].

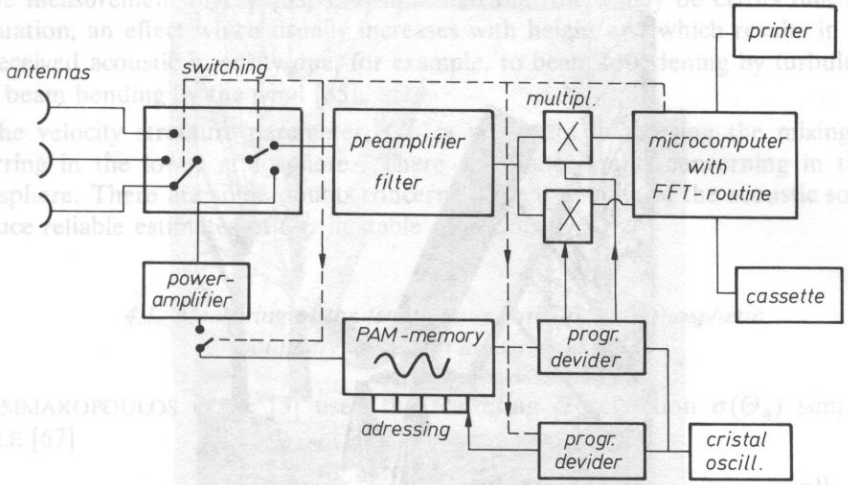

FIG. 16. Electronic configuration of the "FFT" sodar [10].

The electronics consists of emission-reception logic filtering circuits and a power amplifier. The filtering is done in two bands: 1) — the central band around the emission frequency through which the backscattered Doppler signal is coming, and 2) — two side bands which are used to monitor the magnitude of the background noise. The amplitude of the signal in both bandes are measured by the microcomputer to calculate the signal-to-noise ratio.

The software in the microcomputer takes care of the following activities:

- emission-reception switching,
- sampling of signals (2 amplitudes and 1 frequency),
- invalidation of samples with poor S/N–ratio,
- correction of the frequency measurements as a function of signal,
- averaging,
- calculation of horizontal wind speed and standard deviation of the vertical component at the end of the averaging interval,
- printing of the results and storage on a cassette.

Figure 17 shows the modern acoustic sounder made by Military Technical Academy (WAT) and Naval Academy Poland. For instance, the echosonde PS/2 manufactured by Radian Co. (USA) are the following:

1) Doppler winds: vector, components, sigmas from 10–1000 m in 20 range gates.
2) Echo intensity: qualitative backscatter, C_T^2/C_n^2 from 10–2000 m in 200 range gates.
3) Mixing height: fully automatic mixing height, inversion detection and stability class.
4) Frequency: selectable from 1000-5000 Hz; 10–20 ms pulse.
5) Transmissing power: variable from 75–250 W.
6) Antenna aperture: available with 0.9 minisodar, 1.5 m or 1.8 diameter.
7) Unambigous velocity: 0–30 m/s $\pm$ 0.2 m/s.
8) Averaging period: 1–60 min.
9) Environmental: 0°–40° C, 95% humidity non condensing.

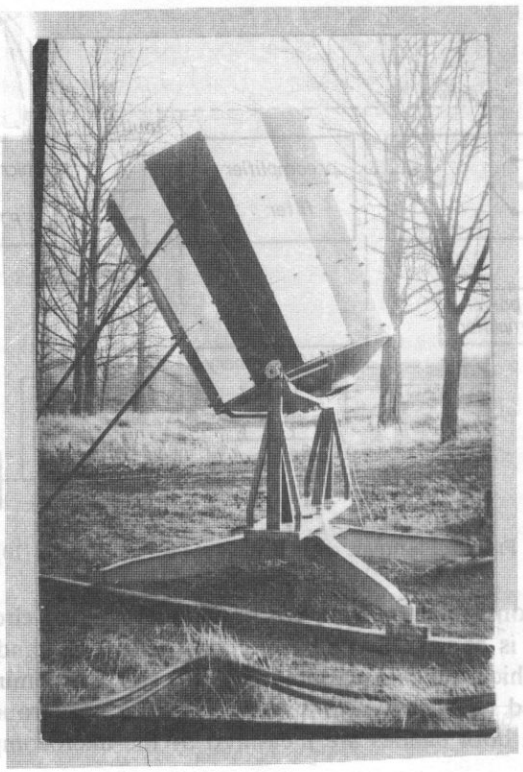

FIG. 17. Monostatic sodar made by WAT (Military Technical Academy) and AMW (Naval Academy).

10) Power: 115/220 vac ± 5% 50/60 Hz.
11) Auxiliary inputs: 12 channels; 12–bit ADC.

4. Acoustic measurement of the parameters of the lower atmosphere

Acoustic sounding techniques have been extensively developed since the initial work of McALLISTER *et al.* [80] and LITTLE [66] provide a valuable method for remote probing of the atmosphering boundary layer. Many qualitative studies of frequently occurring atmospheric phenomena, such as thermal plumes, breaking waves and inversions have been reported [109, 116, 75, 38, 37, 22]. Qualitative information on important atmospheric parameters has also been obtained using the acoustic sounder [41, 54, 116, 38, 93]. The wind velocity has been derived from the Doppler shift of scattered sound, vertical velocity spectra and the velocity structure parameter C_V^2 can also be obtained from these measurements.

The temperature structure C_T^2 has been estimated from the magnitude of the returned signal of a monostatic sounder [33, 109, 116, 75, 38, 5, 76, 37, 22]. The determination of C_T^2 profiles is relevant to optical tracking [108] and could also be used to measure the vertical heat flux under the conditions of local free convection [114, 109]. Recent work

on the measurement of C_T^2 [63, 116] indicated that there may be errors due to excess attenuation, an effect which usually increases with height and which results in a loss of the received acoustic intensity due, for example, to beam broadening by turbulence [19] or to beam bending by the wind [85].

The velocity structure parameter, C_V^2 is important in assesing the mixing process occurring in the lower atmosphere. There are some doubts concerning in the lower atmosphere. There are some doubts concerning the capability of the acoustic sounder to produce reliable estimates of C_V^2 in stable conditions [75].

4.1. Measuring of the temperature structure of atmospheric boundary layer with an acoustic radar

ASIMAKOPOULOS et al. [5] used the scattering cross-section $\sigma(\Theta_s)$ simplified by LITTLE [67]

$$\sigma(\Theta_s) = 0.33k^{1/3}\cos^2\Theta_s\left[\frac{C_V^2}{c^2}\cos^2\left(\frac{\Theta_s}{2}\right) + 0.136\frac{C_T^2}{T^2}\right]\cdot\left[\sin\left(\frac{\Theta_s}{2}\right)\right]^{-\frac{11}{3}}. \tag{4.1}$$

Here Θ_s is the scattering angle, k is the acoustic wave-number and C_V^2 and C_T^2 are the velocity and temperature structure parameters, respectively, defined by

$$C_V^2 = (\overline{\Delta u})^2/r^{2/3}, \tag{4.2}$$

$$C_T^2 = (\overline{\Delta T})^2/r^{2/3}. \tag{4.3}$$

Here $\overline{r}$ is the distance between two points and Δu is the difference of the velocity components parallel to $\overline{r}$ at these points. ΔT is the difference in temperature between the same points separated by a distance $r = (\overline{r})$ while T is absolute temperature in the scattering volume and c is the speed of sound. Equation (4.1) can be combined with the radar equation to give an expression for P_r, the received acoustic power [51]

$$P_r = P_T c\tau\sigma(\Theta_s)A_r\frac{B}{2R^2}\exp(-2\overline{\alpha}R). \tag{4.4}$$

Here P_T is the transmitted acoustic power, τ is the pulse length, A_r the collecting area of the acoustic antenna, and R the range of the scattering region; B is the beam-shape compensation factor which includes the efficiency of the loudspeaker in the receiving mode and allows for the directivity pattern of the antenna; $\overline{d}$ is the mean value, averaged over the path of propagation, of the attenuation coefficient.

Using Eqs. (4.1) and (4.4) in monostatic operation for which $\Theta_s = 180°$, C_T^2 can be written as

$$C_T^2 = \frac{0.54P_r R^2 T^2 \lambda^{1/3}}{P_T c\tau A_T B}\exp(2\overline{\alpha}R), \tag{4.5}$$

where λ is the wavelength of the acoustic waves. Equation (4.5) takes into account neither the excess attenuation, i.e. the loss of acoustic intensity that results from refraction by the wind [85], nor the turbulent beam broadening [19].

The temperature structure parameter, C_T^2 can also be evaluated by means of the formula

$$C_T^2 = 13.6 S_T\left(\frac{n}{\overline{U}}\right)^{2/3} n, \tag{4.6}$$

where n is the frequency in Hz, U the mean wind speed and $S_T\left(\frac{n}{\overline{U}}\right)$ is the frequency spectrum.

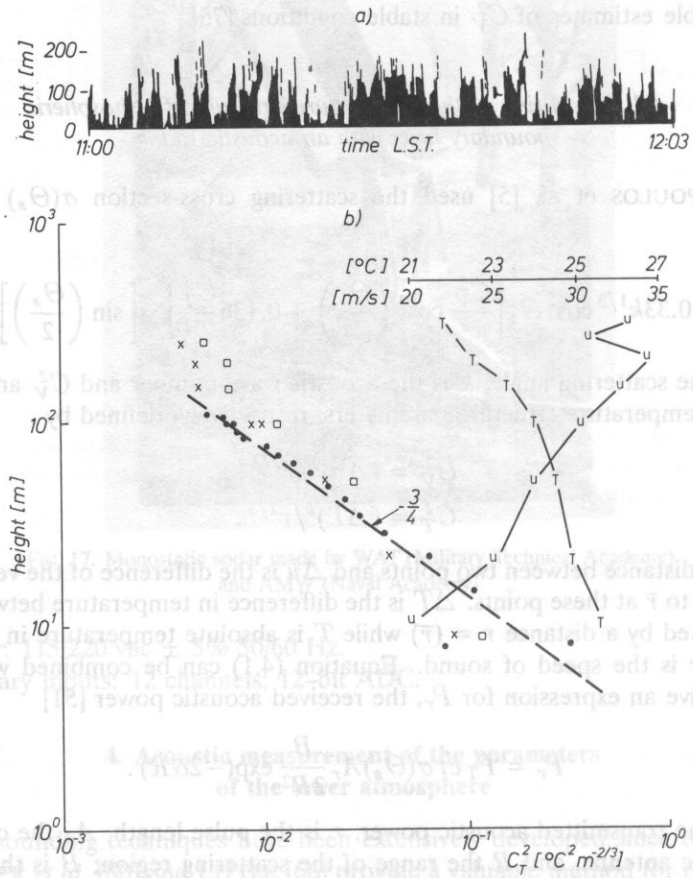

FIG. 18. Monostatic facsimile echoes from 4.7 kHz sodar for the period 11.00 to 12.00 LST on 27 August 1980 (a) and vertical profiles of mean C_T^2 estimates for the same period (b). The line represents $\sim z^{-4/3}$ variation with height and its portion is arbitrary. The C_T^2 estimates obtained by the acoustic sounder from Eq. (4.5) are indicated by (·), the spectral tower estimates via Eq. (4.6) by (□) and the "lag" tower estimates via Eq. (4.3) by (x).

In Fig. 18 profiles of C_T^2 is unstable conditions are shown along with the lower values at the appropriate heights. In Fig. 18, under unstable conditions, the agreement between the tower and the 4.7 kHz sounder is very good. The only difference between the tower and sounder measurements is at the 8 m level, where the proximity of struc-

tures near or at the base of the tower casts doubt on the assumption of isotropy that is necessary for the Eq. (4.6) utilized to reduce the tower data. The acoustic sounder estimates of C_T^2 follow the expected $-4/3$ variation with height [16] as do the tower data if the 8 m point is not taken into account. Above 100 m, the tower data diverge. This is probably due to the combination of reduced stability and large wind shear above the low level jet maximum seen in the mean wind profile, which may have introduced anisotropy.

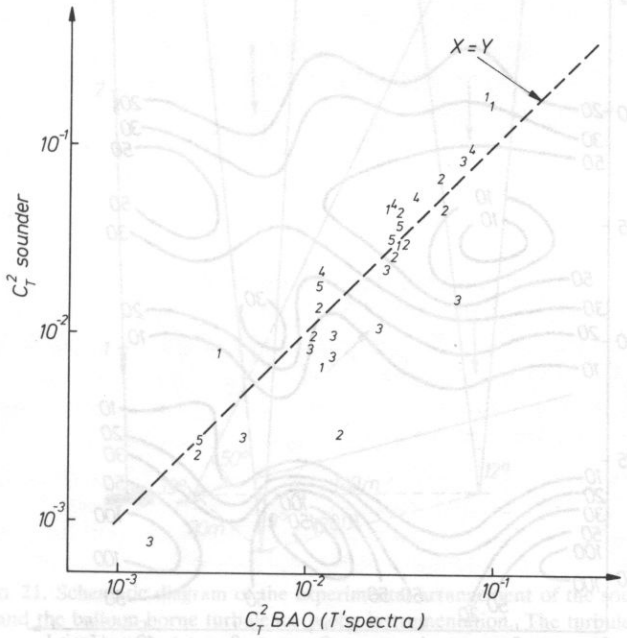

FIG. 19. Scatter diagram of acoustic sounder C_T^2 estimates against tower C_T^2 estimates. Each digit represents the average of 1 hr. The numbers 1, 2 and 3 correspond to data obtained by the 4.7 kHz sounder at height 11, 22 and 50 m, respectively. Numbers 4 and 5 correspond to data obtained by the 6.5 kHz sounder at 11 and 22 m. The line indicates perfect correlation [5].

Figure 19 shows the 1–hr averages for three different heights (11, 22, 50 m) from both sounders 4.7 kHz and 6.5 kHz and the tower. These runs cover both stable and convective conditions.

Figure 20 shows the distribution of C_T^2 on the time-height cross-section. From Fig. 20 it is seen that the distribution of C_T^2 has a horizontally stratified structure and many centers of C_T^2 exist in these layers. It also illustrates the fact that the horizontal distribution of C_T^2 is not uniform.

Figure 20 shows the distribution of C_T^2 on a time-height cross-section in unstable stratification. Figure 20 illustrates the presence of thermal plumes, characteristic of these conditions. It should also be noted that C_T^2 considerably increases within thermal plumes compared with the level outside the plumes. MOUSLEY *et al.* [76] have presented interesting results in measuring the temperature structure parameter C_T^2 using a novel bistatic

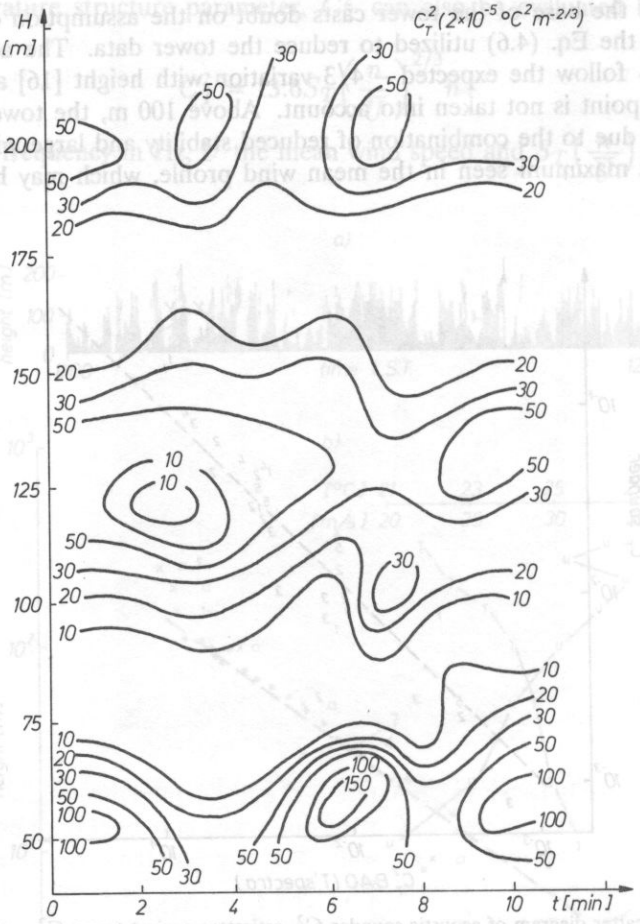

FIG. 20. Contour diagram of C_T^2 (stable stratification) [116].

sounder comprising a fan beam transmitter and a vertically directed receiver. Simultaneous profiles of the temperature structure parameter are obtained using a conventional monostatic sounder.

The experimental arrangement involving two synchronized acoustic sounders and the mobile balloon-borne turbulence probe system is illustrated in Fig. 21.

One sounder is a conventional vertically directed monostatic device with a single array antenna and is used to obtain profiles of the temperature structure parameter (C_T^2) up to height of 340 m. The other sounder is a novel bistatic system comprising a tilted fan beam transmitting array antenna located 140 m away from a vertically directed receiving array. This arrangement has the advantage that the receiving antenna points in the direction of the least ambient noise, which is usually produced mainly by wind or vehicles. Additionally, full advantage can be taken of the side lobe level reduction produced by the acoustic screening.

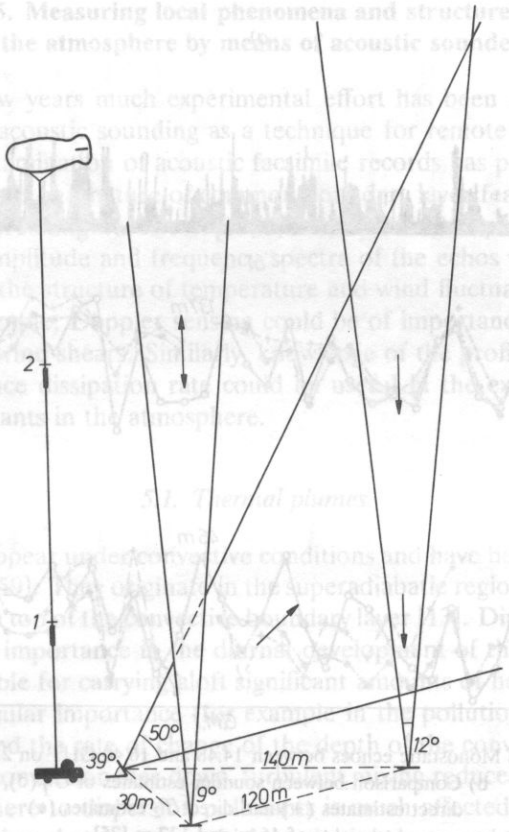

FIG. 21. Schematic diagram of the experimental arrangement of the sounders and the balloon-borne turbulence probe instrumentation. The turbulence probe heights are indicated by the numbers 1 and 2.

Figure 22 (a, b) shows the corresponding bistatic facsimile recording with the comparison of sounder and turbulence C_T^2 probe estimates. The corresponding monostatic facsimile is also shown (Fig. 22a) and illustrates the presence of thermal plumes.

There is a strong correlation between the C_T^2–plots at the two heights due to the vertical organization of thermal plume structures. The mean spectral C_T^2 values at 46 m and 137 m of $5.4 \times 10^{-4} K^2 m^{-2/3}$, respectively, are of the same orders as those reported by KAIMAL [58] and CAUGHEY [23] for these heights in the convective boundary layer.

WEIL *et al.* [109] described a method of evaluation of heat flux profile in the well-mixed layer and heat flux of the surface layer using the vertical velocity variance measured by the Doppler shift of the acoustic sounder. Moreover, they made a comparative evaluation of the different expressions for C_T^2 in the convective boundary layer, and showed that measurement of the vertical velocity variance w'^2 and of the inversion height Z_i, by means of an acoustic sounder, could give good C_T^2 estimates. Their method has the advantage of short measuring times necessary to compute the heat flux and makes it possible to take account of several thermal plumes.

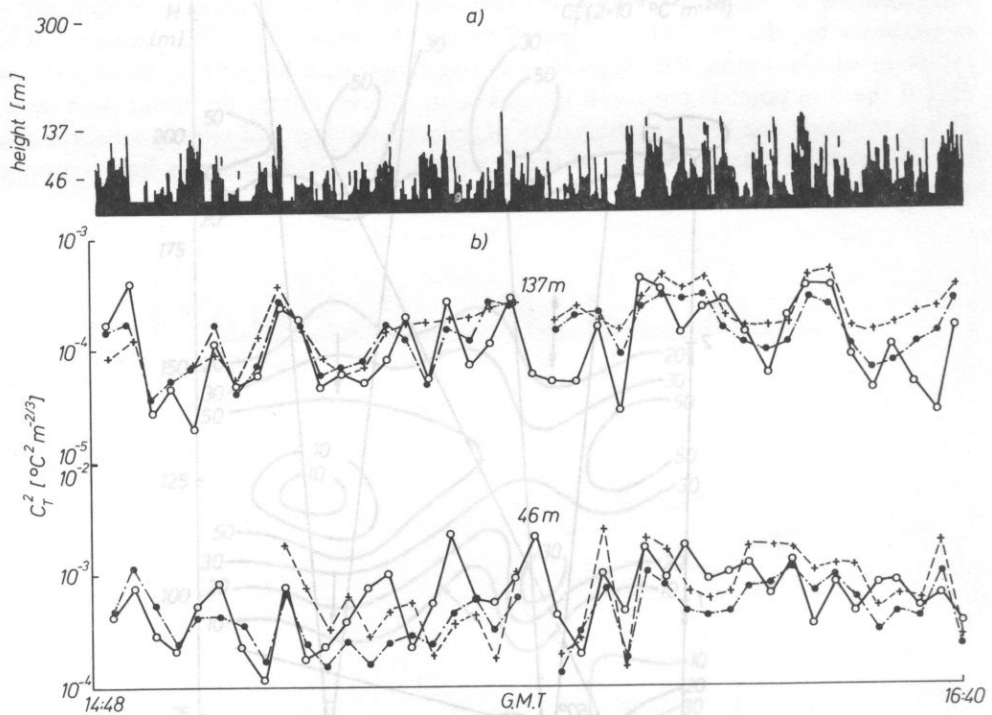

FIG. 22. a) Monostatic echoes between 14.48 and 16.40 GHT on 21 June 1977,
b) Comparison between sounder estimates of C_T^2(○),
direct estimates (+) and direct T_2 estimates (●)
at heights of 46 m and 137 m [75].

Table 1. Evaluation of Q_0 Kms^{-1} [109]

Local time	h' (m) Evaluates by the vertical velocity variance method	Z_i (m) Evaluated by sounding	Q_0 (Kms^{-1}) Evaluated by vertical velocity variance method	Q_0 (Kms^{-1}) INRA
0658–0728	220	200	0.047	0.052
0728–0758	260	260	0.067	0.052
1032–1102	645	660	0.11	0.09
1102–1132	750	755	0.16	0.09

Here Q_0 — surface layer heat flux, Z_i — inversion heights, h' — height at which heat flux vanishes.

Table 1 shows the good agreement between the two methods of surface heat flux computation.

The results illustrate the usefulness of the method presented there to observe changes in heat flux with time.

To conclude indirect measurements of PBL parameters can be more representative than direct measurements, because the latter can be sensitive to local conditions, particularly in the surface layer [115].

5. Measuring local phenomena and structure of the atmosphere by means of acoustic sounders

During the last few years much experimental effort has been devoted to the quantitative evaluation of acoustic sounding as a technique for remote probing of the lower atmosphere. Visual examination of acoustic facsimile records has provided a valuable insight into the occurrence and nature of common boundary layer features; thermal plums, nocturnal inversions, breaking waves etc. [33, 1, 24, 39]. However, of a potentially greater importance are the amplitude and frequency spectra of the echos which contain quantitative information on the structure of temperature and wind fluctuations in the boundary layer studies. For example, Doppler sensing could be of importance in assessing the occurrence of low-level wind shears. Similarly, knowledge of the profiles of vertical velocity variance and turbulence dissipation rate could be useful in the experiments concerning the diffusion of pollutants in the atmosphere.

5.1. Thermal plumes

Thermal plumes appear under convective conditions and have been observed by in-situ sensor for same time [59]. They originate in the superadiabatic region near the ground and normally extend to the top of the convective boundary layer [13]. Direct observations show that they are of great importance in the diurnal development of the boundary layer over land and are responsible for carrying aloft significant amounts of heat and moisture from the surface. Of particular importance (for example in the pollution studies), is the time onset of convection and the rate of change of the depth of the convective layer. Similarly in the evening, when convection dies down, turbulent mixing reduced dramatically and the ability of the atmosphere to dispersion pollutants is much affected. Considerations such as these illustrate the fact that a system which can remotely record the state of convection over long periods of time is likely to be of considerable usefulness.

A typical example of thermal plume structures as recorded by an acoustic sounder is shown in Fig. 23a. This was recorded on a clear day in light wind conditions over a dry short grass surface in summer, using a monostatic sounder operating at 2048 Hz [75].

The plume structure seen by the sounder extends to a height of about 200 m while the apparent plume diameter contracts or sometimes remains approximately constant as a function of height. The transmitted frequency determines not only the atmospheric absorption of the acoustic signal, and hence the range of the system, but is also related to the scale of the atmospheric turbulence which the sounder will observe. An example of acoustic sounder facsimile recordings of thermal plumes obtained by simultaneous application of three soundings frequencies is shown in Fig. 23. Figure 23a,b,c were obtained from closely spaced sounders operating at 2.05 kHz, 4.7 kHz and 6.5 kHz, respectively. The three records, although showing different plume heights, do nevertheless agree remarkably well as for as the relative positions and basic shapes of the plumes are concerned. Normally the monostatic acoustic sounders are directed vertically or at a large angle to the horizontal direction. This is necessary, particularly for a sounder at the ground level, since reflections from near objects (e.g. trees and buildings) or from the ground itself can be received via the antenna side lobes. These echoes are often of greater amplitude than the atmosphere returns. However, sounders which operate at the relatively high

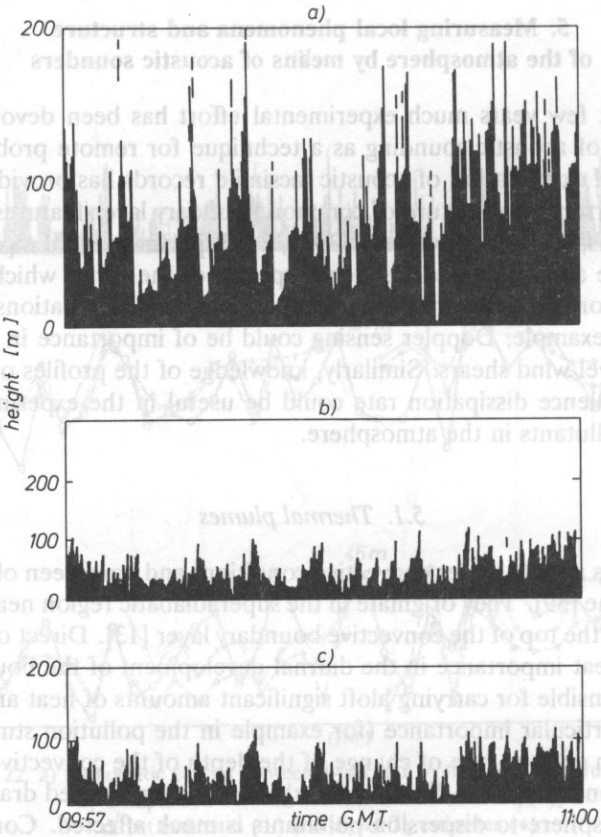

FIG. 23. Acoustic sounder facsimile records of thermal plumes for the period 09.57 — 11.00 GMT on 18 August 1978, obtained using three sounders operating at frequency a) 2048 Hz, b) 4.7 kHz, c) 6.5 kHz [75].

frequencies of 4.7 and 6.5 kHz [74] use small antennas, the side lobes of which can be efficiently screened with a minimum of acoustic absorbing material. The main disadvantage of using high-frequency sound is the reductions of the useful range from which echoes may be received. For these sounders, the maximum range is about 200–300 m. Due to their portability, these antennas can readily be mounted on a tower and directed almost horizontally. The convective boundary layer can be studied by simultaneous application of horizontal and vertical acoustic sounding.

MOULSLEY et al. [74] used 6.5 kHz and 4.7 kHz sounders to investigate convective structures of the boundary layer. The 4.7 kHz sounder was directed vertically and 6.5 kHz sounder could be directed at angles between 0 and 15 deg above the horizont. The sounders were operated with pulse duration of either 31 or 62 ms and to a pulse repetition frequency of 0.5 Hz, which corresponds to a maximum unambiguous range of about 340 m. Figure 24 shows fascsimile records obtained from simultaneous horizontal and vertical soundings. For each of the records, the lower half of the figure shows the conventional vertical monostatic record. We can observe the presence of thermal plumes and the commonly observed intense low-level echoes together with a fairly rapid decrease in

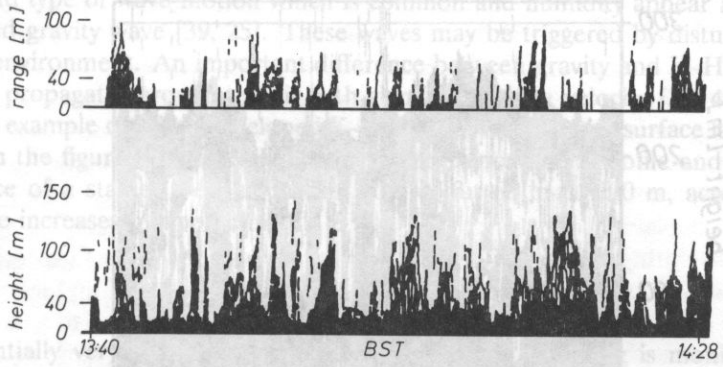

FIG. 24. Facsimile records for 18 September, 1978 between 13.40 and 1428 BST. The upper trace is due to the horizontal sounder pointing downwind at an angle of elevation of 5 deg. The lower trace is due to the vertically pointing sounder. From MOUSLEY et al. [74].

echo strength with height, corresponding to the reduction of the remperature structure parameter in convective conditions (KAIMAL *et al.* [58]).

The remarkable degree of similarity between the facsimile record of vertical and horizontal sounding is noteworthy. The significant differences, however, are the angle appearance of the plumes when sounding downwind, the less marked reduction of the echo signal with range, and the absence of a high echo strength at a close range.

The horizontal sounding technique may provide quantitative information on the spatial variability of atmospheric turbulence which could prove to be particularly interesting under stable conditions, when the interpretation of vertical sounding return is difficult.

5.2. Inversions

One of the most useful applications of acoustic sounding may well prove to be the monitoring of inversions within the lowest few kilometers of the atmosphere. These are regions in which the temperature increases with height, contrary to the normal decrease typical of the troposphere.

Inversions are of great metorological significance since their presence may indicate preferred regions for strong wind shear which can be of importance to aviation. They can also sometimes limit the growth of the convective boundary layer and, hence, influence such parameters as the maximum daytime temperature, visibility etc. In some cases the height of the lowest inversion may be taken as the depth of the convective boundary layer which is an important scaling parameter in the description of turbulence in the lower atmosphere, and is relevant to the dispersal of pollutants.

An acoustic record taken on 28 October 1975 between 13.35–14.45 GMT, when the convective boundary layer was capped by a strong ($\sim$ 10 K) inversion with a base at about 200 m, is shown in Fig. 25.

The interaction of turbulent convective plumes with the region of strong temperature gradients generates an intense echo layer. This interface represents the maximum convection on this day and may be taken as the boundary layer depth [60].

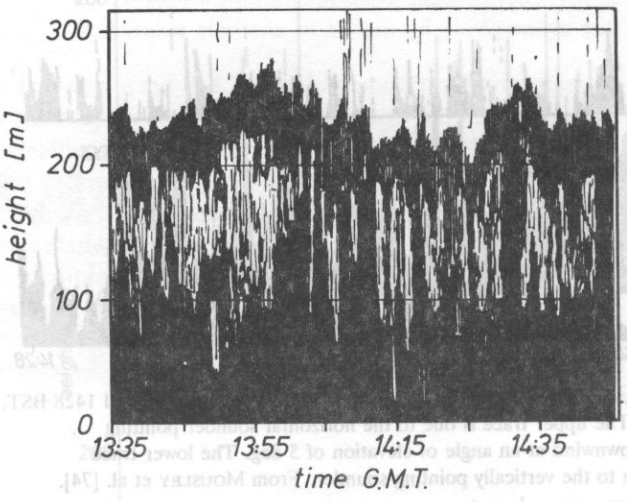

FIG. 25. Sounder facsimile chart for the period 13.35 — 14.45G HT on 28 October 1975.

5.3. *Stable conditions and waves*

Acoustic sounding offers an excellent method for remotely assesing the significance of wave motion [39]. The most common form of wave-like activity in the boundary layer is the Kelvin–Helmholtz (K–H) instability. This occurs in layers where the static stability is much lowers than average, i.e. where large gradients of temperature and humidity appear.

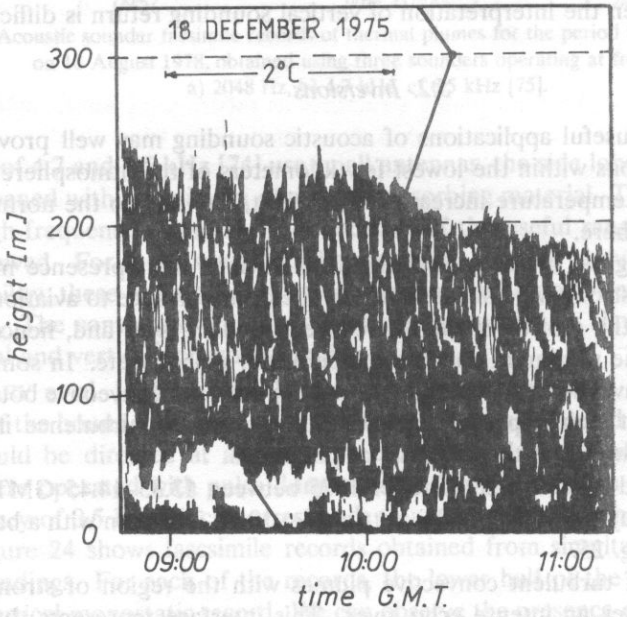

FIG. 26. Kelvin-Helmholtz waves in a surface based stable layer. The solid line indicates the temperature profile at this time [33].

A second type of wave motion which is common and humidity appear atmosphere is the so-called gravity wave [39, 25]. These waves may be triggered by disturbance within the stable environment. An important difference between gravity and K–H waves is that the former propagate through the air with significant phase velocity [39, 46]. Figure 26 presents an example of a well-developed K–H breakdown in a near surface layer [33]. The solid line in the figure indicates the current mean temperature profile and this confirms the presence of a stable layer, extending from about 60 m to 300 m, across which the temperature increases by approximately 2 K.

5.4. Acoustic sounding of clouds

A potentially very important application of acoustic sounding is monitoring of the height of low level layer cloud or fog top [87, 57]. Since the cloud layer is turbulent intense small-scale variations in temperature are generated at cloud top and, hence, they generate acoustic returns. Acoustic scattering has also been observed to occur at the boundaries of cumulus cloud [41]. An acoustic sounding system placed on the NOAA ship "Oceanographer" during GATE provided a unique meteorological data set [41]. The sounder was a radar-like device in that it emitted short bursts (200 ms) of acoustic energy at regular intervals (typically, once every 5 s). Three distinct boundary-layer situ-

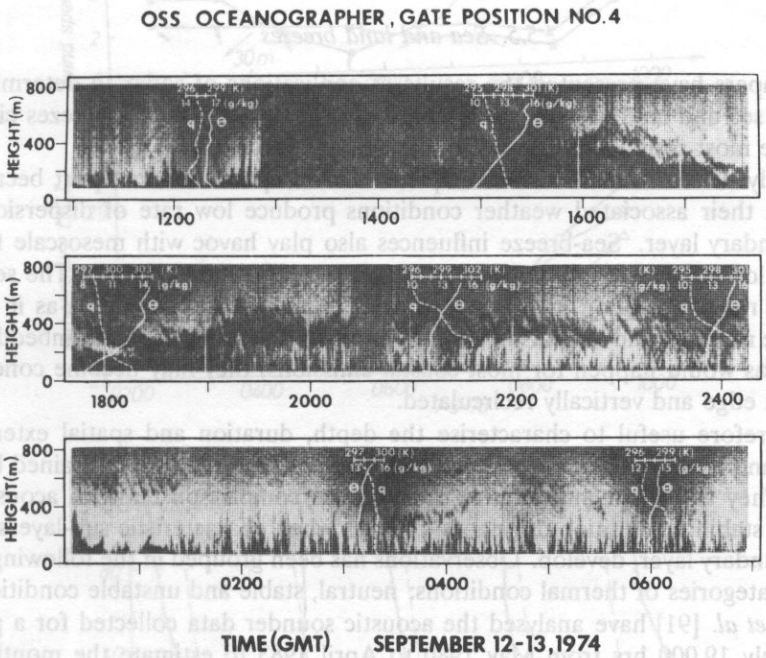

FIG. 27. An acoustic facsimile recorded during the passage of an organized squall line with radiosonde profiles of potential temperature θ and mixing ratio q. The profiles have been placed on the facsimile approximately at the correct flight times. From GAYNOR and MANDICS [42].

ations appear on the facsimile records of backscattered acoustic intensity: 1) ubiquitous plume echoes associated with undisturbed conditions; 2) cool-air outflows (or wakes) from either squall-line or isolated cumulonimbus activity associated with disturbed conditions and 3) "hat" or "hummock" — shaped echoes associated with low-level cumulus clouds usually occuring during weakly disturbed conditions. Profiles of potential temperature and mixing ratio from radiosonde flights launched from the "Oceanographer" are compared with the acoustic data (comp. Fig. 27).

Figure 27 shows the time-height facsimile records of the intensity of backscattered acoustic signals during the passage of an intense, organized squall line. Scattering by small-scale ($\sim$ 0.1 m) turbulent temperature (and, to a lesser extent, humidity) inhomogeneities produced the dark regions seen in the record; white areas correspond to a lack of scatter. Convective plumes observed during GATE were less vigorous than those seen over land. Bulk aerodynamic fluxes of surface sensible and latent heat varied in time with the passage of thermal plumes. The rate of dissipation of turbulent kinetic energy was calculated in the upper mixed layer using an acoustic Doppler — differencing technique. Many of the dynamical aspects of the tropical marine boundary layer can be identified and analyzed using the acoustic sounder as a tool. Using Doppler derived vertical velocities along with the in situ meteorological data, were identified some of the structures seen with the sounder for marine boundary layer of atmosphere.

5.5. Sea and land breezes

Many papers have presented the results of applications of sodar to determining the structure of sea and land breezes at coastal site [1, 9, 91, 67]. The sea-breezes circulation is one of the most prominent mesoscale features in coastal areas.

The study of sea-breezes has consequence for air pollution transport because sea-breezes and their associated weather conditions produce low rate of dispersion in the coastal boundary layer. Sea-breeze influences also play havoc with mesoscale forecasts, such as would be necessary for a Nuclear Emergency (THUILLER [106]). The sea-breeze can cause a rapid transition in near-shove wind directions and stabilities as it advances inland in the morning and retreats in the afternoon. If pollutants become embedded in the sea-breeze, as would happen for most coastal emissions, they may become concentrated on the front edge and vertically recirculated.

It is therefore useful to characterise the depth, duration and spatial extent at the sea-breeze and the turbulence associated with it. Similar results were obtained by BACCI *et al.* [9]. They turn their attention to a qualitative comparison between acoustic radar returns and stability condition during sea-breezes when characteristic sub-layers, like the internal boundary layer, develop. Observations has been grouped in the following analysis into three categories of thermal conditions: neutral, stable and unstable conditions.

RAGHU *et al.* [91] have analysed the acoustic sounder data collected for a period of approximately 19.000 hrs from May 1980 to April 1983 to estimate the monthly mean percentage time of occurrence of sea breezes, thermal plumes and nocturnal inversions with respect to total time of observations.

The occurrence of sea-breezes at coastal zones reduced both the convective instability and nocturnal stability. Information about such changes in stability is useful as input to prediction models of atmospheric diffusion in a coastal industrial cities.

In recent paper JURY and SPENCER–SMITH [57] have investigated summer weather conditions along the west coast of Africa near 34°S, 18°E using Doppler acoustic sounder profiles.

Case studies were selected from two year record of composite analyses over the diurnal cycle.

AGGARWAL *et al.* [1] made observations by an acoustic sounder and on a meteorological tower at Tarapur (India). The probing range of the acoustic sounder was 700 m. The meteorological tower sensed wind and temperature at various level up to a height of 120 m. The site being close to the sea shore, the thermal environment of the lower atmosphere is controlled mostly by land and sea-breeze circulations. Thermal convective

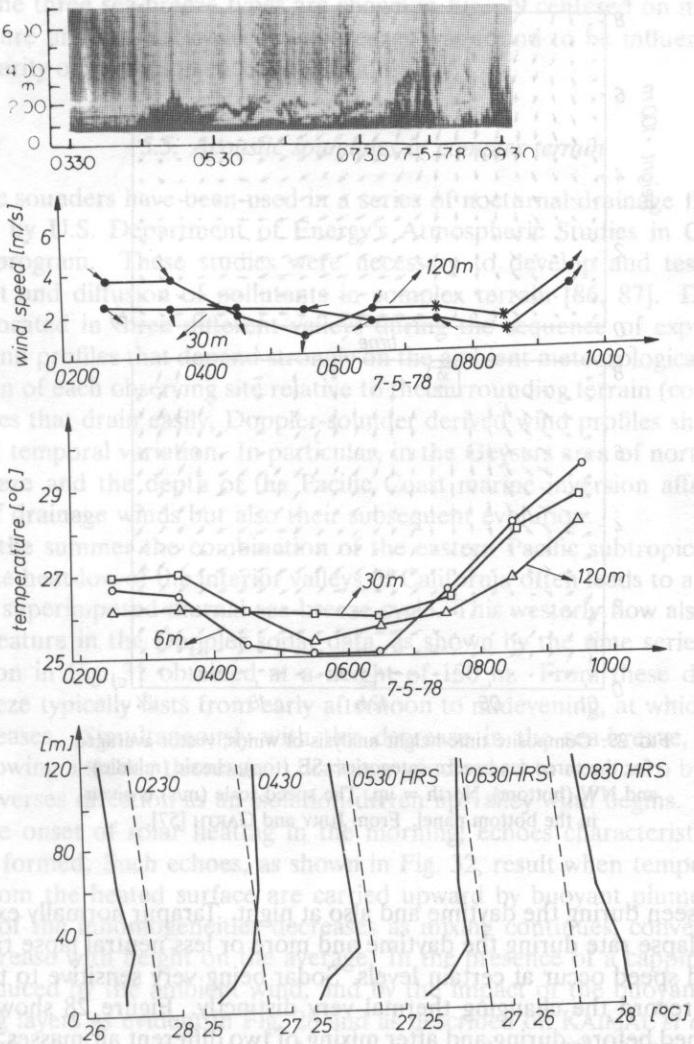

FIG. 28. Sodar structure observed in May 7, 1978 during the transition period of mixing of the different air masses [1].

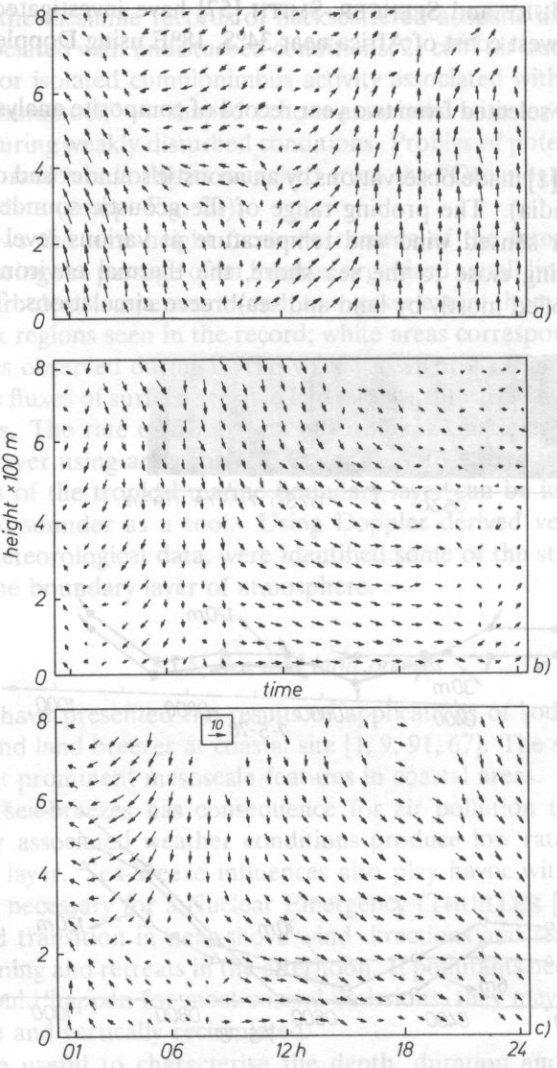

FIG. 29. Composite time-height analysis of winds, vector averaged for the three sea-breeze categories: SE (top), classic (middle) and NW (bottom), North = up. The speed scale (m/s) is given in the bottom panel. From JURY and GARTH [57].

structures were seen during the daytime and also at night. Tarapur normally experiences a super-adiabatic lapse rate during the daytime and more or less neutral lapse rate at night. Changes in wind speed occur at certain levels. Sodar being very sensitive to temperature changes, it can record the changing thermal very distinctly. Figure 28 shows the sodar echogram obtained before, during and after mixing of two different air masses. At 0.4.03 h the inversion becomes suddenly stronger (about 0.8°C) and winds show a sudden change in direction at the 6 and 30 m levels. The wind which was NNW-N at 30 m shifts to

N-NNE. This sudden change in wind direction is associated with a land breeze at the lower level. The change of wind direction from sea to land is also associated with the establishment of an elevated layer as can be seen in the echograms from 0.5.30 h onwords in Fig. 29.

The sounder climatology illustrate the four-dimensional characteristic of sea-breezes near Cape Town. It become apparent that different types of sea-breezes on the basis of the direction of the upper boundary-layer flow in relation to the time of day. The three types were named SE, classic and NW. Each of the categories represented a distinct type, the SE being a weakening and veering of the gradient trade wind, the classic being the traditional land sea-breeze and the NW being characterised by NE winds in the morning and generally NW winds in the upper boundary layer. Time-height analyses of the wind vectors of the three sea-breeze types are shown in Fig. 29 centered on mid-day.

The nature and diurnal cycle of sea-breezes was found to be influenced also by the non-stationarity of synoptic weather conditions.

5.5. Acoustic soundings in complex terrain

Acoustic sounders have been used in a series of nocturnal drainage flow experiments carried out by U.S. Department of Energy's Atmospheric Studies in Complex Terrain (ASCOT) program. These studies were necessary to develop and test better models of transport and diffusion of pollutants in complex terrain [86, 87]. Doppler acoustic sounders, located in three different valleys during the sequence of experiments, reveal drainage-wind profiles that depend strongly on the ambient meteorological conditions and the elevation of each observing site relative to the surrounding terrain (comp. Fig. 30). In elevated sites that drain easily, Doppler-sounder derived wind profiles show considerable vertical and temporal variation. In particular, in the Geysers area of northern California, the sea-breeze and the depth of the Pacific Coast marine inversion affect not only the imitation of drainage winds but also their subsequent evolution.

During the summer the combination of the eastern Pacific subtropical high pressure zone and the heat-low of the interior valleys of California often leads to a strong on shore flow with a superimposed diurnal sea-breeze cycle. This westerly flow also appeared as a persistent feature in the Doppler sodar data, as shown by the time series of wind speed and direction in Fig. 31 obtained at a height of 150 m. From these data we see that the sea-breeze typically lasts from early afternoon to midevening, at which time the wind speed decreases. Simultaneously with this decrease in the sea-breeze, drainage winds begin. Following a steady decrease in drainage wind speed to near zero by early morning, the wind reverses direction as an isolation-driven up-valley wind begins.

With the onset of solar heating in the morning, echoes characteristic of convective activity are formed. Such echoes, as shown in Fig. 32, result when temperature inhomogeneities from the heated surface are carried upward by buoyant plumes. Because the magnitude of the inhomogeneities decreases as mixing continues, convective echo magnitudes decrease with height on the average. In the presence of a capping inversion, the mixing produced by the ambient wind, and by the impact of the buoyant parcels results in scattering layers as evident in Fig. 28 and as described on KAIMAL *et al.* [60].

In Fig. 33 we show echoes from the top a stratus layer. Figure 33 is an example of sodar echo pattern corresponding to low stratus filling the valley. Variations in the height

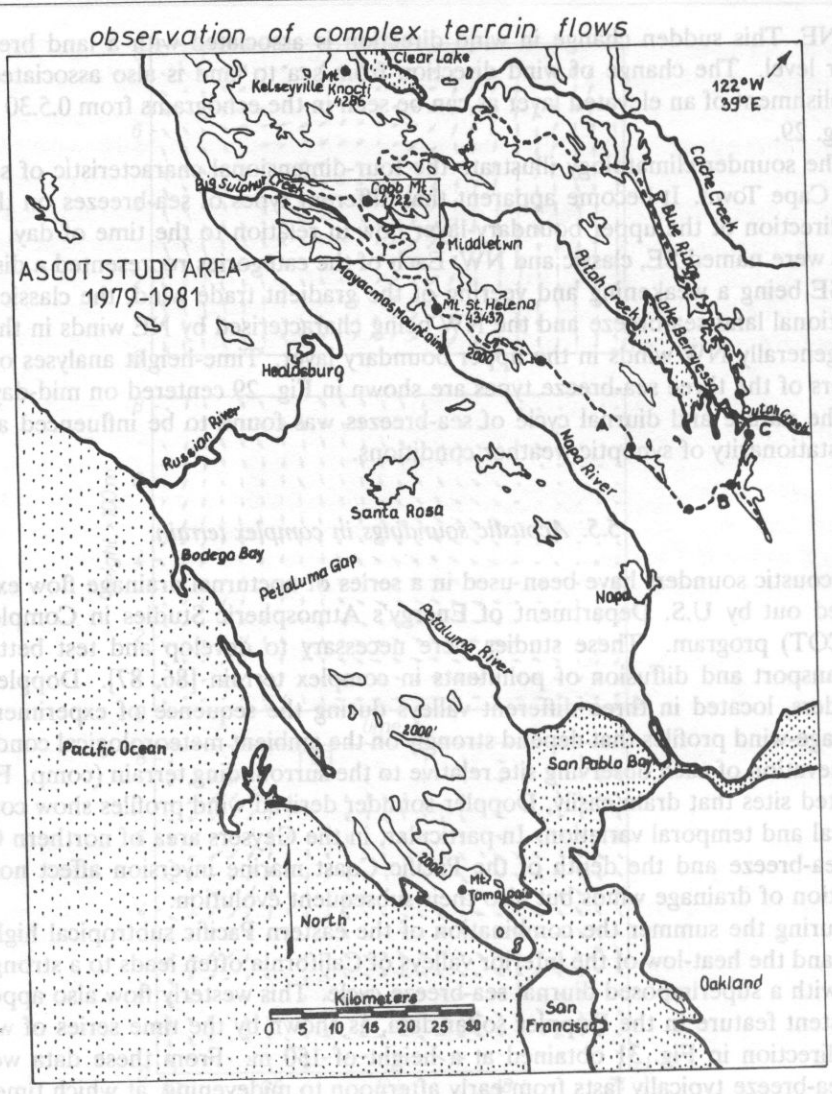

FIG. 30. Major topographic features surrounding the Geysers study area used in the ASCOT experiments carried out between 1979 and 1981.

of the echoes correspond to variations in the height of the stratus layer. The thickness of the layer presumably corresponds to the amount of shear at the top of the cloud and the thickness of inversion at or above cloud top [87].

MAZANDER and WEILL [72] presented first observations of dynamic influence of the forest on the boundary layer using two sodars. With such an experimental system, it has been possible to characterize the forest surface and boundary layers, and to estimate a difference of the turbulent frictional force between two sites differing by the nature of the canopy (forest and bares soil). Figure 34 display the diurnal variation of the horizontal wind direction and speed observed above the two sites at an altitude level of 34 m. The

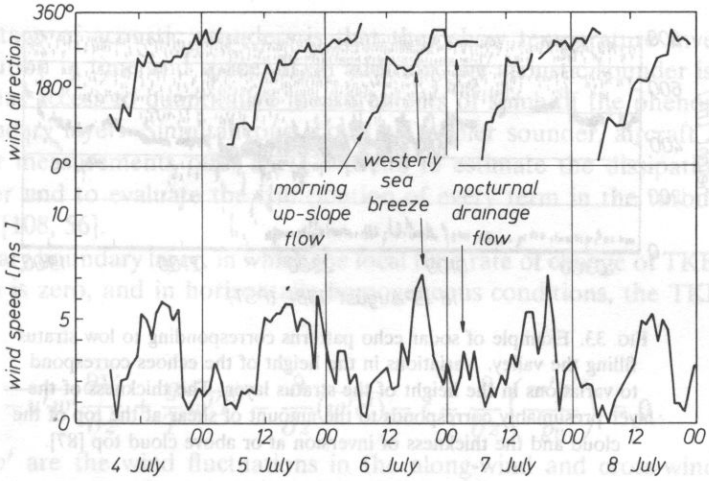

FIG. 31. Diurnal wind cycle, during well-developed sea breeze regime, measured at 150 m above the surface using the Doppler sodar. The sea-breeze, nocturnal drainage, and morning upslope flows are indicated.

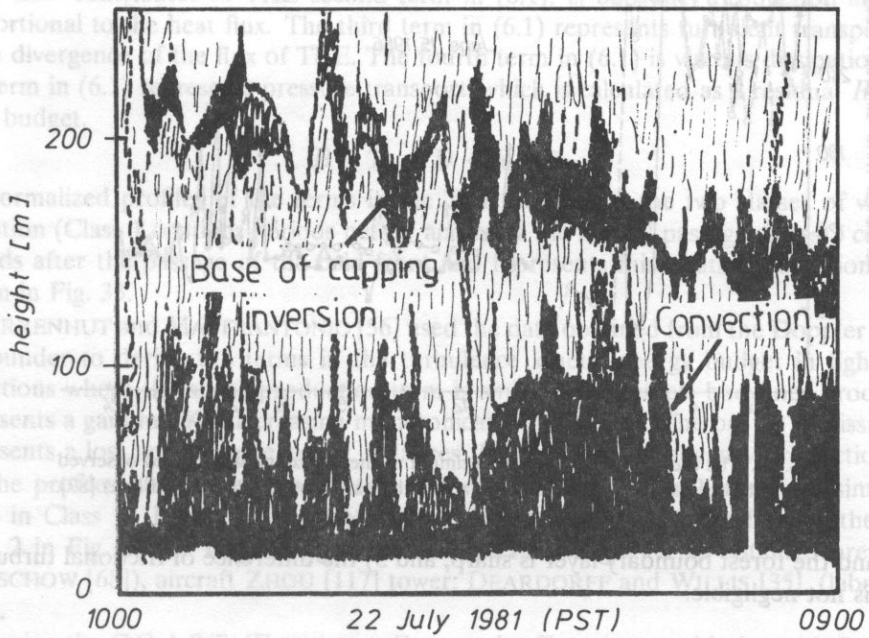

FIG. 32. Example of sodar echo patterns in the case of convection from a heated slope together with a capping inversion [87].

dashed line corresponds to the unforested area and the full line to the forested site. The sodar observations made enable us to conclude that 1) the forest frictional effect depends on the wind regime (magnitude and direction), 2) the transition between the forest surface

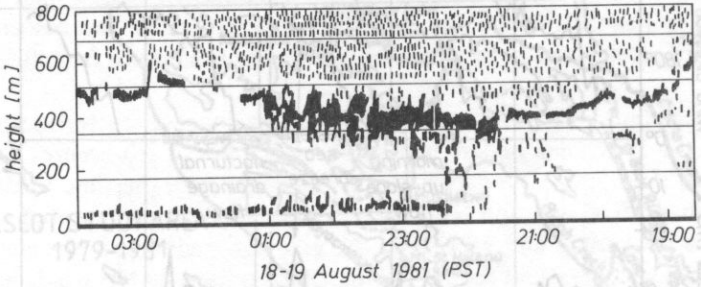

FIG. 33. Example of sodar echo patterns corresponding to low stratus filling the valley. Variations in the height of the echoes correspond to variations in the height of the stratus layer. The thickness of the layer presumably corresponds to the amount of shear at the top of the cloud and the thickness of inversion at or above cloud top [87].

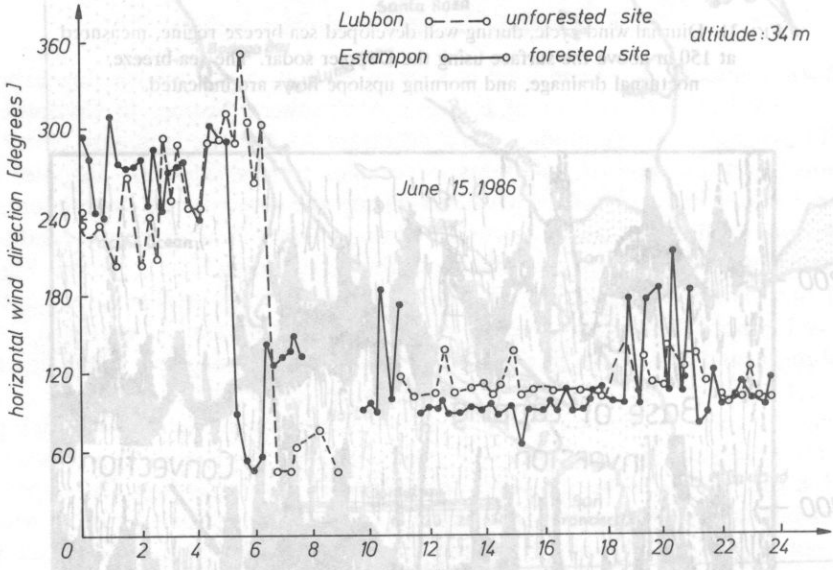

FIG. 34. The diurnal variation of the azimuth of the horizontal wind speed observed above the forested side (full line) and above the base-ground site (dashed line) [87].

layer and the forest boundary layer is sharp, and 3) the difference of frictional turbulence stress is not negligible.

6. Study of the turbulence structure of boundary layer of atmosphere

Knowledge of the turbulence structure associated with temperature inversions is of fundamental importance in boundary-layer modeling and in the study of the diffusion of contaminants.

One advantage of acoustic sounders is that they show temperature inversion layer and their evolution in time and space. If, in addition, the acoustic sounder is a Doppler sounder, one has access to quantitative measurements of some of the phenomens in the planetary boundary layer. Simultaneous acoustic Doppler sounder, aircraft and meteorological tower measurements offer the possibility to estimate the dissipation rate in a convective layer and to evaluate the contribution of every term in the turbulent kinetic energy budget [108, 56].

In a stationary boundary layer, in which the local time rate of change of TKE (turbulent kinetic energy) is zero, and in horizontally homogeneous conditions, the TKE budget is given by [21]

$$-\overline{u'w'}\frac{\partial V}{\partial z} + \frac{g}{T}\overline{w'T'} - \frac{\partial}{\partial z}\overline{(w'e')} - \epsilon - \frac{\partial}{\partial z}\left(\frac{w'p'}{\varrho_0}\right) = 0\,. \tag{6.1}$$

Here u' and v' are the wind fluctuations in the along-wind and cross-wind direction, respectively; p' is the pressure fluctuation and ϱ_0 the air density, w' is wind fluctuation in vertical direction, T' is fluctuation of absolute temperature, T, ϵ is dissipation rate, V is the mean wind.

The first term in (6.1) in shear production, which represents the rate at which the mean flow contributes to TKE second term in (6.1), is buoyancy production and it is proportional to the heat flux. The third term in (6.1) represents turbulent transport and is the divergence of the flux of TKE. The fourth term in (6.1) is viscous dissipation. The last term in (6.1) represents pressure transport, which is calculated as a residual R in the TKE budget.

$$B + T_r + D + R = 0\,. \tag{6.2}$$

Normalized profiles of the terms in the TKE budget for the two classes of weather condition (Class 1 contains periods before and after the frontal passage, Class 2 contains periods after the passage of the cold front and represents fair-weather conditions), are shown in Fig. 35.

GRRENHUT and MASTRANTONIO [56] used the data obtained from the Doppler acoustic sounder to derive the terms in the turbulence kinetic energy budget in light wind conditions where the shear production term is small. In all cases, buoyancy production represents a gain in TKE decreasing monotonically with height. The profile of dissipation represents a loss and to some extent, balances the gain due to buoyancy production.

The profiles of buoyancy production and dissipation in Class 1 are quite similar to those in Class 2. Results of GREENHUT and MASTRANTONIO in the fair weather case Class 2 in Fig. 35 are in good agreement with TKE budget terms obtained previously (LENSCHOW [68]), aircraft ZHOU [117] tower; DEARDORFF and WILLIS [35], (laboratory tank).

During the C.O.A.S.T. (Experiment Cooperative Experiment with Acoustic Sounding Techniques) Doppler sodar and minisodar were used to observation of a mesoscale shear convective. The experiment took place in April/May 1983 in the western port of the Netherlands and typical measurements and instrumental location can be found in Fig. 36.

There was discussed the decomposition of the wind velocity in the presence of mesoscale perturbations and characterized by the turbulent dissipation rate in the presence of mesoscale system.

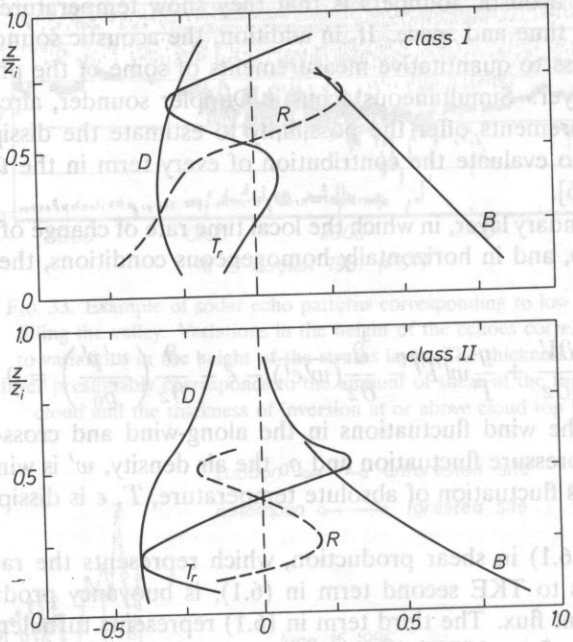

FIG. 35. Normalized profiles of the terms in the turbulence kinetic energy budget for the two classes of weather conditions [56];
$w_* = (g/TQz_i)^{1/3}$ — vertical velocity scaling parameter,
Q_0 is the surface value of $w'T'$, z_i is the inversion height.

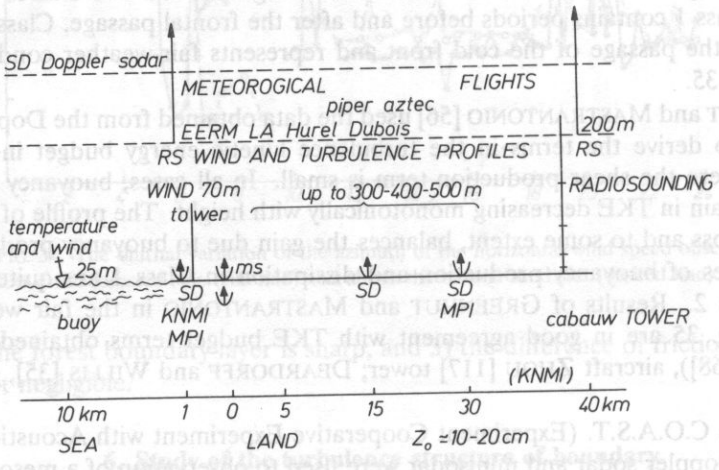

FIG. 36. Scheme of the different kinds of instruments used during COAST experiment and their location along the North-West, South-East transect: distances are indicated from the Dutch Coast SD are the Doppler sodar and RS the radiosoundings [111].

It is difficult to estimate the turbulent dissipation rate by the inertial method in the presence of mesoscale perturbation.

WEILL *et al.* [111] used a Doppler sodar to estimate turbulent dissipation rate using the structure function of velocity fluctuations, averaged on three antennas following WEILL [108]. The turbulent dissipation rate obtained by Weill et al. was two times larger than that expected in the well mixed layer.

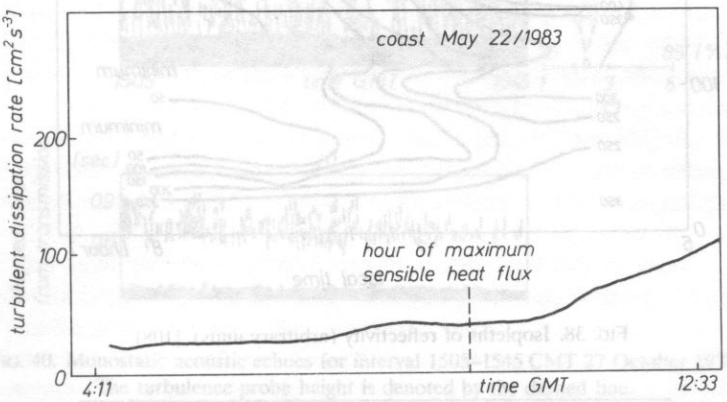

FIG. 37. Turbulence dissipation rate measured with structure function in the mixed layer, the turbulent dissipation rate is average for three antennas. The hour of the maximum of sensible heat flux is indicated [111].

Figure 37 indeed shows that the turbulent dissipation rate increases during the appearance of the mesoscale system, which is certainly due to the mechanical mesoscale momentum production since the sensible heat flux contribution calculated with the sodar vertical velocity variance is fairly smaller after 7.30: of the order of 40 to 50 W/m^2.

Acoustic sounder measurement made during the C.O.A.S.T. demonstrated the capability of 8 sodars to quantity the different perturbations. To go further in such an analysis and to understand correctly the mesoscale organization, a Doppler sodar is not sufficient. WEILL et al. [110] suggest that in future studies, micrometeorological towers should be added at sodar location, to have redundant micrometeorological measurements.

WEILL *et al.* [108] observed the structure of turbulence in an inversion layer in a homogeneous convective field of the planetary boundary layer. By comparison between isopleths of backscattering intensity and of turbulent dissipation rates, they observed that in the early morning, turbulence is advected by mechanical turbulence generated by wind shear. The same mechanism seems to be operating in the case of an inversion layer capping thermal instability, when the convective activity is not too greatly developed. The isopleths of backscattering intensity in Fig. 38 were obtained from backscattering intensity profiles averaged over 13 min.

In Fig. 38 we see the classic signature of the early morning "reflectivity": the reflectivity decreases in the surface layer, reaches a minimum of reflectivity and then increases to a maximum in the inversion layer. The height of the maximum is not very far from the inversion base, and the echo layer top, as observed in Fig. 38, is not the top of the statical stable layer, but the top of the "turbulent mixing layer".

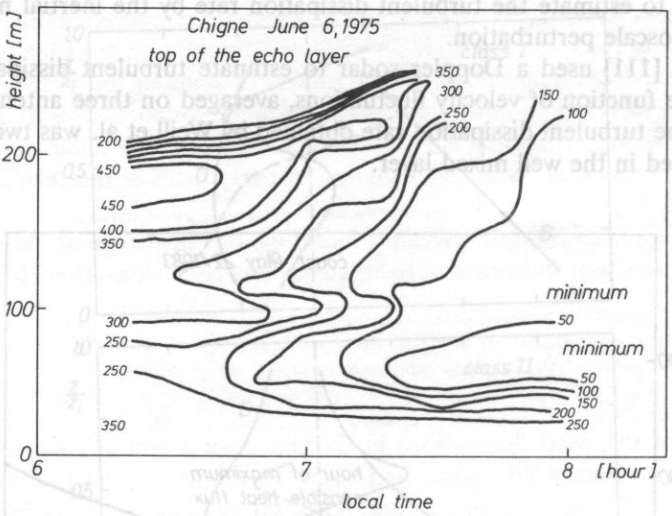

FIG. 38. Isopleths of reflectivity (arbitrary units). [108].

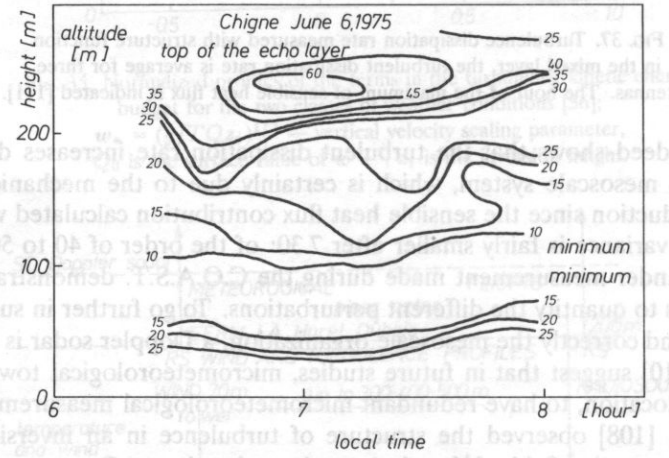

FIG. 39. Isopleths of dissipation rate ($\varepsilon \mathrm{cm}^2\mathrm{s}^{-3}$) [108].

Figure 39 shows that the dynamic structure of the turbulence is very similar to that given by the reflectivity diagram: decreasing turbulent dissipation followed by an increase up to the top of the profile.

The turbulence dissipation rate, ϵ, can also be obtained from the bistatic echo in convective conditions [23]. The facsimile recordings of the monostatic and bistatic returns are shown in Fig. 40a and b, respectively. Profiles of wind speed, temperature and relative humidity across height range of interest, are shown in Fig. 40c. The monostatic echoes indicate only weak and (quite variable) thermal activity in the lowest 100 m of the boundary layer, a region shown to be nearly adiabatic on the potential temperature profile.

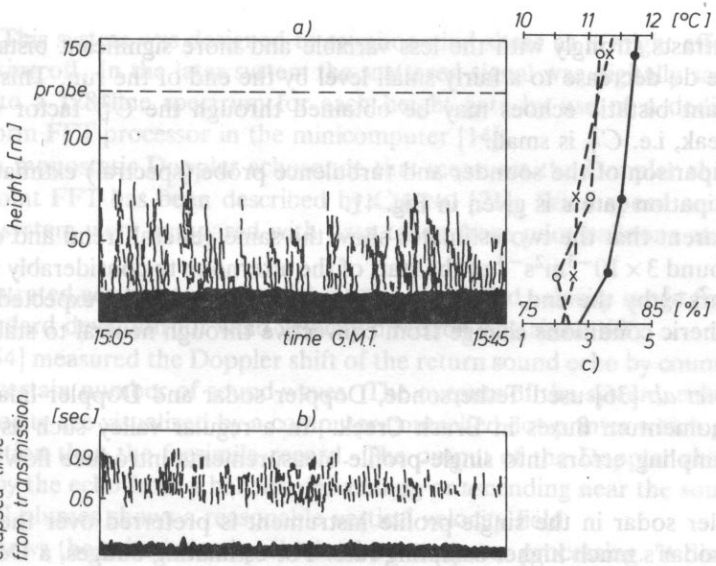

FIG. 40. Monostatic acoustic echoes for interval 1505–1545 CMT 27 October 1975. The turbulence probe height is denoted by the dashed line. b) Bistatic acoustic echoes for the same interval. The ordinate l elapsed time from transmission. c) Balthum profiles of wind speed, potential temperature and humidity. --- wind speed, -×- potential temperature; -o- humidity [23].

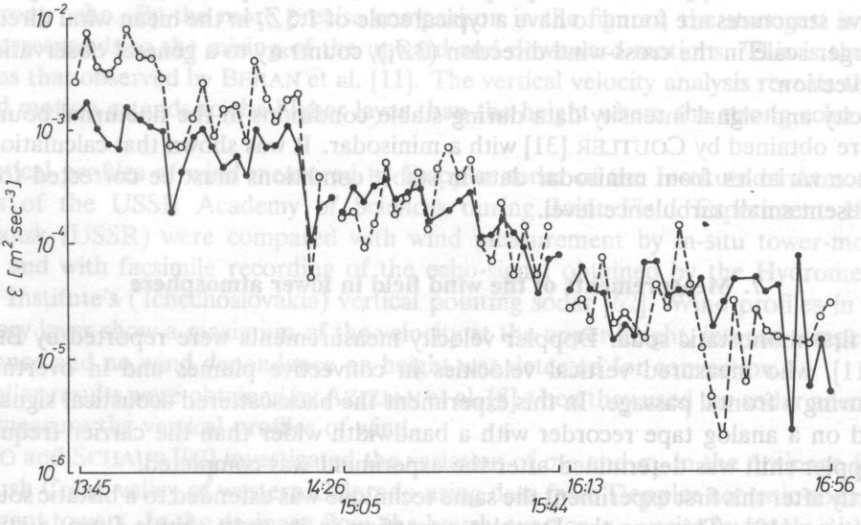

FIG. 41. Time histories of the ϵ estimates from acoustic sounder and turbulence probe on the afternoon 27 October 1975. -o- sounder, --- turbulence probe [23].

This contrasts strongly with the less variable and more significant bistatic echoes although these do decrease to a fairly small level by the end of the run. This clearly shows that significant bistatic echoes may be obtained through the C_V^2 factor when thermal activity is weak, i.e. C_T^2 is small.

The comparison of the sounder and turbulence probe (spectral) extimates of the turbulence dissipation rate ϵ is given in Fig. 41.

It is apparent that the two estimates show the same general trend and decrease from values of around $3 \times 10^{-3} \mathrm{m}^2\mathrm{s}^{-3}$ at the start of the afternoon to considerably smaller values of $\sim 10^{-5} \mathrm{m}^2\mathrm{s}^{-3}$ by the end. This progression complies with the expected variations of ϵ as atmospheric conditions change from convective through neutral to stable during the afternoon.

DOBOSY *et al.* [36] used Tethersonde, Doppler sodar and Doppler lidar to calculate mass and momentum fluxes in Brush Creek. In a regular valley such as Brush Creek unsteady, sampling errors into single-profile measurements introduce flow patterns phenomena.

A Doppler sodar in the single-profile instrument is preferred over the Tethersonde, because of sodar's much higher sampling rate. For estimating budges, a Doppler lidar or equivalent remote sensor is necessary, because single profile measurements were found to have sampling errors which are too large for reliable flux divergence estimates.

The Landes experiment, gathering a dual Doppler radar, a Doppler sodar, radiosoundings and flux measurements performed during three observation periods, provided the opportunity for a study of convective structures in the planetary boundary layers [37]. Using measurements of velocity variances and one-dimensional spectra, the mean behaviour of the convective atmospheric boundary layer is studied in the production subrange. The convective structures are found to have a typical scale of $1.5 Z_i$ in the mean wind direction, and a larger scale in the cross-wind direction ($3 Z_i$), countrary to a general observation of free convection.

Velocity and signal intensity data during stable conditions in the nocturnal boundary layer were obtained by COUTLER [31] with a minisodar. It was shown that calculations of turbulence variables from minisodar data in stable conditions must be corrected for the often present small turbulence level.

7. Measurements of the wind field in lower atmosphere

The first monostatic sodar Doppler velocity measurements were reported by BERAN et al. [11], who measured vertical velocities in convective plumes and in overturning waves during a frontal passage. In this experiment the backscattered acoustical signal was recorded on a analog tape recorder with a bandwidth wider than the carrier frequency. The Doppler shift was determined after the experiment was completed.

Shortly after this first experiment the same technique was extended to a bistatic sounder configuration [12]. This was the Doppler extraction in its most simple form, a straight forward measurement of the frequency of the scattered signal, possible in the acoustic regime because of the low frequencies used.

The feasibility of measuring the profile of the total wind vector from a height of 30 m to over 600 m, even in a noisy airport environment, was demonstrated by BERAN [13]. This system utilized a minicomputer for processing the Doppler voltage desired from the analog

tracking filter. This system was designed to monitor wind shear as it might affect aircraft landing and taking off. In the later system the scattered signal was digitally sampled and transformed into a 128–line spectrum for each height gate by use of a dedicated Fast Fourier Transform FFT processor in the minicomputer [14].

A three-axis monostatic Doppler echosonde that measures the Doppler shift through use of a 100 point FFT has been described by CHONG [21]. Wind speed and direction data from this system were compared with data taken from pilot balloons at heights of 30–500 m.

The demonstrated accuracy was about 1 ms^{-1} over a wind velocity range from 1 to 10 ms^{-1}. The standard deviation for wind velocity direction was about 40°.

HAYASHI [54] measured the Doppler shift of the return sound echo by counting a time duration for a certain number of sound waves. The outputs of the system, echo intensity and vertical velocity are visualized by a computer-controlled dot-printer which gives more minute information than the facsimile record. The output of the Doppler shift analyser was calibrated by the echo from a balloon descending or ascending near the sounder. The case for thermal plumes shows a reasonable vertical velocity field.

Figure 42 shows the echo intensity obtained by computer processing. It distinguished the strong echo area and the weak area; those were not so clear in the facsimile record, even though the darkenning is distorted by photographic reproduction.

Five dark areas are observed about 5, 11, 13, 15 and 17 minutes after 10.00. The derived vertical velocity field is shown in the lower two figures of Fig. 42; the middle figure shows the upward motion and the bottom the downward motion. Each dark area in the top figure (strong echo) corresponds to the dark area in the middle figure (upward motion). Descending air is thermally quiet due to the adiabatic compression and does not give strong echo. By the more precise comparison in the figures, the strongest intensity area corresponds to the mixing of the upward and downward motions. This is the same result as that observed by BERAN et al. [11]. The vertical velocity analysis reveals that the upward motion extends to the higher layer than the height where the strong echo comes back.

Vertical profiles of wind measured by Doppler sodar of the Institute of Atmosphere Physics of the USSR Academy of Sciences during Joint Field Experiment 1981 at Tsimlyansk (USSR) were compared with wind measurement by in-situ tower-mounted sensor and with facsimile recording of the echo-signal obtained by the Hydrometeorological Institute's (Tchechoslovakia) vertical pointing sodar [62]. Wind profiles in stable boundary layer show a maximum of the velocity at the upper height, intense temperature turbulence and no wind dependence on height was detected for convection.

Similar results were obtained by AZIZIAN et al. [8] when they used the sodar anemometer to measure the vertical profiles of wind.

RAO and SCHAUB [92] investigated the variation of σ_Θ and σ_p in the drainage flow in the Brush Creek valley of western Colorado using data from Doppler acoustic sodars and instrument towers. In the drainage flow, the hourly average σ_Θ varies inversely with wind speed according to the relation $\sigma_\Theta \overline{u} \approx 0.7 ms^{-1}$. The vertical standard deviation is much less enhanced by complex terrain than the horizontal standard deviation. The observed σ_p values were predicted fairly well by the local similarity theory.

Acoustic sounder was also used by MCKENDRY and LEWTHWAITE [64] to intensive observations of sumertime up- and down-valley winds in a "dry" valley.

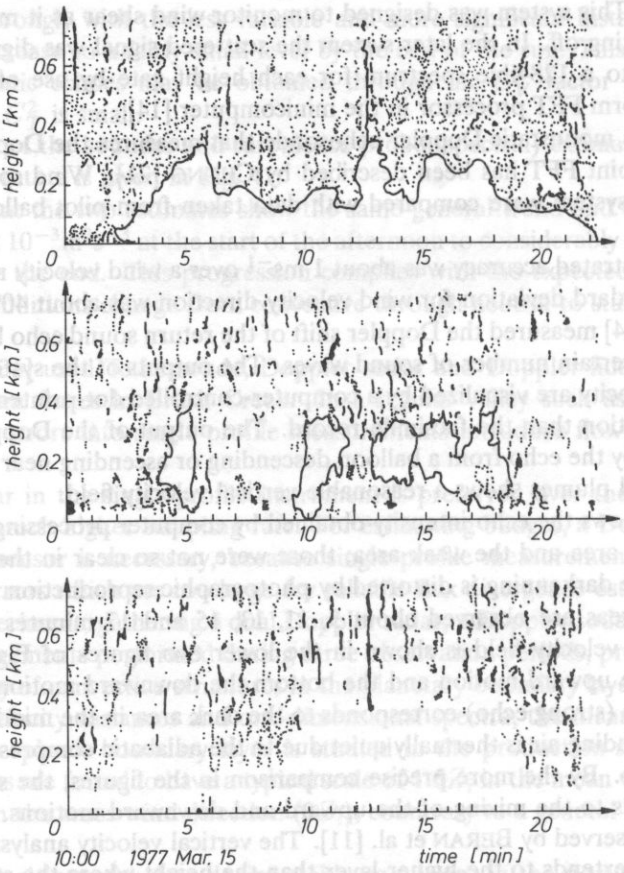

FIG. 42. Computer outputs for a 22 minutes data set 10.00 JST March 15, 1976 [54]. The return echo intensity top upward velocity center and downward velocity bottom.

In the receiver's output the echo signal is combined with noise, mostly of ambient origin, which is often comparable in strength to the signal itself.

Thus, the question arises of defining and measuring a "center frequency" value for the received echoes, representative of the average value of the wind velocity component along the axis of the sodar beam.

There are various ways whereby the "center frequency" is defined and obtained from the sodar echoes [20]. Without attempting to separate the received echo from the noise, this frequency is usually obtained by evaluating the first moment of the filtered spectrum [8] or by finding its peak [62].

The accuracy of wind determination with Doppler sodar was studied by MASTRANTONIO and FIOCCO [82]. The application of the first moment integral to the spectrum of the received echoes in unfavorable signal-to-noise conditions leads to a large systematic, bias and lack of precision. Mastrantonio and Fiocco used a two-step procedure, whereby the spectrum of the echo is first localized and then the actual value of its center frequency is determined. A comparison of the precision, obtained in the measurement of vertical

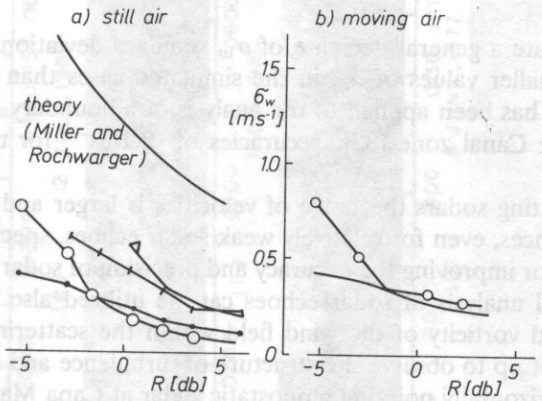

FIG. 43. Precision obtained by various methods as a function of R (ratio of the signal to noise). Open circles simulated echo two-step procedure. Solid circles: simulated echo standard analysis. Open triangles: real echo, two-step procedure. Solid triangles: real echo standard analysis [82].

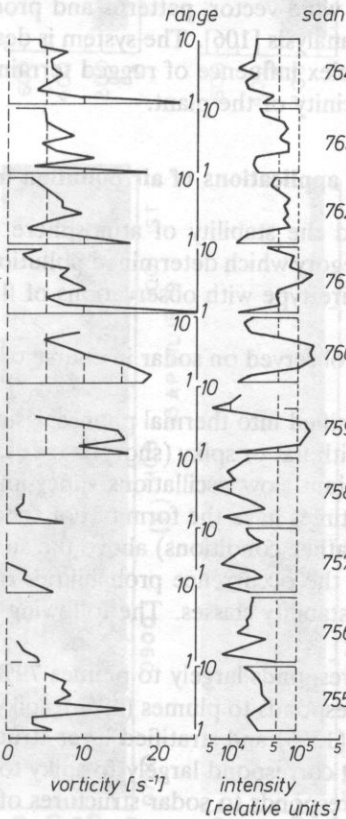

FIG. 44. Intensity (right profiles) and vorticity (left profiles) for the screens 755–764 [40].

wind velocity (w) by various methods as a function of ratio of the signal to noise (R) is shown in Fig. 43.

The curves indicate a general decrease of σ_w standard deviations with an increase in the ratio R, and smaller values of σ_w in the simulated cases than the real cases. This two-step procedure, has been applied to the analysis of a boundary-layer equipment carried out in the Suez Canal zone [82]: accuracies of $0.1 \mathrm{ms}^{-1}$ for the vertical velocities were claimed.

For oblique-pointing sodars the range of velocities is larger and the spectrum wider. For these circumstances, even for relatively weak sodar echoes, spectral two-step analysis provides a method for improving the occuracy and precision of sodar wind measurements.

Detailed spectral analysis of sodar echoes can be utilized also to yield information on the structure and vorticity of the wind field within the scattering volume [40]. The experiments were set up to observe the structure of turbulence and to measure the noise levels by using a horizontally pointing monostatic sodar at Capa Margherita 4559 m.a.s.l. in the Alps. Figure 44 shows the intensity and vorticity profiles obtained there.

Notice that for a monostatic sodar the intensity profiles give an indication of the thermal turbulence, while the vorticity profiles give an indication of dynamical turbulence.

A special system for real-time analysis of local wind patterns has been installed at the Emergency Operations Facility for Diablo Canyon Nuclear Power Plant. Doppler — sounder data produces spatial wind-vector, patterns and producing real-time displays of local fields based on objective analysis [106]. The system is designed to provide an interim solution to addresing the complex influence of rugged terrain and a coastal environment on the wind patterns in the vicinity of the plant.

8. Echosonde applications of air pollution meteorology

SIGNAL *et al.* [100] studied the stability of atmosphere to give information on the prevailing Pasquill stability category which determined pollution dispension. This was done by comparing the echo structure type with observations of fluctuations in the horizontal wind direction.

Various types of structures observed on sodar in course of their observations are given in Fig. 45.

These structure can be classified into thermal plumes, rising layer with thermal plumes below it, surface based layer with flat or spiky (short or tail) top, and stratified layer structure with or without the medium slow oscillations super-imposed over it (stable atmosphere) which may oven sometimes have the form of dot echo structures (stray or regular formed under moist stable weather conditions) above the surface based layer.

The plot in Fig. 46 shows the occurrence probabilities of the various types of sodar structures for the six Pasquill stability classes. The following is clearly seen from the plot of Fig. 46:

1) stability category A corresponds largely to plumes 79%;

2) stability category B corresponds to plumes (49%), spiky top surface layer structures (34%), rising layer structures (13%) and stratified layer structures (4%);

3) stability categories C, D correspond largely to spiky top layer structures;

4) stability category F corresponds to sodar structures of flat top surface-based layer (41%), spiky top surface-based layer (23%), stratified layer (24%) and plumes (6%).

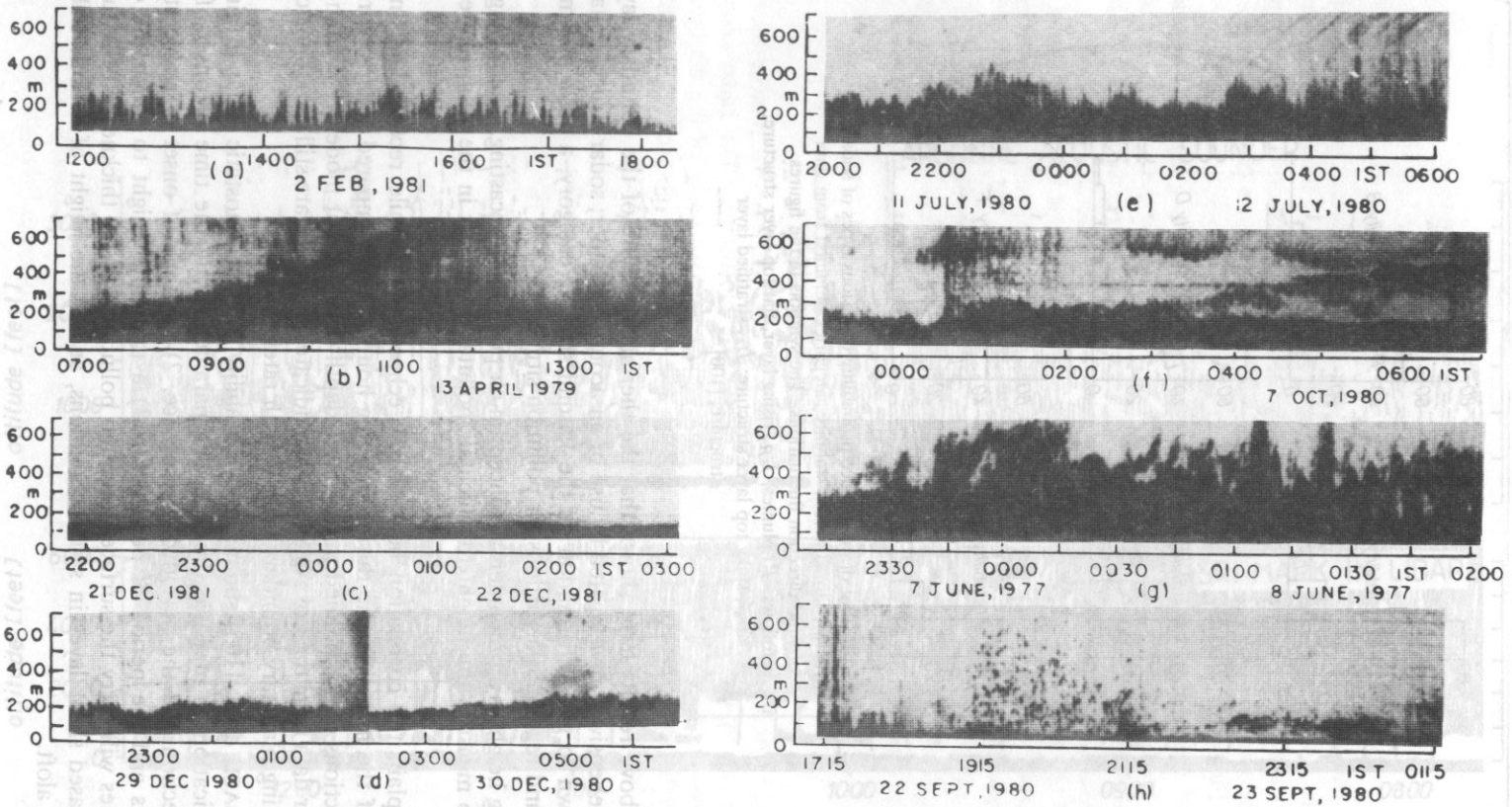

FIG. 45. Typical structures seen on sodar. a) Thermal plumes b) Rising nocturnal inversion layer with plume structure below it. c) Surface based stable layer with flat top. d) Surface based stable layer with short spikes at the top. f) Stratified layer structure without undulations. g) Stratified layer structure undulating. h) Stratified layer structure (dot echoes) [100].

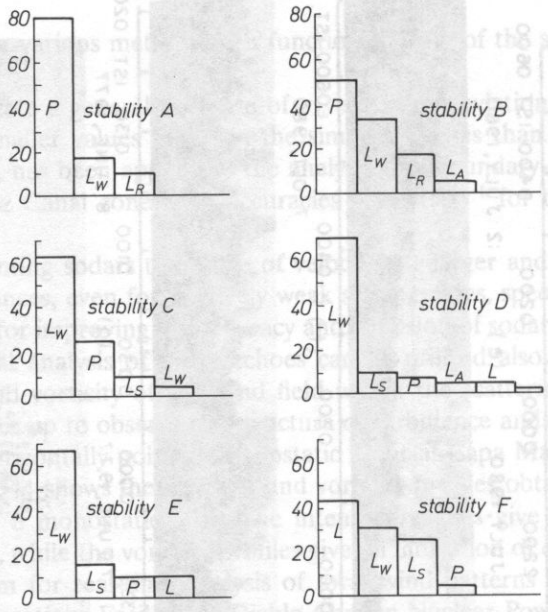

FIG. 46. Plot of occurrence probability of various types of sodar structures for different stability categories obtained from data of wind direction fluctuations. The symbols in the figures are as follows: P, plumes, L_R, rising layer, flat top layer structure; L_w, spiky top layer structure; L_s, stratified layer structure; [100].

The above results have shown that the thermal structure of the boundary layer can be comprehensively investigated by use of an acoustic sounder; sodar structure have also been shown to give information on the Pasquil stability category, a basic parameter to monitor and regulate hazzardous air pollution situations.

Mixing height is a fundamental concept in air pollution forecasting. The mixing height is used to measure the height to which air pollutants will mix in the atmosphere [3, 99, 55].

To explain the correlation between the echosonde facsimile records and analytical models of the inversion rise during morning hours, Shaw compared sodar records with the predictions of a simplified mixing layer depth development model [84]. Comparison with sodar data from the Los Angeles basin indicates that there are still some shortcomings in modelling planetary boundary layer growth rates.

TOMBACH *et al.* [105] summarized the ability of the monostatic sodar in air pollution application to measure the following parameters: 1) the time of onset of unstable convection and the period of persistence, 2) the time of onset of stable stratified conditions and the period of persistence, 3) a minimum height to which the convective plumes will carry the surface-generated pollutants, 4) the thickness of the turbulent ground-based shear layer in stable conditions, and 5) the height of various stable and inversion aloft.

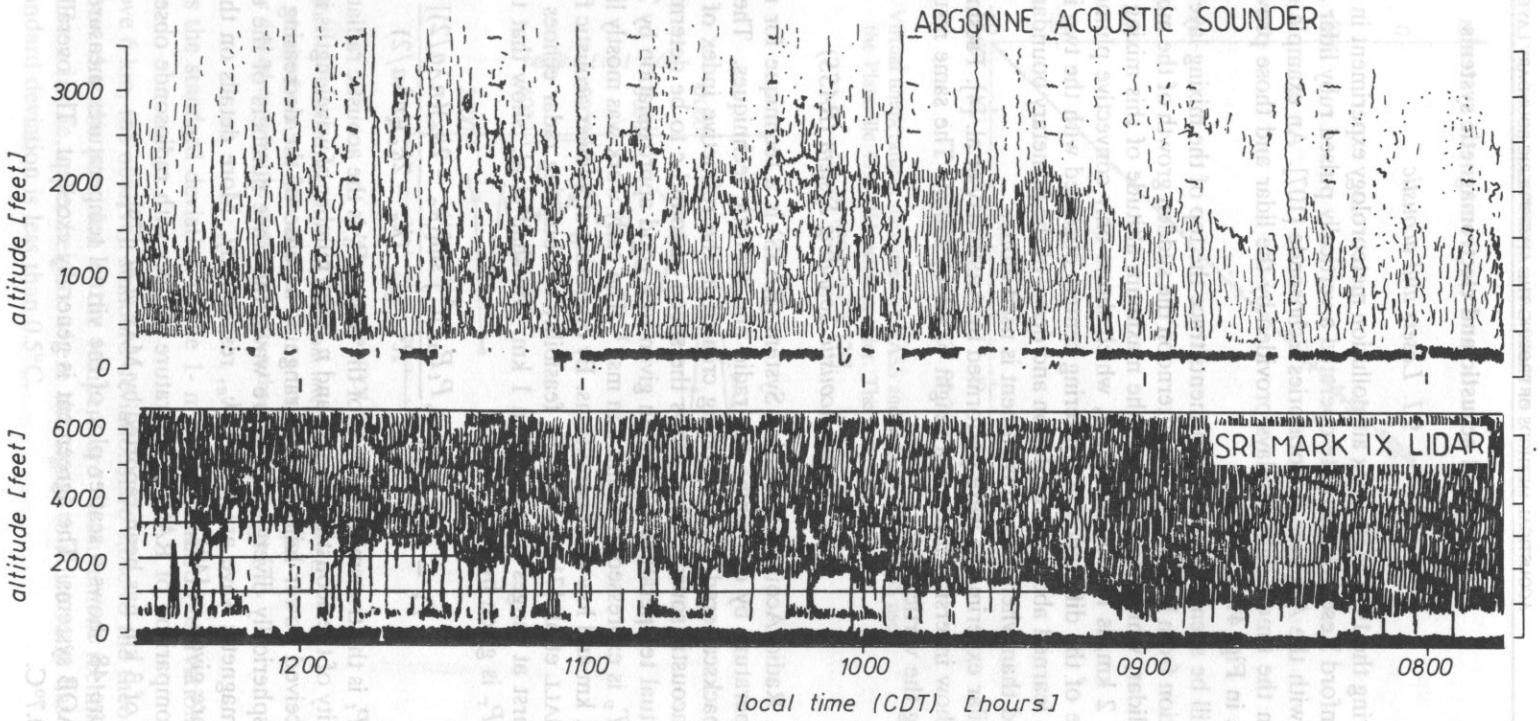

FIG. 47. Comparison of sodar (top panel) and lidar (bottom panel) display of the growth of a convectively mixed layer [107].

9. Hybrid acoustic and electromagnetic systems

9.1. Lasers and acoustic

During the 1971 Metromex air pollution meteorology experiment in the St. Louis area, the Stanford Research Institute operated a vertically pulsed ruby lidar and compared the results with the Argonne Laboratories Echosonde [107]. An example of the comparison between the time height displays provided by the lidar and those provided by the sodar is given in Fig. 47.

It will be seen that both instruments trace the top of the mixing layer as it is heated by convection from below, but that afternoon the sudden growth of the mixed layer recorded by the lidar, which clearly shows the maximum altitude of this mixing layer depth to be near 1, 2 km, is lost by the sodar, which shows only convective plumes to about 1 km. Because of the difference in scattering centers observed with the two instruments, much more is learned about the evolution and decay of the planetary boundary layer when both are used than when either instrument is used alone.

Similar experiments were performed by ARSHINOV et al. [4]. Facsimile records of the sodar show inversion layer at a height of about 250 m. The same results were obtained by using the vertical lidar.

9.2. Radio Acoustic Sounding System (RASS)

The Radio Acoustic Sounding System (RASS) is a technique for remote measuring of temperature by combining the radio and acoustic techniques. The radar senses the signal backscattered from a grating created in the refractive index of the air by a high power acoustic source. This allows the speed of sound c to be determined [see 89, 78]. The virtual temperature T_v is then given to a good approximation by $T_v = (c/20.047)^2$, where T_v is expressed in K and c in ms^{-1}. The early work was mostly limited to altitudes below 1 km and low wind conditions. By operating at a lower acoustic frequency (85 Hz), MARSHALL et al. [71] proved the feasibility of obtaining radar echoes from the acoustic tone burst at ranges of more than 1 km. Marshall et al. show that the received radar power P_r is given by

$$P_r = 1.38 \times 10^{-16} \frac{P_t P_a g n^2}{R^2} \left\{ \frac{\sin[(k_a - 2k_e)(n\lambda a/2)]}{(k_a - 2k_e)(n\lambda a/2)} \right\} \tag{9.1}$$

where P_t is the transmitted power of the radar, P_a is the acoustic radiated power, g is the directivity of the acoustic antenna, and n is the number of wavelengths in a acoustic pulse. The received power falls off with range R because of the decreasing acoustic intensity in the spherically diverging pressure wave; the wave numbers of the acoustic wave and electromagnetic wave are k_a and k_e, respectively. More details on the development of RASS are given in [49].

A comparison of RASS temperature profiles with radiosonde observation RAOB to heights of 3 km has been reported by MAY *et al.* [79].

Figure 48 shows a scatter plot of the virtual temperatures measured with the RASS and RAOB systems. The agreement is generally excellent. The overall rms difference is about 0.7°C.

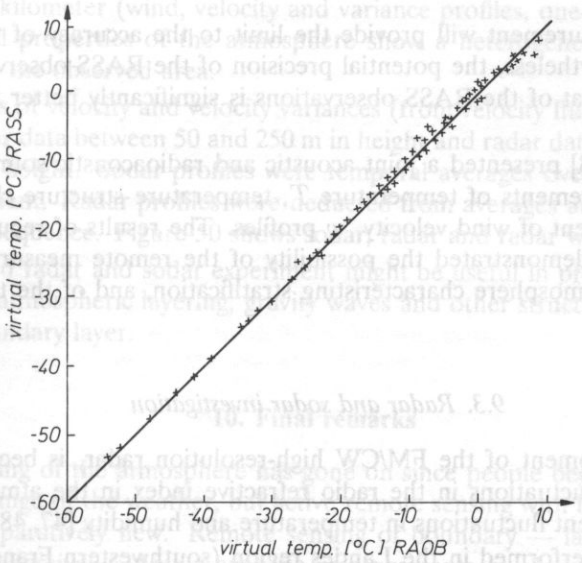

FIG. 48. Virtual temperatures measured by RASS and RAOB. The RASS used the Plateville 49.8 MHz wind profiler. The rms difference is about 0.7°C [79].

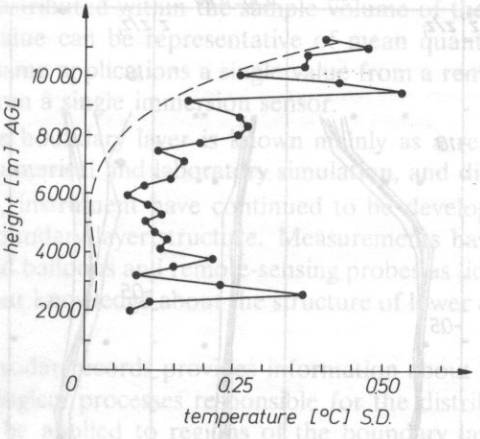

FIG. 49. Standard deviation of the 1-min interval measurements obtained with the Plateville 49.8 MHz profiler against height. The dashed curve on the plots represents a theoretical estimate [79].

Figure 49 shows the standard deviation of the 1- min temperature observations as a function of height.

At altitudes above 6 km, the observed standard deviations are close to the theoretical expectation, and show that the precision of the temperature measurement technique is better than 0.2°C. Even in the upper heights where the signal-to-noise ratio has fallen below 0 dB, the standard deviation is less than 0.5°C.

The former measurement will provide the limit to the accuracy of the temperature measurement. Nevertheless, the potential precision of the RASS observations is significantly better than that of the RASS observations is significantly better than that of the present radiosondes.

AZIZYAN *et al.* [8] presented a joint acoustic and radioacoustic sounding system for simultaneous measurements of temperature T, temperature structure characteristic C_T^2 and vertical component of wind velocity, w profiles. The results of regular observations at autumn of 1980 demonstrated the possibility of the remote measurements of main parameters of the atmosphere characteristing stratification, and of the turbulent regime of boundary layer.

9.3. Radar and sodar investigation

With the development of the FM/CW high-resolution radar, is became possible to monitor fine-scale fluctuations in the radio refractive index in the atmosphere, caused principally by turbulent fluctuations in temperature and humidity [47, 48].

An experiment performed in the Landes region (southwestern France) utilized dual Doppler radar (Ronsard system) and the Doppler sodar system in the experiment on clear air convection [48]. It provided the opportunity to develop a method for the spatial study of atmospheric structure in the PBL: the mean characteristic of the flow structures at scales

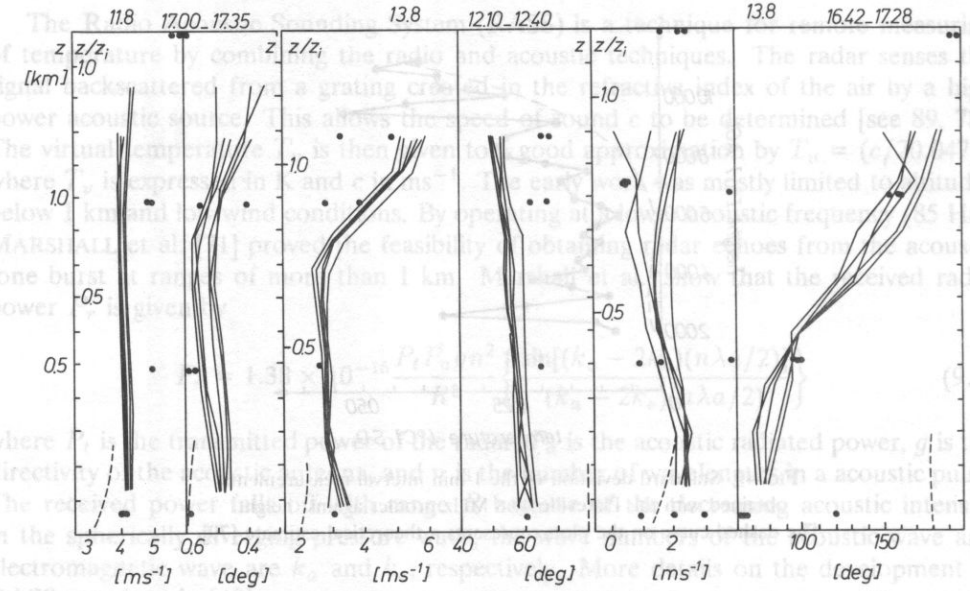

FIG. 50. Mean horizontal wind profiles during the three experiments on 11 August (11–8), 13 August noon and afternoon (13–8). Hours are indicated LST. The solid lines show the profiles of speed and direction for each sequence of 5 or 6 min, from radar data: the dashed line shows the sodar profiles taken over 20 min deviation. The directions are measured from north, Z_i = inversion height [38].

larger than one kilometer (wind, velocity and variance profiles, one-dimensional velocity spectra). Spatial properties of the atmosphere show a heterogeneity of the horizontal wind field inside the observed area.

Mean profiles of velocity and velocity variances (from velocity fluctuations) were computed using sodar data between 50 and 250 m in height and radar data from 100 or 150 m to $\sim$ 1000 m in height. Sodar profiles were temporal averages over half and hour during each experiment. Radar profiles were deducted from averages across each horizontal plane for every sequence. Figure 50 shows sodar, radar and radar wind profiles.

The combined radar and sodar experiment might be useful in providing a more complete picture of atmospheric layering, gravity waves and other structures characteristic of the dynamic boundary layer.

10. Final remarks

Remote sensing of the atmosphere has gone on since people began watching the sky for signs of a change of the weather, but active remote sensing with intentionally directed radiation is comparatively new. Remote sensing of boundary — layer variables can be done actively or passively. Active acoustic measurements involve transmitting acoustic radiation to the region and measuring the portion of radiation that is returned from the region to sodar. Remote acoustic measurements are spatial averages over volumes that depend on the parameters of the sodar; remote sensing is suitable if spatial averages are desired. A single reading from a sodar's record is equivalent to the average of an ensemble of in situ instruments distributed within the sample volume of the remote sensor. Thus, the acoustical sensed value can be representative of mean quantity than a single-point measurement, and for same applications a single value from a remote sensor can replace a time average value from a single immersion sensor.

The structure of the boundary layer is known mainly as a result of combination of observational studies, numerical and laboratory simulation, and dimensional analysis.

In the last 40 years, instrument have continued to be developed for improving our understanding of the boundary-layer structure. Measurements have been obtained from towers, free and tethered balloons and remote-sensing probes as lidars, radars and sodars. The important part of our knowledge about the structure of lower atmosphere came from sodar studies.

The observation of sodar records provides information about the atmospheric mean fields and the meteorological processes responsible for the distribution of such echoes. Acoustic sounders can be applied to regions of the boundary layer, where regular access by other means is difficult. Due to its usefulness and relatively low cost, sodars are very interesting scientific instruments. The sodar outputs provide estimation of turbulence, shear dynamic instabilities and area-averaged surface parametrizations. The sodar measurement indicate how these measurements can be utilized to investigate physical processes important in the lower atmosphere.

Sodars have operated in diverse environments, ranging from the polar regions to the tropical oceans and new opportunities are still appearing. Application of conventional sodars and minisodars to studies in complex terrain in recent years is only one example of the potential expansion of sodar technology.

References

[1] S.K. AGGARWAL, S.P. SINGAL, R.K. KAPOOR, B.B. ADIGA, *A study of atmospheric structures using sodar in relation to land and sea-breezes*, Boundary Layer Meteorol., **19**, 361–371 (1980).

[2] A.W. ANDRIANOV, H.A. ARMANOV, W.I. WETROV, W.A. KALCY, *Measurement of the characteristics acoustical signal for vertical sounding of boundary layer of the atmosphere* [in Russ.], Radiotechnika i elektronika, **9**, 1801–1809 (1980).

[3] R. ARON, *Mixing height-an inconsistent indicator of potential air pollution concentrations*, Atmos. Envir. **17**, 2193–2197 (1983).

[4] J.F. ARSHINOV, S.M. BUBROVNIKOV, *Remote measurement of temperature vertical profiles in atmosphere by lidar*, 7th. Simp. on Laser and Acoustic Sounding of Atmosphere, Tomsk 1982.

[5] D.N. ASIMAKOPOVLOS, T.J. MOULSLEY, C.G. HECHIS, D.P. LALAS, J. GAYNOR, *Quantitative low-level acoustic sounding and comparison with direct measurements*, Boundary-Layer Meteorol., **27**, 1–26 (1983).

[6] M. AUBRY, *Measurement of the total attenuation of acoustic waves in the turbulent atmosphere*, J. Geophys. Res., **79**, 5598–5606 (1974).

[7] T. AZRIAN, M.A. KALLISTRATOVA, F. MARTWEL, I. PETENKO, N. TIME, *Measurement of wind profile by sodar anemometer* [in Russ.] Fiz. Atm. Ok., **18**, 100–104 (1982).

[8] G.V. AZIZYAN, V. BELYAVSKAYA, M.A. KALLISTRATOVA, I.V. PETENKO, *A joint acoustic and radioacoustic sounding of the atmospheric boundary layer* [in Russ.], Fiz. Atm. Ok., **18**, 1036–1042 (1982).

[9] P. BACCI, C. GIRAUD, A. LONGHETTO, R. RICHIHRDONE, *Acoustic sounding of land and sea-breezes*, Boundary-Layer Meteorol., **28**, 187–192 (1984).

[10] A.C.M. BELJAARA, *Verification of Doppler sodar measurements, Nederlands Meteorologisch Institut*, De Bilt 1985.

[11] D.W. BERAN, C.G. LITTLE, B.C. WILLMARTH, *Acoustic Doppler measurements of vertical velocity in the atmosphere*, Nature, **230**, 160–162 (1971).

[12] D.W. BERAN, B.C. WILLMARTH, *Doppler winds from a bistatic acoustic sounder*, Proc. 7th Inst. Symp. Remote Sensing of the Envir., 1971, 1699–1714, Mich. Press.

[13] D.W. BERAN, B.C. WILLMARTH, F.C. CARSEY, F.F. HALL, *An acoustic Doppler wind measuring system*, J. Acoust. Soc. Am., **55**, 334–338 (1974).

[14] D.W. BERAN, P.A. MANDICS, A.J. BEDARD, R.G. STRAUCH, *A wind shear and gust front warning system*, Proc. 7th Conf. Aerospace and Aeronautical Meteorol. Boston 1976.

[15] D. BLOKHINTZEV, *The propagation of sound in a inhomogeneous and moving medium*, J. Acoust. Soc. Am., **18**, 329–341 (1946).

[16] E.H. BROWN, S.F. CLIFFORD, *On the total attenuation of sound by turbulence*, J. Acoust. Soc. Am., **58**, 788–794 (1976).

[17] E.H. BROWN, F.F. HALL, *Advances in atmospheric acoustics*, Rev. Geoph. Space Phys., **16**, 47–104 (1978).

[18] E.H. BROWN, F.F. HALL, *Advances in atmospheric acoustics*, Rev. Geophys. Space Phys., **16**, 47–100 (1978).

[19] E.H. BROWN, *Turbulent spectral broadening of backscattered acoustic pulses*, J. Acoust. Soc. Am., **56**, 1398—1406 (1974).

[20] J.A. BUSINGER, *Atmospheric turbulence and air-pollution modeling*, Dodrecht 1982.

[21] M. CHONG, *Measure des profil de vent par sodar Doppler*, Note Tech. CRPE/22, 1976, France.

[22] S.J. CAUGHEY, R. RAYMENT, *High-frequency temperature fluctuations in planetary boundary layer*, Boundary-Layer Meteorol., **4**, 211–264 (1977).

[23] S.J. CAUGHEY, B.A. CREASE, R.S. COLE, D.N. ASIMAKOPOULOS, T.J. MOULSLEY, *Quantitative interpretation of acoustic echoes from the planetary boundary layer*, Radio Electr. Eng., **50**, 598–610 (1980).

[24] S.J. CAUGHEY, C.J. READINGS, *An observation of waves and turbulence in the earth's boundary layer*, Boundary-Layer Meteorol., **9**, 279–296 (1975).

[25] S.J. CAUGHEY, B.A. CREASE, D.N. ASIMAKOPOULOS, R.S. COLE, *Quantitative bistatic acoustic sounding of the atmospheric boundary layer*, Quart. J. R. Met. Soc., **104**, 147–161 (1978).

[26] S.F. CLIFFORD, E.H. BROWN, *Propagation of sound in a turbulent atmosphere*, J. Acoust. Soc. Am., **48**, 1123–1127 (1970).

[27] D.H. LENSCHOW, *Probing the atmospheric boundary layer*, Amer. Met. Soc., 1986.

[28] S.F. CLIFFORD, E.H. BROWN, *Acoustic scattering from a moving turbulent medium*, J. Acoust. Soc. Amer., **55**, 929–933 (1974).

[29] S.F. CLIFFORD, E.H. BROWN, *Excess attenuation in echosonde signals*, J. Acoust. Soc. Am., **67**, 1967–1973 (1980).

[30] R.S. COLE, D.N. ASIMAKOPOULOS, T.J. MOUSLEY, S.J. CAUGHEY, B.A. CREASE, *Some aspects of the construction and use of atmospheric acoustic sounders*, Radio and Electr. Eng., **50**, 585–597 (1980).

[31] R.I. COOTLER, *A case study of turbulence in the stable nocturnal boundary layer*, Boundary-Layer Meteorol., **52**, 75–91 (1990).

[32] B.A. CREASE, S.J. CAUGHEY, D.T. TRIBBLE, *Information on the thermal structure of the atmospheric boundary layer from acoustic sounding*, Meteorological Magazine, **106**, 42–55 (1977).

[33] R.S. COLE, *Quantitative interpretation of acoustic echoes from the planetary boundary layer*, Radio and Electr. Eng., **50**, 508–610 (1980).

[34] R.F. DAVEY, *A comparison of Doppler sodar antenna configurations used for horizontal wind measurement*, J. Acoust. Soc. Am., **63**, 1335–1341 (1978).

[35] J.W. DEARDORF, G.E. WILLIS, *Further results from a laboratory model of the convective planmetary boundary layer*, Boundary-Layer Meteorology, **32**, 205–236 (1985).

[36] R.J. DOBOSY, K. SKANDAR RAO, J.W. PRZYBYLOWICZ, R.M. ECKMAN, R.P. HOSKER, *Mass and momentum balance in the Bruch Creeke drainage flow determined from single-profile data*, J. Appl. Meteorol., **28**, 467–476 (1989).

[37] L. EYMARD, A. WEILL, *Investigation of clear air convective structures, in the PBL using a dual Doppler radar and a Doppler sodar*, J. Appl. Meteorol., **21**, 1891–1906 (1982).

[38] L. EYMARD, A. WEILL, *A study of gravity waves in the planetary boundary layer by acoustic sounding*, Boundary-Layer Meteorol., **17**, 231–245 (1979).

[39] G. FIOCCO, G. MASTRANTONIO, *Character of the air flow inferred from detailed spectral analysis of acoustic sounder echoes*, J. Acoust. Soc. Am., **74**(6), 1861–1865 (1983).

[40] J.E. GAYNOR, *Acoustic Doppler measurement of atmospheric boundary layer velocity structure functions and energy dissipation rates*, J. Appl. Meteorol., **16**, 148–155 (1977).

[41] J.E. GAYNOR, P.A. MANDICS, *Analysis of the tropical marine boundary layer during GATE using acoustic sounder data*, Monthly Weath. Rev., **106**, 223–232 (1978).

[42] J.E. GAYNOR, P.A. MANDICS, *Analysis of the tropical marine boundary layer during GATE using acoustic sounder data*, Month. Weat. Rev., **106**, 223–230 (1978).

[43] T.M. GEORGES, S.F. CLIFFORD, *Acoustic sounding in a refracting atmosphere*, J. Acoust. Soc. Amer. **52**, 1397–1405 (1972).

[44] T.M. GEORGES, S.F. CLIFFORD, *Estimating refractive effects in acoustic sounding*, J. Acoust. Soc. Am., **55**, 934–936 (1974).

[45] G.W. GILMAN, *Reflection of sound signals in the troposphere*, J. Acoust. Soc. Am., **18**, 274–283 (1946).

[46] E.E. GOSSARD, J.M. RICCHTER, D. ATLAS, *Internal waves in the atmosphere from high resolution radar measurements*, J. Geophys. Res. **75**, 903–913 (1970).

[47] E.E. GOSSARD, R.B. CHADWICK, W.D. NEFF, K.P. MORAN, *The use of ground-based Doppler radars to measure gradients, fluxes and structure parameters in elevated layer*, J. Appl. Meteorol., **21**, 211–226 (1982).

[48] E.E. GOSSARD, R.B. CHADWICK, T.R. DETHAN, J. GAYNOR, *Capability of surface-based clear-air Doppler radar for monitoring meteorological structure of elevated layers*, J. Clim. Appl. Meteorol., **23**, 474–485 (1984).

[49] A.S. GURIANOV, *Radio-acoustic sounding of the atmosphere*, Obminsk, USSR, 1982.

[50] F.F. HALL, J.W. WESCOTT, *Acoustic antennas for atmospheric echo sounding*, J. Acoust. Soc. Am., **56**, 1376–1382 (1974).

[51] F.F. HALL et al., *Convective plumes in the planetary boundary layer, investigated with an acoustic echo sounder*, J. Appl. Meteorol., **14**, 513–523 (1972).

[52] R.J. HARTMAN, *Wave propagation in a statified shear flow*, J. Fluid Mech., **71**, 89–104 (1975).

[53] D.A. HAUGEN, *Measuring temperature structure parameter profiles with an acoustic sounder*, J. Appl. Meteorol., **17**, 895–899 (1978).

[54] H. HAYASHI, O. YOKOYAMA, *Acoustic Doppler measurements of vertical velocity in the atmosphere*, J. Met. Soc. Japan, **56**, 516–521 (1978).

[55] G.C. HOLZWORTH, *Mixing depths, wind speeds and air pollution potential for selected locations in the United States*, J. Appl. Meteorol., **6**, 1039–1044 (1967).

[56] G.K. GREENHUT, G. MASTRANTONIO, *Turbulence kinetic energy budget profiles derived from Doppler sodar measurements*, J. Appl. Meteorol., **28**, 99–106 (1989).

[57] H. JURY, G. SPENCER–SMITH, *Doppler sounder observations of trade winds and sea-breezes along the African west coast near* 34°S, 19°E, Bounday-Layer Meteorol. **44**, 373–405 (1988).

[58] J.C. KAIMAL, *Turbulence structure in the convective boundary layer*, J. Atmos. Soc., **33**, 2152–2169 (1976).

[59] J.C. KAIMAL, J.A. BUSINGER, *Case studies of a convective plume and dust devil*, J. Appl. Meteorol., **17**, 723–734 (1978).

[60] J.C. KAIMAL, *Estimative the depth of the convective boundary layer*, J. Appl. Meteorol., **21**, 1123–1120 (1982).

[61] M.A. KALLISTRATOVA, V.I. TATARSKII, *Acousting for wind turbulence in the calculation of sound scattering in the atmosphere*, Sov. Phys. Acoust., **6**, 503–505 (1960).

[62] M.A. KALLISTRATOVA, J. KEDER, I.V. PETENKO, N. TIME, *Wind profile measurements by Doppler sounder in the stable and convective boundary layer* [in Russ.], Fiz. Atm. Ok., **21**, 492–497 (1985).

[63] M.A. KALLISTRATOVA, *The measuring of the statistical characteristics of the echoes for acoustical sounding of atmosphere* [in Russ.], Fiz. Atm. Ok., **22**, 987–990 (1986).

[64] I.G. MCKENDRY, E.W. LEWTHWAITE, *The vertical structure of summertime local winds in the Wright Valley, Antarctica*, Boundary-Layer Meteorol., **51**, 329–342 (1990).

[65] M.J. IGHTHILL, *On the energy scattered from the interaction of turbulence with sound or shock waves*, Proc. Combridge Philos. Soc., **49**, 531–538 (1953).

[66] C.G. LITTLE, *Acoustic methods for the remote probing of the lower atmosphere*, Proc. IEEE, **57**, 571–578 (1969).

[67] C.G. LITTLE, *Status of remote sensing of the troposphere*, Bull. Am. Meteorol. Soc., **53**, 936–949 (1972).

[68] D.H. LENSCHOW *et al.*, *Mean-field and second moment, budgets in a baroclinic, convective boundary layer*, J. Atmos. Sci., **37**, 1313–1326 (1980).

[69] A.S. MONIN, *Characteristic of the scattering of sound in a turbulent atmosphere*, Sov. Phys. Acoust., **7**, 370–373 (1962).

[70] A.S. MONIN, A.M. YAGLOM, *Statistical fluid mechanics*, Cambridge Mass, 1971.

[71] J.M. MARSHALL, A.M. PETERSON, A.A. BARNES, *Combined radio-acoustic sounding system*, Appl. Opt., **11**, 108–112 (1972).

[72] C. MAZAODIER, A. WEILL, *A method of determination of dynamic influence of the forest on the boundary layer using two Doppler sodars*, J. Appl. Meteorol., **28**, 705–710 (1989).

[73] T.J. MOUSLEY, D.N. ASIMAKOPOULOS, R.S. COLE, B.A. CREASE, *Design of arrays for acoustic sounder antennas*, J. Phys. E. Sci. Instrum., **11**, 657–662 (1978).

[74] T.J. MOULSLEY, R.S. COLE, D.N. ASIMAKOPOULOS, S.J. CAUGHEY, *Simultaneous horizontal and vertical acoustic sounding of the atmospheric boundary layer*, Boundary-Layer Meteorol., **17**, 223–230 (1979).

[75] T.J. MOULSLEY, D.N. ASIMAKOPOULOS, R.S. COLE, B.A. CREASE, J. CAUGHEY, *Measurements of boundary layer structure parameter profiles by acoustic sounding and comparison with direct measurements*, Quart. J. R. Met. Soc., **107**, 203–230 (1981).

[76] T.J. MOULSLEY, D.N. ASIMAKOPOULOS, C.G. HECHIS, D.P. LALAS, J. GAYNOR, *A quantitative comparison of horizontal and vertical acoustic sounding with in-situ measurements*, Boundary-Layer Meteorol., **33**, 85–100 (1985).

[77] T.J. MOULSLEY, R.S. COLE, *A general radar equation for the bistatic acoustic sounder*, Boundary-Layer Meteorol., **19**, 359–372 (1980).

[78] P.T. MAY, K.P. MORAN, *The altitude coverage of temperature measurement using RASS with wind profiles radars*, Geophys. Res. Lett., **15**, 1381–1384 (1988).

[79] P.T. MAY, K.P. MORAN, R.G. STRAUCH, *The accuracy of RASS temperature measurements*, J. Appl. Meteorol., **28**, 1329–1339 (1989).

[80] L.G. MCALLISTER, *Acoustic sounding of the lower troposphere*, J. Atmos. Terr. Phys., **30**, 1439–1440 (1968).

[81] L.G. MCALLISTER, *Acoustic sounding — a new approach to the study of atmospheric structure*, Proc. IEEE, **57**, 579–587 (1969).

[82] G. MASTRANTONIO, G. FIUCCO, *Accuracy of wind velocity determinations with Doppler sodars*, J. Appl. Meteorol., **21**, 823–830 (1982).

[83] L.G. MCALLISTER, J.R. POLLARD, *Acoustic sounding of the lower atmosphere*, Proc. 6th International Symp. on Remote Sensing of the Environment, 436–450, 1969.

[84] M.E. MILLER, *Forecasting afternoon mixing depths and transport winds speeds*, Month. Weath. Rev., **95**, 35–44 (1967).

[85] W.D. NEFF, *Quantitative evaluation of acoustic echoes from the planetary boundary layer*, Prep. 16th Radar Meteorol. Conf. Montreal, 263–270, 1975.

[86] W.D. NEFF, C.W. KING, *Observations of complex-terrain flows using acoustic sounders: experiments, topography, and winds*, Boundary-Layer Meteorol., **40**, 363–392 (1987).

[87] W.D. NEFF, *Observations of complex-terrain flows usings acoustic sounders: echo interpretation*, Boundary-Layer Meteorol., **42**, 207–228 (1988).

[89] G.H. PETERS, H.T. TIHMERMAN, H. HINZPELER, *RASS, A remote sensing in the planetary boundary low-level temperature profiles*, Int. J. Remote. Sens., **4**, 49–63 (1983).

[90] P.D. PHILLIPS, H. RICHTER, W. NATER, *Layer model for assesing acoustic refraction effects in echo sounding*, J. Acoust. Soc. Am., **62**, 277–285 (1977).

[91] A. RAGHU, M. PURNACHANDRA RAO, J.S. HURTHY, *The effect of sea-breezes on atmospheric stability as observed with acoustic sounder*, Boundary-Layer Meteorol. **35**, 303–308 (1986).

[92] K.S. RAO, M.A. SCHAUB, *Observed variations of δ_θ and δ_Φ in the nocturnal drainage flow in a deep valley*, Boundary-Layer Meteorol. **51**, 31–48 (1990).

[93] K.T. SWANG, Z. GERSTMAN, *International turbulence comparison experiment* (I TCE-81), Boundary-Layer Meteorol., **31**, 325–348 (1985).

[94] J.H. RICHTER, *Clear air convection*, Geophys. Res. Lett., **1**, 173–176 (1974).

[95] S. ROSENBAUM, *Backscatter from gated fluctuating regions*, IEEE Trans. Antennas Propagat. **AP-20**, 618–624 (1972).

[96] P.B. RUSSEL, *Acoustic and direct measurement, of atmospheric mixing at three sites during an air pollution incident*, Atmos. Environ., **55**, 115–121 (1974).

[97] P.B. RUSSEL, E.E. UTHE, *A comparison of atmospheric structure as observed with monostatic acoustic sounder and lidar techniques*, J. Geophys. Res., **79**, 5555–5566 (1974).

[98] G. SAGER, *Eine Methods zur Vestimmung der Schallausbreitung in quasiruhender Atmosphere*, Z. Meteorol., **24**, 117–129 (1974).

[99] N.A. SHAW, *Observations of atmospheric structure using an acoustic sounder*, Rep. ANL (RER) 75-2, Arqonne Nat. Lab., 1974.

[100] S.P. SINGAL, S. KAGGARWAL, D.P. PAHWA, B.S. GERA, *Stability studies with the help of acoustic sounding*, Atmos. Envir., **19**, 221–228 (1985).

[101] A.S. SMEDHAN, *Observation of a multi-level turbulence structure in a very stable atmospheric boundary layer*, Boundary-Layer Meteorol., **44**, 231–253 (1988).

[102] D.H. WOOD, *Refraction convection in constant gradient media*, J. Acoust. Soc. Am., **47**, 1448–1452 (1970).

[103] L.C. SUTHERLAND, *Review of experimental data in support if a proposed new method for computing atmospheric losses*, National Technical Information Service, New York, 1975.

[104] V.I. TATARSKI, *Wave propagation in a turbulent medium*, Mc Graw-Hill, New York, 1969.

[105] I. TOMBACH, M. CHAN, *Use of a monostatic acoustic sounder in air pollution diffusion estimates*, Proc. 2nd Joint Conf. Sens. Env. Poll. Washington, 1973.

[106] R.H. TUILLIER, *Real-time analysis of local wind patterns for application to under-emergency response*, Bull. Amer. Meteorol. Soc., **68**, 1111–1115 (1987).

[107] E.E. UTHE, P.B. RUSSEL, *Experimental study of the urban aerosol structure and its relation to urban climate modification*, Bull. Amer. Meteorol. Soc., **55**, 115–121 (1974).

[108] A. WEILL, F. BAUDIN, J.G. GOUTORBE, P. van GRUNDERBEECK, P. LEBERRE, *Turbulence structure in temperature inversion and in convection fields as observed by Doppler sodar*, Boundary-Layer Meteorol., **15**, 375–390 (1978).

[109] A. WEILL, G. KLAPISZ, B. STRAUSS, F. BAUDIN, C. JAUPART, P. van GRUNDERBEECK, J.P. GOUTORBE, *Measuring heat flux structure functions of temperature fluctuations with an acoustic Doppler sodar*, J. Appl. Meteorol., **19**, 199–205 (1980).

[110] A. WEILL, F. BAUDIN, C. MAZADIER, G. DESBRAUX, C. KLAPISZ, A.G.M. DRIEDONSKS, J.P. GOUTORBE, A. PRUILHET, P. DURAND, *A mezoscale shear convective cell observed during the C.O.A.S.T. experiment: Acoustic sounder measurements*, Boundary-Layer Meteorol., **44**, 359–371 (1988).

[111] A. WEILL, O. TACONET, *Vertical velocity field in the convective boundary layer as observed with an acoustic Doppler sodar*, Boundary-Layer Meteorol., **23**, 133–151 (1982).

[112] M.L. WESELY, *The combined effect of temperature and humidity fluctuations on refractive index*, J. Appl. Meteorol., **15**, 43–49 (1976).

[113] A. WEILL et al., *A study of temperature fluctuations in the atmospheric boundary layer*, Boundary-Layer Meteorol., **10**, 337–346 (1976).

[114] J.C. WYNGAARD, *Behaviour of the refractive index structure parameter near the ground*, J. Opt. Soc. Am., **61**, 1646–1650 (1971).

[115] J.C. WYNGAARD, *Scalar fluxes in the planetary boundary layer-theory, modeling, and measurements*, Boundary-Layer Meteorol., **50**, 49–77 (1990).

[116] M.Y. ZHOU, NAT-PING LU, YAN-JUAN CHEN, *The detection of the temperature structure coefficient of the atmospheric boundary layer by acoustic radar*, J. Acoust. Soc. Am., **68**, 1, 303–308 (1980).

[117] M.Y. ZHOU, D.H. LENSCHOW, B.B. STANKOV, J.C. KAIMAL, J.E. GAYNOR, *Wave and turbulence structure in a shallow baroclinic convective boundary layer and overlaying inversion*, J. Atmos. Sci., **42**, 47–57 (1985).

[118] W.E. ZUIEV, N.P. KRASNENKO, W.A. FEDOROV, M.G. FORSOV, *Acoustical sounding of the boundary layer of the atmosphere*, [in Russ.], Dok. ANSSSR, 257, 1092–1096 (1981).

Received on February 3, 1992

ARCHIVES OF ACOUSTICS
17, 4, 511–523 (1992)

ULTRASONIC TRANSDUCERS RADIATING INTO THE AIR IN THE FREQUENCY RANGE 50–250 KHZ

W. PAJEWSKI and M. SZALEWSKI

Institute of Fundamental Technological Research
Polish Academy of Sciences
(00-049 Warszawa, Świętokrzyska 21)

In the paper ultrasonic piezoelectric transducers radiating into the air in the frequency range 50–250 kHz are described. Methods of improving their properties (efficiency, frequency characteristics, directivity characteristics) are discussed. Several types of designed, made and investigated transducers are presented. The transducers have the form of properly shaped piezoelectric plates or an array of plates embedded in plastic. The properties of these transducers enable their application in robotics, e.g., in echolocation or in object identification systems.

1. Introduction

Ultrasonic transducers are applied in robotics in echolocation systems — detection and localization of obstacles on the path of a mobile robot [1, 2], in object identification systems — object localization, identification and classification [4, 7], e.g., in automated production lines and for robot grip position measurements [8, 11]. In such systems transducers radiate ultrasonic energy into the air. The ultrasonic signal range and the electric power necessary for transducer excitation depend on the efficiency of ultrasonic energy transmission into the air. Ultrasonic systems applied in robotics should not require large supply powers, especially in the case of sensors on a mobile robot.

Ultrasonic transducers applied in robotics should also have suitable radiation directivity characteristics and a frequency bandwidth. Directivity pattern widths of transducers applied in echolocation and object identification have a crucial influence on the resolution of systems. Strong acoustic beam side lobes generate parasite signals from surrounding objects. The frequency bandwidth should be wide because these transducers work in the pulse mode. Wide bandwidth of transducers is especially important in object identification systems because the information about the object is contained in the shape of the pulse reflected from this object [4].

Strong mismatching of acoustic impedances impedes considerably the radiation of ultrasonic piezoelectric transducers into the air. The characteristic acoustic impedance of the air is 5 times smaller than acoustic impedances of piezoelectric ceramics and crystals. Owing to this strong mismatching, the acoustic transmission coefficient on the transducer — air boundary is very small (10^{-4}–10^{-5}) and the transducer works in the narrow frequency bandwidth.

Modern technology requires sensor and robots to work with high accuracy and quality respectively. Such devices use suitable instrumentation to obtain objective data and to provide inputs to automatic control systems. These requirements help to speed up the development of microelectronics and ultrasonic technology. This is backed by extensive research on the subject of ultrasonic transducers for the use of on–robots and on–automatic control systems. The purpose of the present paper is to study the radiation property of types of piezoelectric transducers having the form of a piezoelectric plate or an array of plates embedded in plastic, the plates being made of a piezoelectric ceramic. Since such transducers are of rather low cost, it is reasonable to ask: given some knowledge of required accuracy and quality of ultrasonic transducers for the use of on–robots and on–automatic control systems, is it possible to make ceramic plate transducers applicable to these devices? The remainder of this paper is concerned with finding particular answers to this question.

Different methods of impedances mismatching reduction are discussed in Sect. 2. Examples of piezoelectric ultrasonic transducers radiating into the air are presented in Sect. 3. Their properties are summarized in Table 1.

Table 1. Properties of different types of ultrasonic piezoelectric transducers radiating into the air

Nr	f [kHz]	Pressure of acoustic wave generated by the transducer – distance 30 cm [Pa]	Sensitivity for the transducer working as a receiver [μV/Pa]	Beam spread 3 dB [°]	Beam spread 6 dB [°]	Side lobes [dB]	Remarks
5	191	68	50	6	8	−8	mosaic, star-shaped
8	190.5	310	230	3	4	−8	ring, patented
9	190	350	260	3	4	−8 −14	ring, patented
13	153.5	216	160	6	8	—	radial vibrations
15	96.5	270	200	14	16	—	thickness vibrations, $\lambda/4$ plate, patented
17	105.5	270	240	12	14	−20	thickness vibrations, $\lambda/2$ plate
18	190.5	756	560	3	4	−9	3 rings, patented
19	113.5	365	270	8	10	−6 −14	3 plates, thickness vibrations
22	105	297	220	8	10	−12	3 plates, thickness vibrations

2. Improvement of properties of piezoelectric ultrasonic transducers radiating into the air

As we have mentioned in the Introduction strong mismatching of acoustic impedances is the main problem which exists as regards radiation of piezoelectric transducers into the air. Transducers are usually made of piezoelectric ceramic — type PZT. Impedance mismatching is smaller for piezoelectric foils PVDF, their impedance is one order of magnitude smaller than the acoustic impedance of piezoelectric ceramic. Unfortunately, piezoelectric foils have an electromechanical coupling coefficient much smaller and dielectric losses higher than piezoelectric ceramic. Furthermore their low dielectric constant

makes difficult their electric matching to transmitting and receiving electronic circuits. Mechanical quality factor of piezoelectric ceramic ($Q_m \geq 50$) impedes its application for work in the wide frequency bandwidth.

The application of one or more quarter-wavelength impedance transformers is the standard method of matching an ultrasonic transducer to a load. This method is successfully applied when a transducer radiates into a solid or liquid. The application of quarter-wavelength transformers to piezoelectric transducers radiating into the air (or other gases) is difficult owing to the lack of materials with properly low acoustic impedances [10]. A matching layer made of silicone rubber filled with hollow glass spheres was the best solution described in the literature. The glass spheres had an average diameter of 80 μm and wall thickness of 2 μm. This composite applied as a quarter-wavelength transformer enabled to reduce considerably losses in comparison with the same transducer without the matching layer [17].

The other method of reducing impedance mismatching and of increasing ultrasonic energy transmission into the air is to apply composite transducers: piezoelectric ceramic-plastic material [16]. Such a composite is a two-phase material in which the ceramic produces the piezoelectric effect while the plastic reduces density and increases elastic compliance. The acoustic impedance of composites is several times smaller than the acoustic impedance of piezoelectric ceramic. Transducers made of composites have Q_m = 5 – 15 and a wide frequency bandwidth.

The shape of a transducer radiation directivity characteristic (beam width proper to the application, side lobes reduction) is very important from the practical point of view. The radiation directivity pattern depends on the vibration distribution on the transducer surface [13]. One obtains the directivity pattern without side lobes when the vibration distribution is described by the Gauss function. When vibration distribution approximates the Bessel function J_0, the radiated beam has a very small divergence. One can form the directivity pattern by selecting a proper type and mode of vibrations [13], the dimension and shape of the transducer, and by applying nonuniform polarization of piezoelectric ceramic [5] or electrode apodization [9]. It is also possible to use an array of several transmitting transducers [12] or a properly driven segmented transducer [3].

The realization of efficient quarter-wavelength transformers as well as composite transducers requires special materials and complicated technologies. In Sect. 3 we shall describe several ultrasonic transducers designed and made by us. They have the form of properly shaped piezoelectric plates or of a proper array of piezoelectric plates embedded in plastic. It is not possible to obtain complete impedance matching this way but acoustic energy radiation efficiency is sufficient for the applications of robotics. Such transducers have simple technology; their mechanical quality factor Q_m is reduced and one can form properly their directivity patterns. The theoretical analysis of vibrations of piezoelectric plates such as plates applied in these transducers has been presented earlier elsewhere [6, 13, 14].

3. Examples of piezoelectric ultrasonic transducers radiating into the air

3.1. Transducers with thickness vibrations of piezoelectric plates

Piezoelectric plates excited to thickness vibrations have a complicated deformation structure depending on the ratio of the plate diameter D to the plate thickness d. Differ-

ent modes of vibration exist [13]. The radiation directivity characteristics of these plates differ considerably from the simple case of piston vibrations. There are vibration distributions, especially for the small ratio D/d, which have better directivity patterns than the piston transducers. These vibration distributions are characterized by a small amplitude of vibrations on the transducer edges, by the lack of distinct vibrations nodes on the transducer surface and by insignificant phase difference on the vibrating surface [13]. The electromechanical coupling coefficient is large for thickness vibrations; this makes it possible to use smaller supply voltage.

Three types of transducers with thickness vibrations of piezoelectric plates embedded in polyurethane resin have been made. The resin improves matching of acoustic

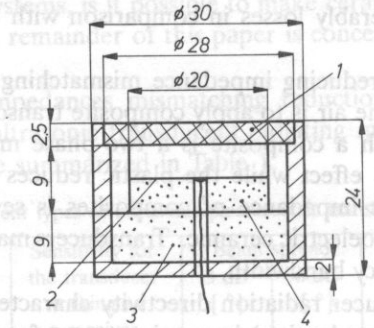

FIG. 1. Transducer with piezoelectric plate vibrating in the thickness direction. *1* — polyurethane resin, *2* — piezoelectric ceramic plate, *3* — epoxy resin with tungsten powder, *4* — passive ceramic with high ρc.

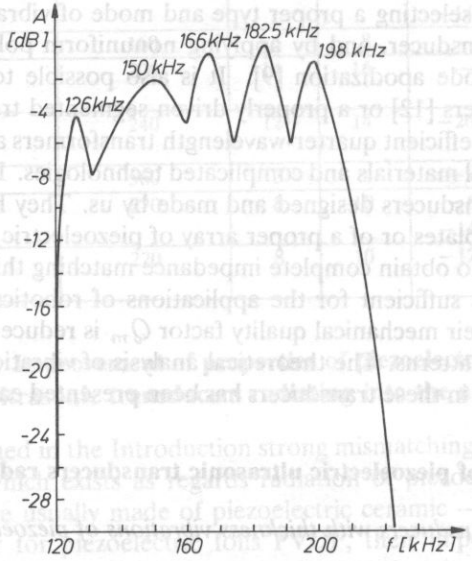

FIG. 2. Frequency characteristic of the transducer shown in Fig. 1. Arbitrary units.

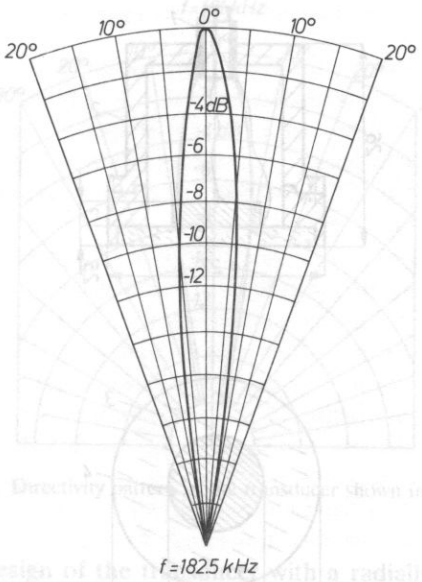

FIG. 3. Directivity pattern of the transducer shown in Fig. 1.

impedances and decreases the mechanical quality factor. In the first type of transducers a piezoelectric ceramic (type PZT) plate with thickness $\lambda/2$ was applied. In the second type — a piezoelectric plate with thickness $\lambda/4$ was placed on the base with high acoustic impedance — Fig. 1. The reduction of the plate thickness makes it possible to decrease an exciting voltage. The frequency characteristic of such a transducer is presented in Fig. 2 the directivity pattern recorded under quasi-continuous conditions — in Fig. 3. The lack of side lobes in the directivity pattern is worth noticing. Further reduction of an exciting voltage was possible using a pile of thin plates of piezoelectric ceramic connected electrically in parallel. By applying such a transducer as a transmitter and transducer with a pile of plates connected electrically in series as a receiver, one can considerably increase the radiation range.

3.2. Transducer with radial vibrations of piezoelectric plate

A piezoelectric plate excited to radial vibrations may radiate a wave in a direction perpendicular to its surface. This is possible because deformation in the radial direction causes also a change of the plate thickness. Coupling between radial and axial deformations depends on the Poisson constant of the piezoelectric material. The greatest amplitude of vibration in the direction perpendicular to the surface occurs at the centre of the plate, vibrations vanish in the direction of the plate edges. For the mode (0, 1) of radial vibrations of circular plates, one obtains the amplitude distribution of vibrations near the Gauss function. The near field is reduced and the side lobes of the directivity pattern are strongly damped [14]. It is also possible to excite higher modes of vibrations but then electromechanical coupling is lower.

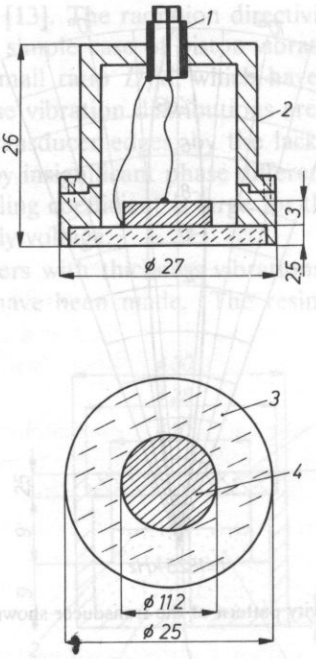

FIG. 4. Transducer with radially vibrating piezoelectric plate. *1* — BNC junction, *2* — casing, *3* — polyurethane resin, *4* — piezoelectric ceramic.

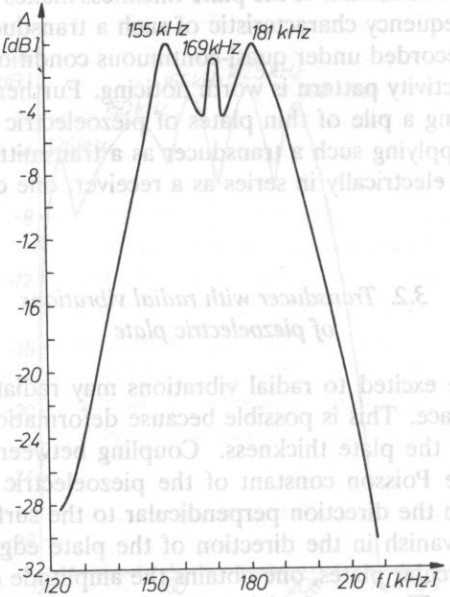

FIG. 5. Frequency characteristic of the transducer shown in Fig. 4. Arbitrary units.

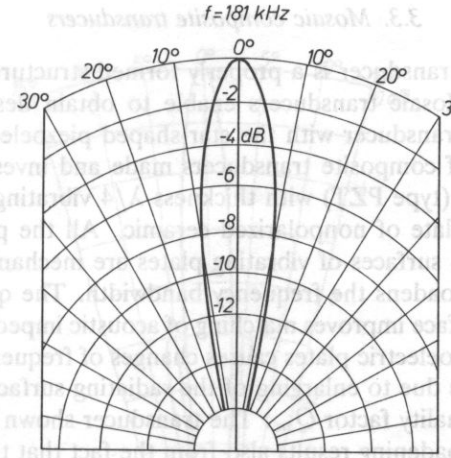

FIG. 6. Directivity pattern of the transducer shown in Fig. 4.

Figure 4 shows the design of the transducer with a radially vibrating plate of piezoelectric ceramic, Fig. 5 — its frequency characteristic, Fig. 6 — its directivity pattern. One can see that the radiation directivity pattern without side lobes has been obtained. Polyurethane resin improved matching of acoustic impedances and reduced the mechanical quality factor.

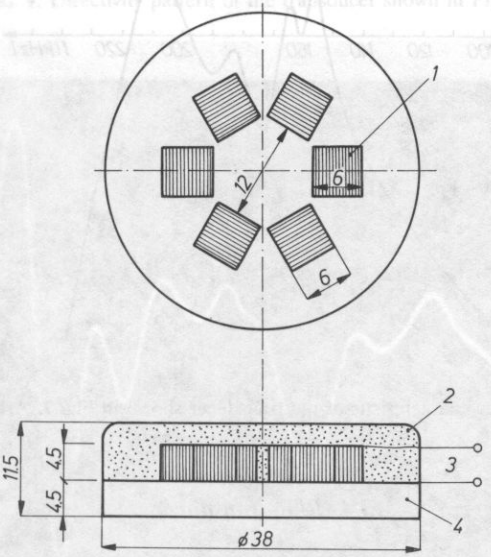

FIG. 7. Composite mosaic transducer with star-shaped arrangement of piezoelectric plates, *1* — piezoelectric ceramic, *2* — polyurethane resin, *3* — electrodes, *4* — passive ceramic.

3.3. *Mosaic composite transducers*

A mosaic composite transducer is a properly formed structure of piezoelectric plates embedded in plastic. Mosaic transducers enable to obtain desired radiation directivity characteristics. The transducer with the star-shaped piezoelectric plate arrangement (Fig. 7) is an example of composite transducers made and investigated by the authors. The piezoceramic plates (type PZT) with thickness $\lambda/4$ vibrating in the thickness direction are placed on the plate of nonpolarized ceramic. All the plates are submerged in polyurethane resin. Back surfaces of vibrating plates are mechanically loaded by passive ceramic. This loading broadens the frequency bandwidth. The quarter-wavelength resin layer on the radiating surface improves matching of acoustic impedances. The plastic mass vibrating jointly with piezoelectric plates causes changes of frequency and directivity characteristics (Figs. 8 and 9) due to enlarging of the radiating surface and decreasing of the transducer mechanical quality factor Q_m. The transducer shown in Fig. 7 has $Q_m = 12$. Frequency bandwidth broadening results also from the fact that this transducer can work at a lower frequency when piezoelectric plates are excited to contour vibrations. This transducer is especially useful for pulse work owing to its broad frequency bandwidth. The pulse response of the star-shaped transducer has been investigated in the shock tube — Fig. 10. Damped oscillations for time greater than 20 μs were caused by spurious oscillations of the tube itself. The other realized composite mosaic transducers were described in [15].

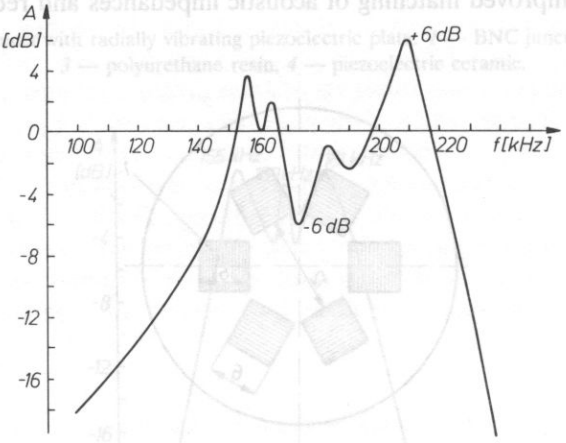

FIG. 8. Frequency characteristic of the transducer shown in Fig. 7. Arbitrary units.

3.4. *Ring transducer*

A ring transducer consists of one or some rings of piezoelectric ceramic embedded in polyurethane resin. Designs, theoretical analysis and characteristics of ring transducers are described in [6].

The resonance vibrations of ring and plastic mass appear in a ring transducer filled by a plastic material. By selecting properly ring dimensions, one can obtain coupling between

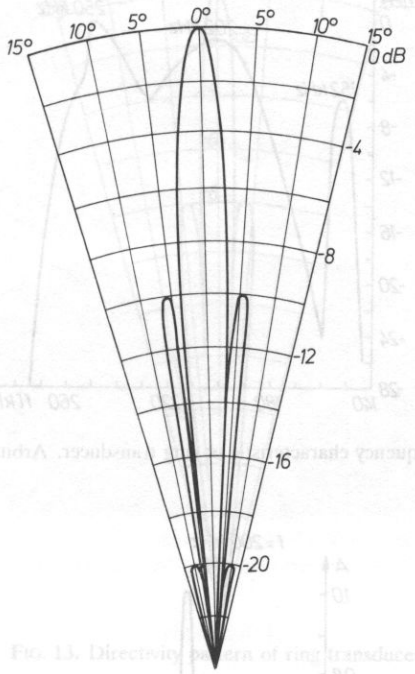

FIG. 9. Directivity pattern of the transducer shown in Fig. 7.

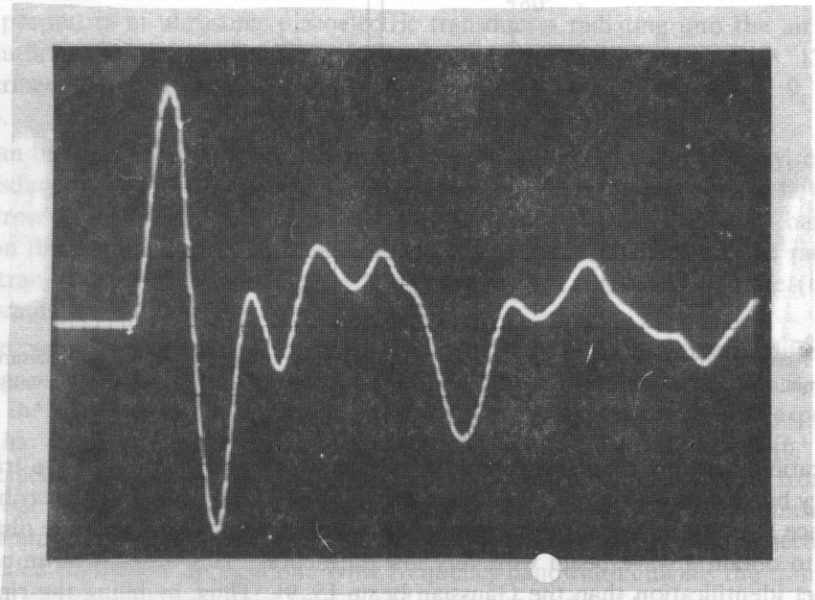

FIG. 10. Pulse response of the transducer shown in Fig. 7 measured in shock tube, 5 μms/div.

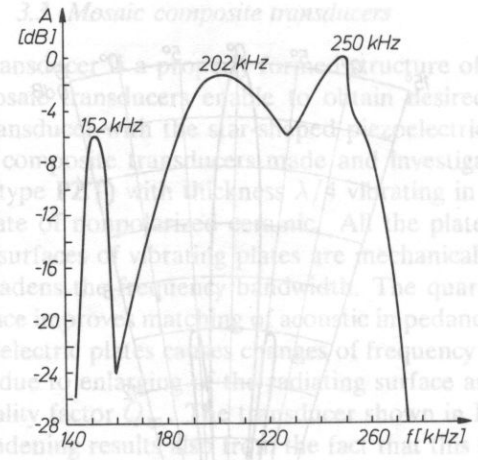

FIG. 11. Frequency characteristic of ring transducer. Arbitrary units.

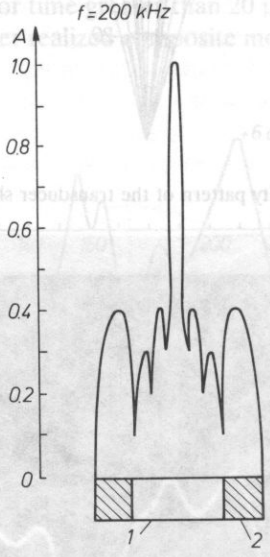

FIG. 12. Acoustic pressure in the air, distance 10 mm from the surface of ring transducer, measured using miniature microphone, *1* — polyurethane resin, *2* — piezoelectric ceramic. Arbitrary units.

ring vibrations and plastic mass vibrations. This produces broadening of the transducer frequency bandwidth — Fig. 11. Plastic mass vibrations have an amplitude distribution on the surface like the zero order Bessel function — Fig. 12. Such an amplitude distribution permits to obtain a wave beam with very low diffraction. This beam is more useful for the object identification than the Gaussian beam [5, 9]. Thus, by filling the ring with a plastic, one obtains better matching to the air, a wider frequency bandwidth and a wave beam with very small divergence — Fig. 13.

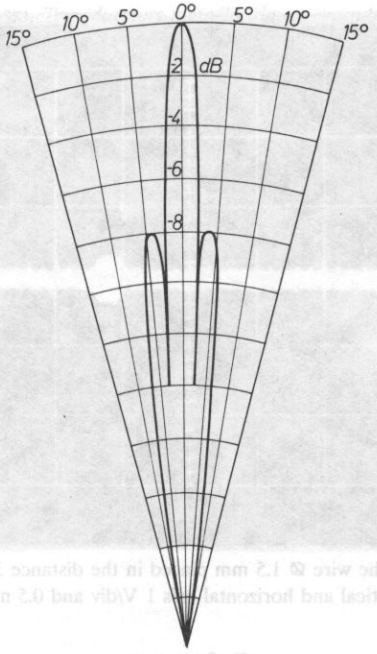

FIG. 13. Directivity pattern of ring transducer.

4. Conclusion

The properties of ultrasonic piezoelectric transducers radiating into the air realized by the authors are compiled in Table 1. Designs of the transducers nos. 15, 17, 19, 22 are described in Sect. 3.1, nr 13 — in Sect. 3.2, nr 5 — in Sect. 3.3, nos. 8, 9, 18 — in Sect. 3.4.

As can be seen in Table 1, the ring transducers have the highest efficiency, especially the transducer with three piezoelectric rings (nr 18). The ring transducers have also a very narrow main lobe of radiation directivity pattern and wide frequency bandwidth. Radiation directivity patterns without side lobes have been obtained for the radially vibrating transducer (nr 13) and for the transducer with a piezoelectric plate (thickness $\lambda/4$) vibrating in the thickness direction (nr 15).

These transducers have been successfully applied for the localization of different objects. Figure 14 shows pulses reflected from a wire with the diameter 1.5 mm, distance between the wire and the ring transducer 30 cm, f = 200 kHz. Conducted experiments proved that the realized transducers are proper for applications in robotics [6, 15]. Radiation efficiency, especially for ring transducers, ensures a suitable range (from above 1 m for one transducer working as transmitter — receiver at 200 kHz to several meters for two transducers at 100 kHz). It is possible to shape directivity patterns according to the provided transducer application. Wide frequency bandwidth enables the transmission of narrow pulses (with sinusoidal carrier and short rise and fall time) without significant distortions.

Two types of transducers are patented.

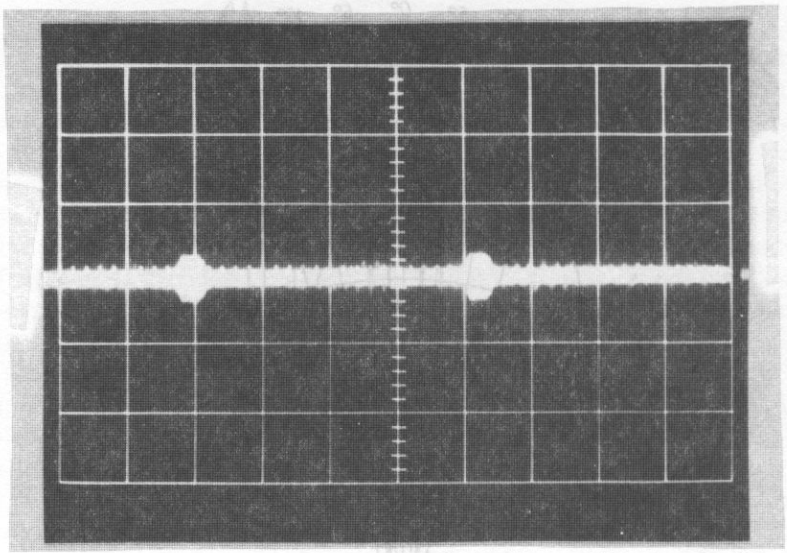

FIG. 14. Pulses reflected from the wire Ø 1.5 mm placed in the distance 30 cm from the ring transducer, f = 200 kHz. Vertical and horizontal axis 1 V/div and 0.5 ms/div, respectively.

References

[1] G. BAUZIL, M. BRIOT, P. RIBES, *A navigation sub-system using ultrasonic sensors for the mobile robot*, Proc. of the 1st Intern. Conf. on Robotics and Automation. 47–58 (1981).

[2] J. BORENSTEIN, Y. KOREN, *The vector field histogram — fast obstacle avoidance for mobile robots*, IEEE Trans. Robot. Automat., 7, 3, 278–288 (1991).

[3] C.B. BURCKHARDT, P.A. GRANDCHAMP, H. HOFFMANN, *Focussing ultrasound over a large depth with an annular transducer — an alternative method*, IEEE Trans. SU-22, 1, 11–15 (1975).

[4] H. ERMERT, J. SCHMOLKE, G. WETH, *An adaptive ultrasonic sensor for object identification*, 1986 IEEE Ultrason. Symp. Proc.

[5] D.K. HSU, F.J. MORGETAN, M.D. HASSELBUSSCH, S.J. WORMLEY, M.S. HUGHES, P.O. THOMPSON, *Ultrasonic beams with Bessel and Gaussian profiles*, Rev. of Progress in Quantit. Nondestr. Eval., vol. 9, Plenum Press, New York 1990, 799–806.

[6] P. KIEŁCZYŃSKI, W. PAJEWSKI, M. SZALEWSKI, *Ring piezoelectric transducers radiating ultrasonic energy into the air*, IEEE Trans. UFFC-37, 1, 38–43 (1990).

[7] A.C. KNOLL, *Ultrasonic holography techniques for localizing and imaging solid objects*, IEEE Trans. Robot. Automat., 7, 4, 449–467 (1991).

[8] Š. KŐCIŠ, *Electroacoustical robot grip position measurement*, Computers and Artificial Intelligence, **2**, 5, 479–488 (1983).

[9] J.Y. LU, J.F. GREENLEAF, *Ultrasonic nondiffracting transducer for medical imaging*, IEEE Trans. **UFFC-37**, 5, 438–447 (1990).

[10] L.C. LYNNWORTH, *Ultrasonic impedance matching from solids to gases*, IEEE Trans. **SU-12**, 2, 37–48 (1965).

[11] J.M. MARTIN, R. CERES, J. NO, L. CALDERON, *Adaptive ultrasonic range-finder for robotics, Sensor devices and systems for robotics*, [Ed.] A. Casals, Springer Verlag, Berlin 1989, 143–156.

[12] H. MURATA, M. HASHIMOTO, M. UCHIDA, *The development of an ultrasonic measuring system for the tracking of a moving target*, JSME Intern. J., **30**, 259, 130–140 (1987).

[13] W. PAJEWSKI, *Vibrations and radiation of piezoelectric ceramic transducers* [in Polish], Archiwum Akustyki, **4**, 2, 355–367 (1967).

[14] W. PAJEWSKI, *On the possibility of using the radial vibrations of piezoelectric plates to generate ultrasonic radiation in liquids*, Proc. of Vibration Problems, **14**, 4, 367–372 (1973).

[15] W. PAJEWSKI, M. SZALEWSKI, *Transducteurs piézoélectriques engendrant des ondes ultrasonores dans l'air (200 kHz)*, Colloque sur les Ultrasons et Acoustique Physique, Paris 1987, 222–239.

[16] W. WERSING, *Composite piezoelectrics for ultrasonic transducers*, Proc. 1986 IEEE Int. Symp. on Applications of Ferroelectrics, 249–260.

[17] T. YANO, M. TONE, A. FUKUMOTO, *Range finding and surface characterization using high-frequency air transducers*, IEEE Trans. **UFFC-34**, 2, 232–236 (1987).

Received on April 17, 1991

ARCHIVES OF ACOUSTICS
17, 4, 525–542 (1992)

THE ENERGY DISTRIBUTION IN THE FAR FIELD RADIATED FROM THE SEMI-INFINITE UNFLANGED CYLINDRICAL WAVE-GUIDE

A. SNAKOWSKA

Department of Theoretical Physics
Pedagogical University of Rzeszów
(35-310 Rzeszów, ul. Rejtana 16)

The theory of an arbitrary axi-symmetric Bessel mode in a circular wave-guide is reviewed and applied to the analysis of the energy distribution in the far field outside the duct. The duct is assumed to be semi-infinite and perfectly rigid, and the diffraction phenomena occurring at the open end are taken into account.

The intensity directivity function as well as the power–gain function for every mode appearing in the duct, with the diffraction parameter ka changing within the limits 0–15, has been discussed.

The formulae for the intensity directivity function were derived by applying the saddle point method to the exact expression for the acoustic velocity potential. The first and second approximations are developed and the results of computed numerical characteristics are discussed.

List of symbols

a	wave-guide radius
A_l	amplitude of l–mode
c_0	speed of sound at an ambient condition
$d_l(\vartheta)$	directivity function in the first approximation
$D_l(R, \vartheta)$	directivity function in the second approximation
$f_l(z)$	jump of potential at the wave-guide surface
$F_l(w)$	Fourier transform of $f_l(z)$
$G_l(\alpha, \vartheta)$	integrand in Eq. (6)
$I(\,)$	intensity of radiation
$H_n^{(1)}(\,)$	n order Hankel function of the first kind
$J_n(\,)$	n order Bessel function
k	wave number
ka	diffraction parameter
$K_l^{(I)}(\,)$	power directivity function defined by Wajnshtejn
l, n	Bessel mode numbers
N	index of Bessel mode producing cut-off at a fixed diffraction parameter
$p(\,)$	acoustic pressure
P_0	power radiated by a spherical wave
$P_l^{(\mathrm{inc})}$	power propagated with the l incident mode
$P_l^{(\mathrm{rad})}$	power radiated outside

R_{ln}	complex reflection coefficient
r_{ln}	power reflection coefficient
r_l	total reflection coefficient
$s^{(p)}(\,)$	pressure directivity function
$S^{(p)}(\,)$	pressure directivity function defined by Morfey
$s^{(I)}(\,)$	relative power directivity function
$S^{(I)}(\,)$	intensity directivity function defined by Eq. (18)
v	radial wave number
v_R	radial velocity
w	partial wave number
$W_l(\vartheta)$	second order contribution to directivity factor
$\Phi_l^{\mathrm{inc}}(\,)$	velocity potential of incident l mode
$\Phi_l(\,)$	velocity potential of l mode
γ_l	partial wave number of l Bessel mode
μ_l	l root of J_1
ζ_0	specific impedance of the environment
ρ_0	medium density
$\mathcal{G}(\,)$	power–gain function
$*$	complex conjugate

Other symbols used in the text are standard ones and are not listed here.

1. Introduction

Ducts, pipes and tubes in which sound propagates are called wave-guides for the reason that they carry the acoustic energy so efficiently that it does not decay according to the inverse square-distance law. These phenomena have been known for a long time, at least as long ago as when man made use of his hands as a horn to be heard at a long distance.

Some experiments showing the propagation of energy in tubes were described a hundred years ago by J. TYNDALL [1]. The observations were carried out by the famous physicist, Biot, who noticed that the lowest whispear had been heard at the other end of a 950–meter–long water pipe and that the firing of a pistol had put out the candle at the outlet.

The efficiency of transmitting sound by pipes causes sometimes an undesirable noise outside the outlet, even far away from it. The necessity often arises to damp this unwanted noise for ecological, human–health, technological or other reasons. In everyday life these problems appear in connection with road traffic and aircraft transportation, the last being the most harmful nowadays. This is why there has been so much additional interest.

For this reason too, the investigations of the distribution of acoustic energy, radiated out of the duct into the free space, is of great importance, not only theoretical but also practical.

The problem of sound propagating in the circular duct and radiating outside has been considered in a few different aspects:

– the phenomena occurring at the open end — impedance of the outlet, reflection coefficients, appearance of higher order modes in the reflected wave (WAJNSHTEJN [2]), ERIKKSON [3], LEVINE and SCHWINGER [4], SNAKOWSKA and WYRZYKOWSKI [5, 6]),

– ther acoustical properties of circular ducts with some additional geometry features like nonuniform area, certain wall thickness, finite length (ALFREDSON [7], LUNDQVIST and BOSTROM [8], HUDDE [9], ANDO [10], JOHNSTON and OGIMOTO [11, 12],

– the propagation of sound in ducts with flow (JOHNSTON and OGIMOTO [11, 12], CARIER [13], MORFEY [14], LANSING et al. [15]),

– the attenuation of sound in a duct with impedance-type boundary conditions (RAWLINS [16, 17], TESTER [18]).

In the present paper we develop the intensity directivity characteristics for any axis-symmetric Bessel mode which propagates to the open and where it is partly reflected and partly radiated outside. We consider the far field taking into account all the diffraction phenomena at the outlet. The method involved is the saddle point method called also the steepest descent method.

It is undoubtful whether the energy relations in the acoustic wave radiating outside are of great interest. Some authors working on the problem restrict their investigations to the plane wave, maintaining the opinion that the latter represents the behaviour of the system well enough. It is true as long as the diffraction parameter fulfills the condition $ka < 3.83$ (the value of the first root of the Bessel function J_1) when only the plane wave can propagate along the duct without damping. Otherwise the principal mode approximation can lead to important errors, as will be demonstrated in this paper.

In Section 2 the outline of the saddle point method is presented as well as the first and second approximation formulas for the acoustical potential. In Section 3 the intensity directivity function and the power–gain function are introduced, while Section 4 contains the results of numerical calculations and conclusions.

2. Formulation of the problem. The saddle point method approximation

Let us consider the rigid semi-infinite cylindrical wave-guide of radius "a" stretching from $z = 0$ to ∞, with the z-axis being its axis of symmetry Fig. 1.

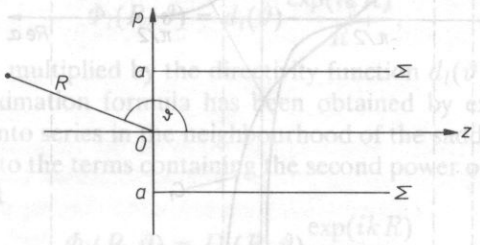

FIG. 1. Geometry of the problem.

We will only consider the axi-symmetric excitations whose time dependence is expressed by the factor $\exp(-i\omega t)$, ω being the determined frequency of vibrations. We assume that the single Bessel mode of a potential [19]

$$\Phi_l^{\text{inc}}(\rho, z) = A_l \frac{J_0(\mu_l \rho/a)}{J_0(\mu_l)} \exp(-i\gamma_l z), \tag{1}$$

where γ_l is the partial wave number related to the wave number k by the following relationship $\gamma_l = \sqrt{k^2 - \mu_l^2/a^2}$, μ_l is the l root of the Bessel function $J_1(\,)$, is incident. The wave equation solution which satisfies the hard wall boundary conditions (i.e., the

decay of the radial vibration velocity on the wave-guide wall [19]) has the form [2, 5]

$$\Phi_l(\rho, z) = \frac{ai}{4} \int_{-\infty}^{+\infty} dw \exp(iwz) v F_l(w) \begin{Bmatrix} H_0^{(1)}(v\rho) & J_1(va) \\ H_1^{(1)}(va) & J_0(v\rho) \end{Bmatrix}_{\rho<a}^{\rho>a} + \Phi_l^{\text{inc}}(\rho, z), \tag{2}$$

where w, v are partial and radial wave numbers, respectively, and $w^2 + v^2 = k^2$, $F_l(w)$ is the Fourier transform of the jump of the potential

$$f_l(z) = \Phi_l(\rho, z)|_{\rho \to a+} - \Phi_l(\rho, z)|_{\rho \to a-}. \tag{3}$$

Detailed considerations are reported in [2, 5].

The next step is to apply the saddle point method to the expression (2). The method was analysed step by step in our previous paper [20], so only an outline will be presented here.

The expression for the potential (2) is different in two partts of space $\rho > a$ and $\rho < a$, as the potential must fulfill Sommerfeld's radiation and finiteness conditions. The saddle point method must be applied to the upper and lower form of expression (2) separately.

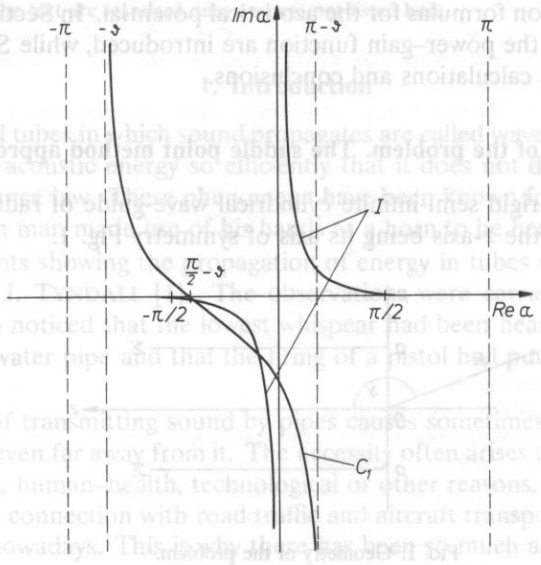

FIG. 2. Contour of integration C_1 in α complex plane.
I — cut lines of the two value function beginning at the branch points.

The saddle point method is a well known approximate method of calculating the contour integrals of the type

$$\Gamma(\Lambda) = \int G(z) \exp(\Lambda g(z))\, dz, \tag{4}$$

where $G(z)$ and $g(z)$ are analytic functions, Λ being the real parameter. To make this method applicable to our problem, we have to assume that the wave number k has a small imaginary part. This assumption allows us to consider the integrand in Eq. (2) as an analytic function and to adjust its form to the formula (3) that is, first of all, to eliminate

the exponential function. For that reason we introduce the new complex variable α as follows:

$$w = k \sin \alpha, \tag{5}$$

and apply the asymptotic form of the Hankel function $H_0^{(1)}(v\rho)$ or $J_0(v\rho)$ [21], depending on what part of space we are considering. For further calculations it will be convenient to introduce the polar coordinates (R, ϑ) so that $\rho = R \sin \vartheta$, $z = R \cos \vartheta$. After these steps we obtain the potential in the form

$$\Phi_l(R, \vartheta) = c \exp\left(\frac{i\pi}{4}\right) \int_{C_1} G_l(\alpha, \vartheta) \exp(ikR \sin(\alpha + \vartheta)) \sqrt{\cos \alpha}\, d\alpha, \tag{6}$$

the contour C_1 being plotted in Fig. 2. The explicit form of the constant c and $G_l(\alpha, \vartheta)$ for $\rho > a$ and $\rho < a$ were presented in [20]. The form of the above expression makes it possible to deduce the next step, i.e., to choose such a contour of integration which passes through the saddle point and on which the exponential function diminishes the fastest. For who has some experience in applying this method the substitution of the form

$$\sin(\alpha + \vartheta) = 1 + ix^2, \tag{7}$$

is obvious, as the exponential function in Eq. (6) takes the form $\exp(ikR) \exp(-kRx^2)$ the second term representing the function decaying exponentially with x^2. For $|kR| \gg 1$ and real k the major contribution to the integral comes from the neighbourhood of $x = 0$, which corresponds to $\alpha_0 = \pi/2 - \vartheta$.

In both parts of space $\rho > a$ and $\rho > a$ we finally obtain the same expression for the velocity potential. In the first approximation the $G_l(\alpha, \vartheta)$ function has been replaced by its value at the saddle point.

According to [20] in the first approximation we obtain the formula

$$\Phi_l(R, \vartheta) = d_l(\vartheta) \frac{\exp(ikR)}{R}, \tag{8}$$

i.e., the spherical wave multiplied by the directivity function $d_l(\vartheta)$.

The second approximation formula has been obtained by expanding the integrand $G_l(\alpha, \vartheta)$ and $\sqrt{\cos \alpha}$ into series in the neighbourhood of the saddle point and by restricting our considerations to the terms containing the second power of variable x at the most. This leads to the result

$$\Phi_l(R, \vartheta) = D_l(R, \vartheta) \frac{\exp(ikR)}{R}, \tag{9}$$

where

$$D_l(R, \vartheta) = d_l(\vartheta) + \frac{ia}{2R} W_l(\vartheta), \tag{10}$$

so in the expression for the directivity function the term depending on the distance R appears. Its contribution to the field potential decreases with the distance R, but for some values of R neglecting this term would affect the results considerably, what will be shown in the next section. It is clear that we can obtain the first approximation in the limit $R \to \infty$, so it is also called the "infinite distance approximation". Because of the rather complicated form of expressions for the above introduced quantities $F_l(w)$, $d_l(\vartheta)$, $D_l(R, \vartheta)$, we do not present their explicit forms in this paper. Readers are referred to our previous paper [20] containing all the details.

We should not forget about the limits applicability of the presented method. For the real wave number k, the results obtained are valid for $kR\sin^2\vartheta \gg 1$, this condition occurring as a result of applying asymptotic formulas.

3. Evaluation of physical quantities. Power directivity and power–gain function

Among many physical quantities useful in analysing the problem of acoustic far field outside the pipe, the pressure directivity, the power directivity, and the power–gain functions should be listed.

The pressure directivity function can be defined as a ratio of the pressure in the given direction (ϑ, φ) and the pressure of an isotropically radiating point source of equal power output:

$$s^{(p)}(R, \vartheta, \varphi) = |\Phi(R, \vartheta, \varphi)|R. \tag{11}$$

JOHNSTON and OGIMOTO [12] define the pressure directivity as

$$S^{(p)}(R, \vartheta, \varphi) = \frac{|p(R, \vartheta, \varphi)|R}{\rho_0 c_0}, \tag{12}$$

so using the well-known dependence between the velocity potential and acoustic pressure it is easy to notice that

$$S^{(p)}(R, \vartheta, \varphi) = ks^{(p)}(R, \vartheta, \varphi). \tag{13}$$

For the potential given by the formulas (8) or (9) the pressure directivity function (11) is equal to $|d_l(\vartheta)|$ and $|D_l(\vartheta)|$, respectively, the index l referring to a number of Bessel mode propagating along the pipe and radiating outside. This quantity has been considered for the diffraction parameter ka changing within the limits of (0–15), so now we will concentrate on the quantities connected with energy distribution in the far field.

WAJNSHTEJN [2] defines the power directivity function as the power radiated into a unit solid angle in the direction connected with the velocity potential in the way

$$K^{(I)}(\vartheta, \varphi) = \frac{1}{2}\rho_0 c_0 k^2 |\Phi|^2 R^2. \tag{14}$$

It is easy to find out that the above is valid only in the infinite distance approximation $R \to \infty$. As $P_0 = 1/2\rho_0 c_0 k^2$ is the power radiated into a unit solid angle by a spherical wave of a potential $\Phi = (1/R)\exp(ikR)$, we can write the last expression in the form

$$K^{(I)}(R, \vartheta, \varphi) = P_0 |\Phi|^2 R^2, \tag{15}$$

and define the related power directivity function

$$s^{(I)}(R, \vartheta, \varphi) = \frac{K^{(I)}(R, \vartheta, \varphi)}{P_0} \tag{16}$$

According to that definition, in the case of axis symmetric excitation, we obtain in the first approximation as follows:

$$s_l^{(I)}(\vartheta) = |d_l(\vartheta)|^2. \tag{17}$$

MORFEY in his work [14] introduced the intensity directivity function, applied later by JOHNSTON and OGIMOTO [12]

$$S^{(I)}(R, \vartheta, \varphi) = \rho_0 c_0 I(R, \vartheta, \varphi) R^2, \tag{18}$$

where $I(R, \vartheta, \varphi)$ is the power radiated into the unit solid angle in the direction (ϑ, φ)

$$I(R, \vartheta, \varphi) = \langle p(R, \vartheta, \varphi) v_R^*(R, \vartheta, \varphi) \rangle_t, \tag{19}$$

v_R being the radial velocity and $\langle\ \rangle_t$ denoting the time average of bracketed quantity. In the first approximation, in accordance with Eq. (8) and pressure and velocity definitions, we obtain for the l — Bessel mode propagating to the open end

$$I_l(\vartheta, \varphi) = \frac{1}{2} \rho_0 c_0 k^2 |\Phi_l|^2, \tag{20}$$

and

$$S_l^{(I)}(R, \vartheta, \varphi) = \frac{1}{2} (\rho_0 c_0 k)^2 |\Phi_l|^2 R^2, \tag{21}$$

so comparing the last expression with the one proposed by WAJNSHTEJN [14] we see that

$$S_l^{(I)}(R, \vartheta, \varphi) = \zeta_0 K_l^{(I)}(R, \vartheta, \varphi), \tag{22}$$

$\zeta_0 = \rho_0 c_0$, being the specific impedance of the environment.

We extend Wajnshtejn's definition so that it should be adequate not only in the $kR \to \infty$ approximation, writing simply that

$$K_l^{(I)}(R, \vartheta, \varphi) = I(R, \vartheta, \varphi) R^2 \tag{23}$$

In the second approximation the intensity calculated according to Eq. (9) is equal to

$$I_l(R, \vartheta) = \left\langle k^2 \rho_0 c_0 D_l(R, \vartheta) \left[D_l(R, \vartheta) + \frac{i}{R} d_l(\vartheta) \right]^* \right\rangle_l \tag{24}$$

what gives the following intensity directivity formula:

$$S_l^{(I)}(R, \vartheta) = \frac{1}{2} (k \rho_0 c_0)^2 D_l(R, \vartheta) \left[D_l(R, \vartheta) + \frac{i}{R} d_l(\vartheta) \right]^*. \tag{25}$$

It is easy to notice that the last expression differs from the one we would have obtained using Wajnshtejn's formula (14) which would be proportional to $|D_l(R, \vartheta)|^2$. The difference appears as a consequence of the phase-shift between the pressure and velocity, the difference disappearing as the distance $R \to \infty$. The Wajnshtejn definition is valid only in the infinite distance approximation, otherwise we use the formula for the potential (9), in which the directivity coefficient $D_l(R, \vartheta)$ depends on the distance R neglecting at the same time the phase-shift between pressure and velocity.

After these remarks we can extend the definition of $s_l^{(I)}(\vartheta)$ for the points in finite distance from the outlet writing

$$s_l^{(I)}(R, \vartheta) = D_l(R, \vartheta) \left[D_l(R, \vartheta) + \frac{i}{R} d_l(\vartheta) \right]^*. \tag{26}$$

It is useful to compare the power radiated outside with the power transmitted by the incident l Bessel mode. To calculate these quantities we will remind the formula for the potential inside the pipe [2, 21]:

$$\Phi_l(\rho, z) = A_l \frac{J_0(\mu_l \rho / a)}{J_0(\mu_l)} \exp(-i\gamma_l z) + \sum_{n=0}^{N} R_{ln} A_l \frac{J_0(\mu_n \rho / a)}{J_0(\mu_n)} \exp(i\gamma_n z), \tag{27}$$

where R_{ln} is the complex reflection coefficient being the ratio of the complex amplitude of the n Bessel mode which appears in the duct due to diffraction and the amplitude l of the incident l mode, N is the index of the highest mode which can propagate without damping along the duct at a fixed diffraction parameter $ka(\mu_N < ka \leq \mu_{N+1})$. That lets us calculate the power propagated with the incident mode [2, 19]

$$P_l^{\text{inc}} = \frac{1}{2}\pi a^2 \rho_0 c_0 k \gamma_l |A_l|^2, \tag{28}$$

where πa^2 is the outlet surface.

Another quantity to be discussed is the power radiated outside [2].

$$P_l^{\text{rad}} = P_l^{\text{inc}} \left[1 - \left(\sum_{n=0}^{N} |R_{ln}|^2 \frac{\gamma_n}{\gamma_l}\right)\right], \tag{29}$$

the expression under the sum sign representing the residue part of energy in the wave guide.

Introducing the power reflection coefficient as

$$r_{ln} = |R_{ln}|^2 \frac{\gamma_n}{\gamma_l}, \tag{30}$$

and total reflection coefficient as

$$r_l = \sum_{n=0}^{N} r_{ln}, \tag{31}$$

we can express the power radiated from the pipe outlet [2] as

$$P_l^{\text{rad}} = P_l^{\text{inc}}(1 - r_l). \tag{32}$$

The power directivity function integrated over the total solid angle should be equal to the quantity of power radiated outside:

$$\int_0^{2\pi} d\varphi \int_0^{\pi} K_l^{(I)}(\vartheta, \varphi) \sin\vartheta \, d\vartheta = P_l^{\text{rad}}, \tag{33}$$

so, having in mind the axis-symmetric excitation, we obtain

$$2\pi \int_0^{\pi} K_l^{(I)}(\vartheta) \sin\vartheta \, d\vartheta = P_l^{\text{rad}}. \tag{34}$$

The quantity

$$\mathcal{G}(\vartheta) = \frac{K_l^{(I)}(\vartheta)}{P_l^{\text{rad}}/4\pi}, \tag{35}$$

called the power-gain function indicates what part of outside radiated energy has been shaped in a unit solid angle and it is obvious that

$$\int_0^{\pi} \mathcal{G}(\vartheta) \sin\vartheta \, d\vartheta = 2. \tag{36}$$

4. Results of numerical calculations. Conclusions

In the previous Section some of the features of the considered quantities have been presented theoretically. The results obtained allowed doctor J. Jurkiewicz from the Noise-Lab to derive the numerical programme to calculate the intensity directivity function and the power–gain function and to analyse the results obtained with dependence on the mode number, diffraction parameter and the distance from the output.

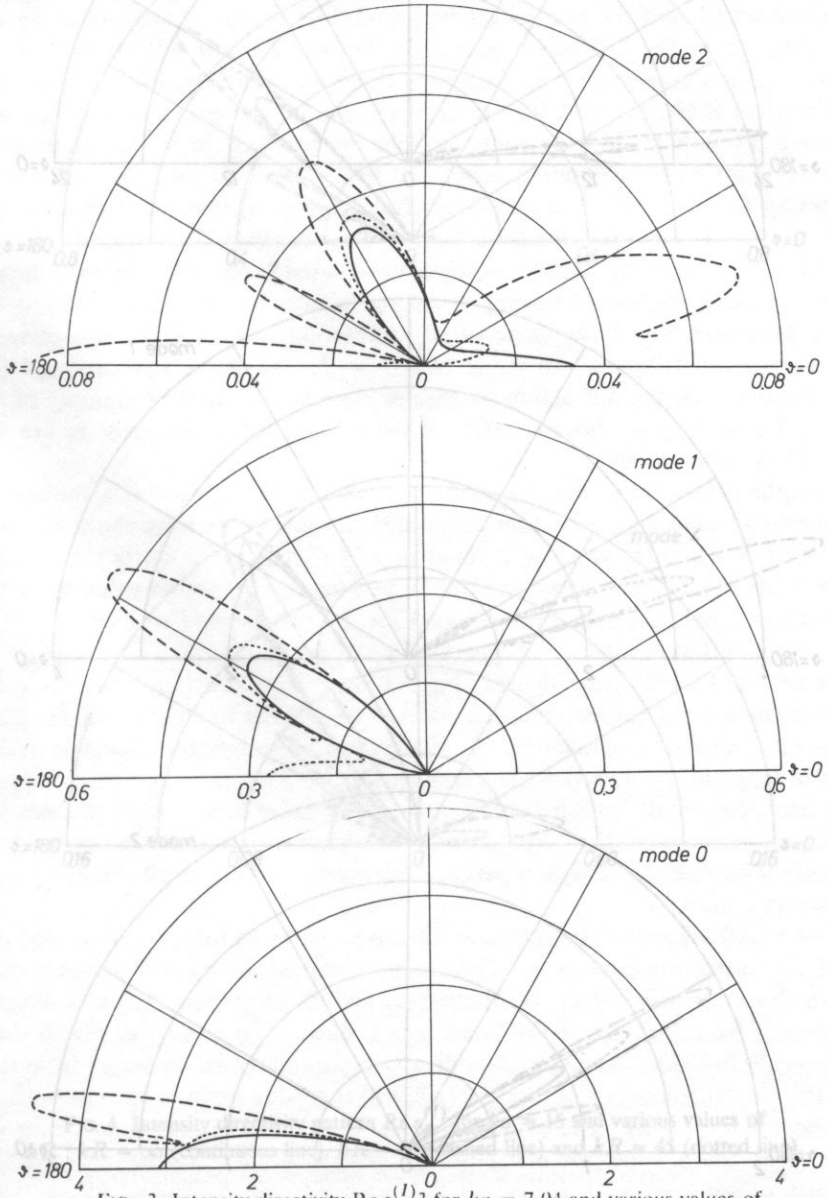

FIG. 3. Intensity directivity Re $s_l^{(1)}$ for $ka = 7.04$ and various values of kR : $kR = \infty$ (continuous line), $kR = 7$ (dashed line) and $kR = 21$ (dotted line).

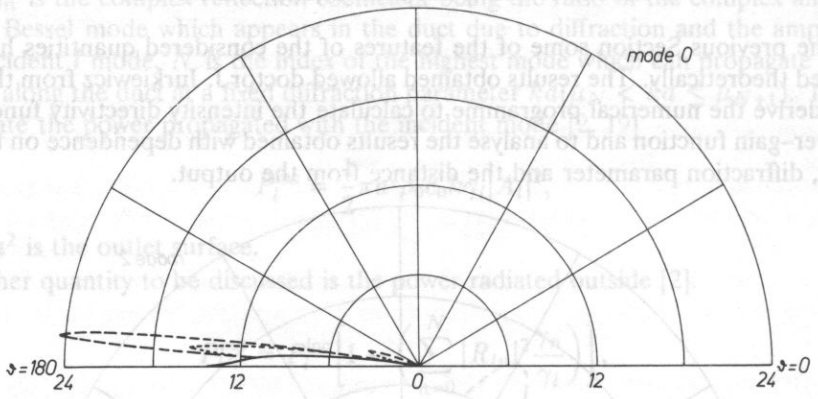
mode 0
ϑ=180
24
12
0
12
24
ϑ=0

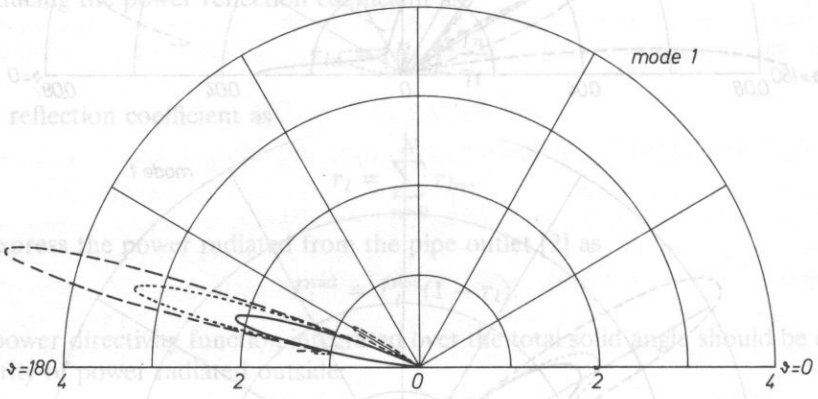
mode 1
ϑ=180
4
2
0
2
4
ϑ=0

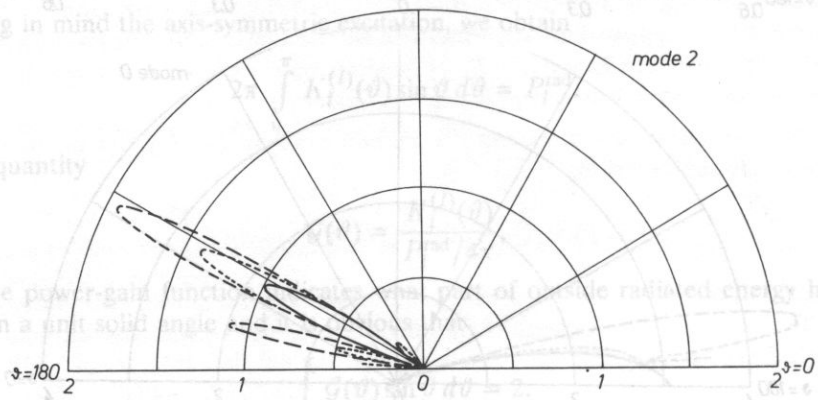
mode 2
ϑ=180
2
1
0
1
2
ϑ=0

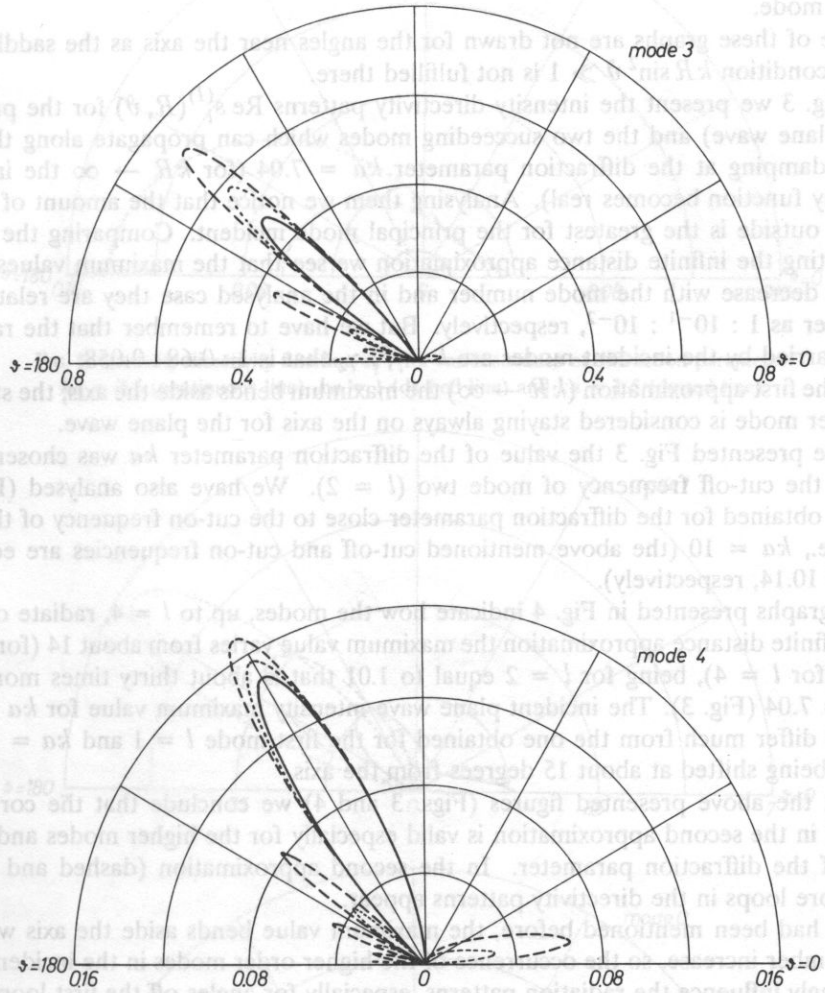

FIG. 4. Intensity directivity pattern $\mathrm{Re}\, s_1^{(I)}$ for $ka = 15$ and various values of kR : $kR = \infty$ (continuous line), $kR = 30$ (dashed line) and $kR = 45$ (dotted line).

The assumption was made that the single Bessel mode allowed for the fixed diffraction parameter, propagates towards the open end. The diffraction phenomena at the output was taken into account. In all the considered cases we assumed the unit amplitude of the incident mode.

Some of these graphs are not drawn for the angles near the axis as the saddle-point method condition $kR\sin^2\vartheta \gg 1$ is not fulfilled there.

In Fig. 3 we present the intensity directivity patterns $\mathrm{Re}\, s_l^{(I)}(R,\vartheta)$ for the principal mode (plane wave) and the two succeeding modes which can propagate along the duct without damping at the diffraction parameter $ka = 7.04$ (for $kR \to \infty$ the intensity directivity function becomes real). Analysing them we notice that the amount of energy radiated outside is the greatest for the principal mode incident. Comparing the graphs representing the infinite distance approximation we see that the maximum values of the intensity decrease with the mode number and in the analysed case they are related one to another as $1 : 10^{-1} : 10^{-2}$, respectively. But we have to remember that the ratios of energy carried by the incident modes are $k : \gamma_1 : \gamma_2$ that is $1 : 0.68 : 0.058$.

For the first approximation ($kR \to \infty$) the maximum bends aside the axis, the stronger the higher mode is considered staying always on the axis for the plane wave.

In the presented Fig. 3 the value of the diffraction parameter ka was chosen to be close to the cut-off frequency of mode two ($l = 2$). We have also analysed (Fig. 4) the date obtained for the diffraction parameter close to the cut-on frequency of the next mode, i.e., $ka = 10$ (the above mentioned cut-off and cut-on frequencies are equal to 7.02 and 10.14, respectively).

The graphs presented in Fig. 4 indicate how the modes, up to $l = 4$, radiate outside. In the infinite distance approximation the maximum value varies from about 14 (for $l = 0$) to 0.14 (for $l = 4$), being for $l = 2$ equal to 1.01 that is about thirty times more than for $ka = 7.04$ (Fig. 3). The incident plane wave intensity maximum value for $ka = 7.04$ does not differ much from the one obtained for the first mode $l = 1$ and $ka = 15$, the last one being shifted at about 15 degrees from the axis.

From the above presented figures (Figs. 3 and 4) we conclude that the correction obtained in the second approximation is valid especially for the higher modes and larger values of the diffraction parameter. In the second approximation (dashed and dotted lines) more loops in the directivity patterns appear.

As it had been mentioned before, the maximum value bends aside the axis with the mode number increase, so the occurrence of the higher order modes in the incident wave can strongly influence the radiation patterns, especially for angles off the first loop of the plane wave radiation.

Figures 5 and 6 present the intensity directivity patterns for $kR \to \infty$ and different values of the diffraction parameter. The results obtained for $ka = 1$ are in good agreement with these obtained by G. W. JOHNSTON and K. OGIMOTO [12] as a limiting case in considering radiation out of the finite length duct. The graphs in Fig. 6 show how the power–gain function changes if the diffraction parameter ka increases from the value close to the cut-off frequency of mode 1 (3.83) to the value close to the cut-on frequency of the next mode (7.016). The principal mode has always its maximum in the forward direction ($\vartheta = 180°$), while the maximum of the first mode bends towards the axis with the increase of ka.

In the next two figures (Figs. 7 and 8) we present the power–gain function for different

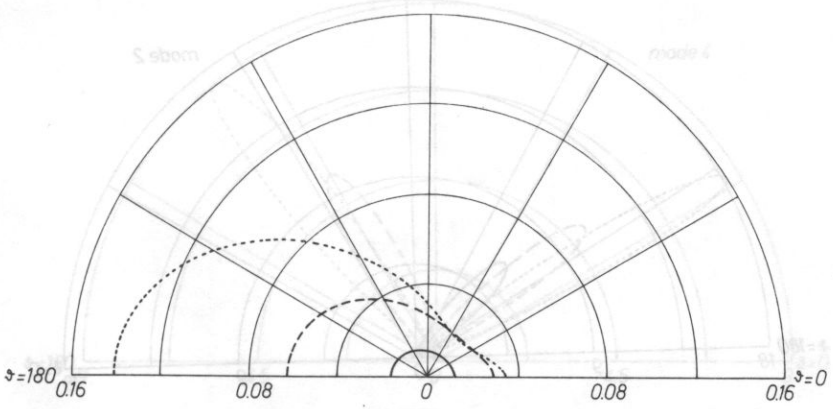

FIG. 5. Intensity directivity function $s_l^{(I)}$ for various values of diffraction parameter: $ka = 0.5$ (continuous line), $ka = 1$ (dashed line) and $ka = 1.5$ (dotted line).

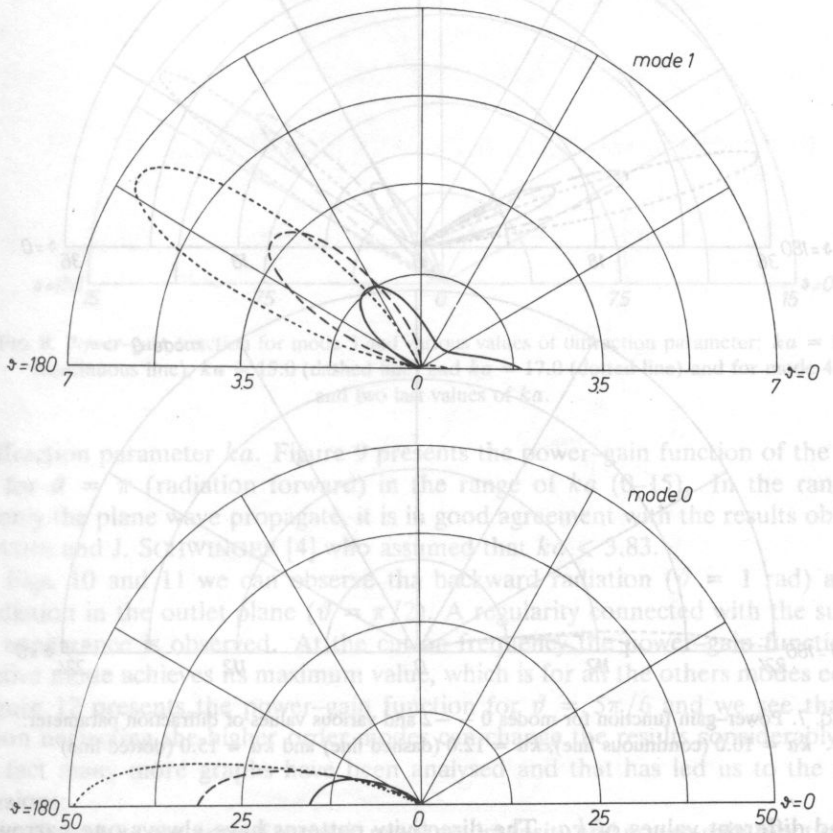

FIG. 6. Power–gain function for modes 0–2 and various values of diffraction parameter: $ka = 3.85$ (continuos line), $ka = 5.5$ (dashed line) and $ka = 7.0$ (dotted line).

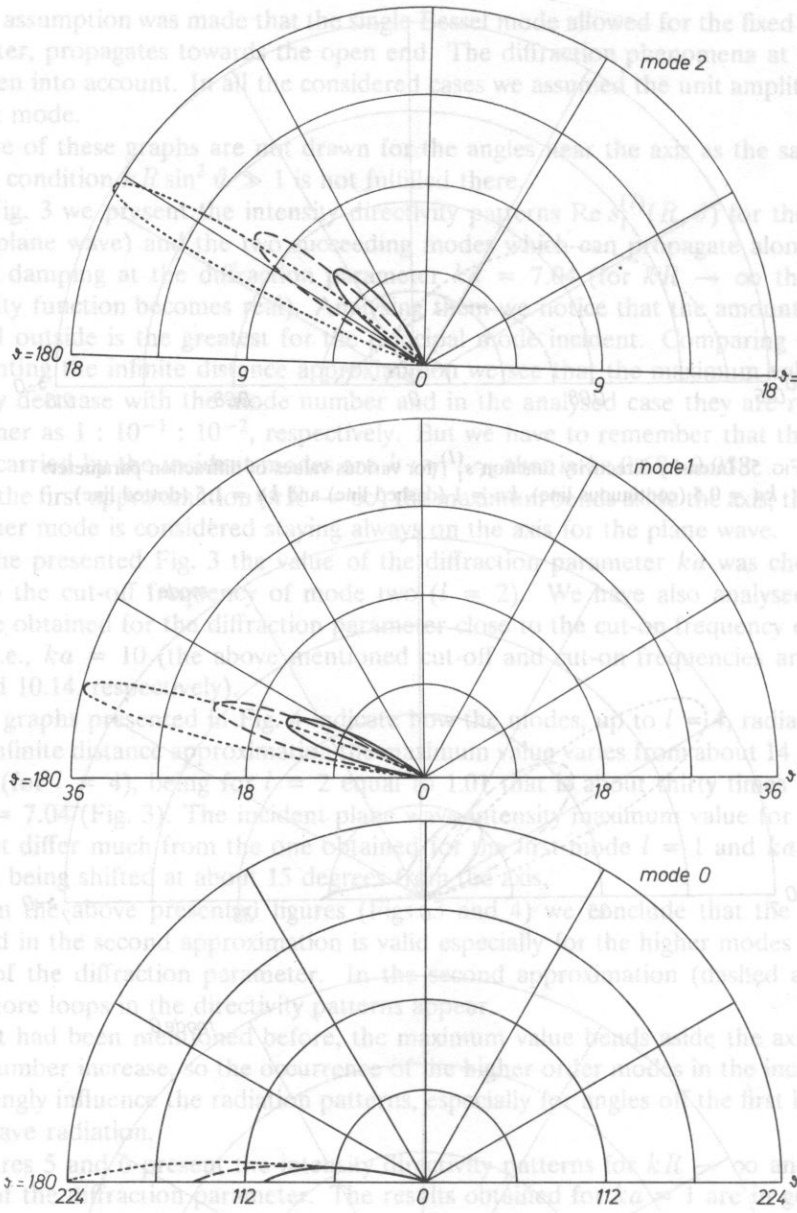

FIG. 7. Power–gain function for modes $0 - -2$ and various values of diffraction parameter: $ka = 10.0$ (continuous line), $ka = 12.0$ (dashed line) and $ka = 15.0$ (dotted line)

modes and different values of ka. The directivity patterns have always one narrow loop which shifts from the axis with the mode number increase, but for the same mode ($n = 0$) its maximum bends towards the axis for larger ka.

The next figures show how the power–gain function of the fixed angle changes with

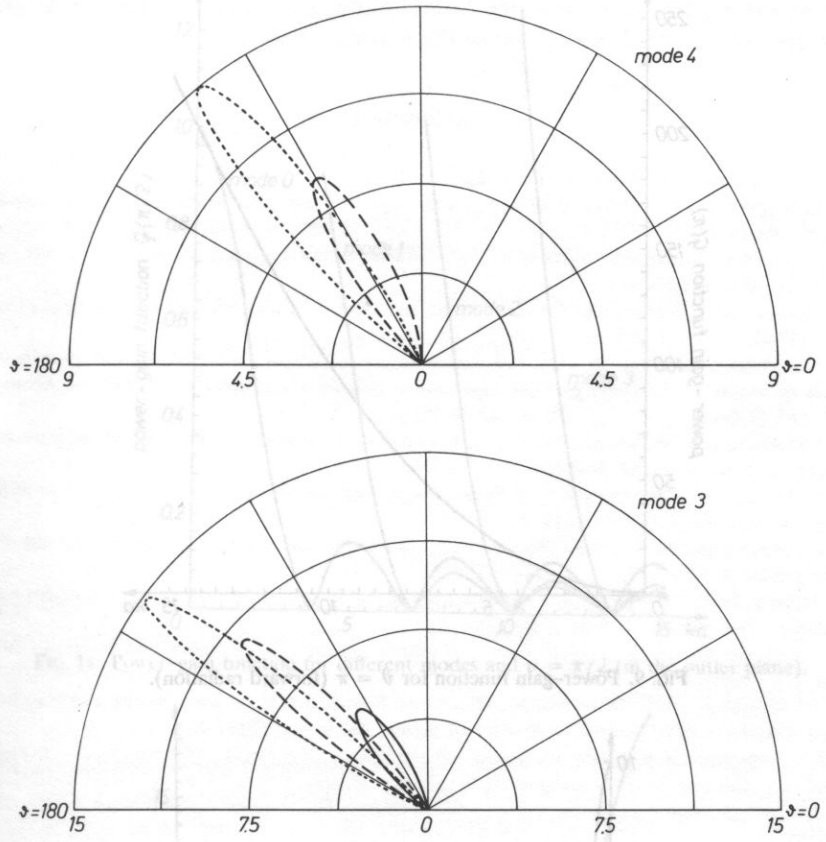

FIG. 8. Power–gain function for mode 3 and various values of diffraction parameter: $ka = 12.0$ (continuous line), $ka = 15.0$ (dashed line) and $ka = 17.0$ (dotted line) and for mode 4 and two last values of ka.

the diffraction parameter ka. Figure 9 presents the power–gain function of the principal mode for $\vartheta = \pi$ (radiation forward) in the range of ka (0–15). In the range of ka when only the plane wave propagate, it is in good agreement with the results obtained by H. LEVINE and J. SCHWINGER [4] who assumed that $ka < 3.83$.

In Figs. 10 and 11 we can observe tha backward radiation ($\vartheta = 1$ rad) as well as the radiation in the outlet plane ($\vartheta = \pi/2$). A regularity connected with the succeeding mode appearance is observed. At the cut-on frequency the power–gain function of the respective mode achieves its maximum value, which is for all the others modes equal to 0.

Figure 12 presents the power–gain function for $\vartheta = 5\pi/6$ and we see that in that direction neglecting the higher order modes can change the results considerably.

In fact many more graphs have been analysed and that has led us to the following conclusions:

– the directivity patterns of acoustic pressure, intensity and power-gain function depend strongly on the number of the Bessel mode incident

– the maximum values bend aside the axis with the mode number increase

– the correction obtained in the second approximation is valid especially for the higher

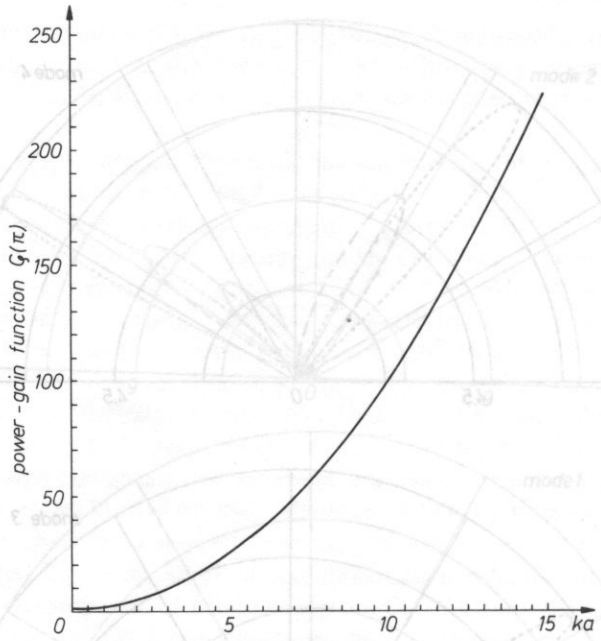

FIG. 9. Power–gain function for $\vartheta = \pi$ (forward radiation).

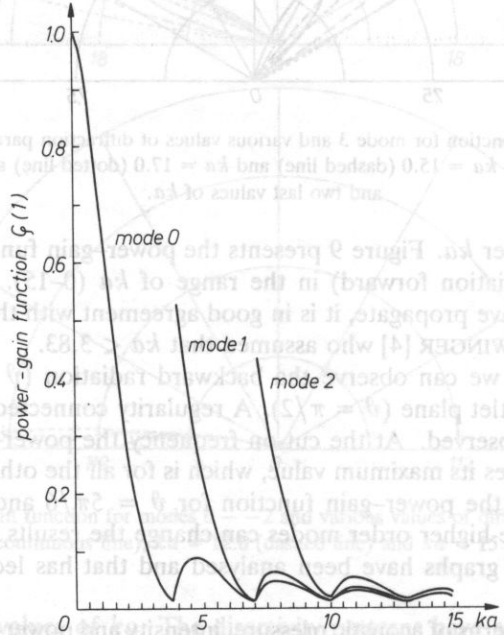

FIG. 10. Power–gain function for different modes and $\vartheta = 1$ (backward radiation).

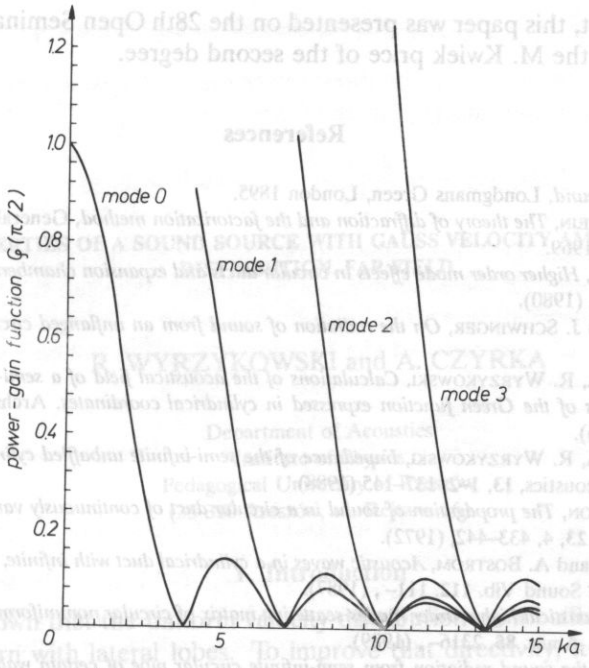

FIG. 11. Power–gain function for different modes and $\vartheta = \pi/2$ (in the outler plane).

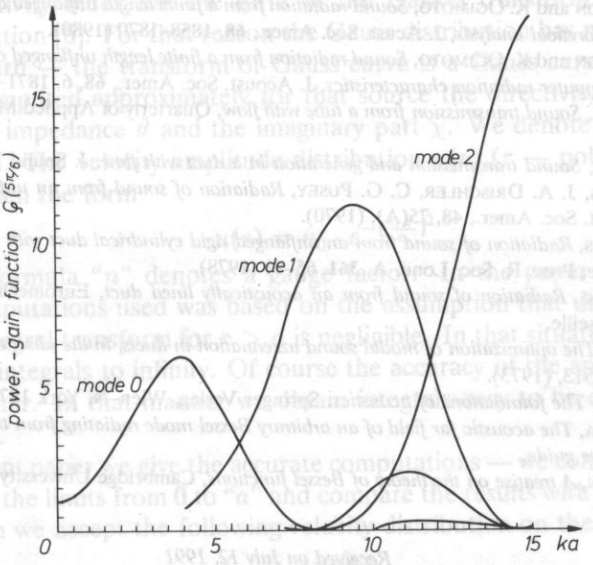

FIG. 12. Power–gain function for different modes and $\vartheta = 5\pi/6$.

modes and larger values of the diffraction parameter

– a regularity connected with the succeeding mode appearance is observed.

From the above presented results it is undoubtful that in many analyses of the energy distribution the plane wave approximation can yield significant errors.

To some extent, this paper was presented on the 28th Open Seminar on Acoustics and was honoured by the M. Kwiek price of the second degree.

References

[1] J. TYNDALL, *Sound*, Londgmans Green, London 1895.

[2] L. A. WAJNSHTEJN, *The theory of diffraction and the factorization method*, Generalized Wiener-Hopf technique, Golem 1969.

[3] L. J. ERIKKSON, *Higher order mode effects in circular ducts and expansion chambers*, J. Acoust. Soc. Amer., **68**, 2, 545–550, (1980).

[4] H. LEVINE and J. SCHWINGER, *On the radiation of sound from an unflanged circular pipe*, Phys. Rev. **73**, 383- (1948).

[5] A. SNAKOWSKA, R. WYRZYKOWSKI, *Calculations of the acoustical field of a semi-infinite cylindrical waveguide by means of the Green function expressed in cylindrical coordinates*. Archives of Acoustics, **11**, 3, 261–285, (1986).

[6] A. SNAKOWSKA, R. WYRZYKOWSKI, *Impedance of the semi-infinite unbaffled cylindrical wave-guide outlet*, Archives of Acoustics, **13**, 1–2, 137–145 (1988).

[7] R. J. ALFREDSON, *The propagation of sound in a circular duct of continuously varying cross-sectional area*, J. Sound Vib., **23**, 4, 433–442, (1972).

[8] L. LUNDOVIST and A. BOSTRÖM, *Acoustic waves in a cylindrical duct with infinite, half-infinite or finite wall corrugations*, J. Sound Vib. **112**, 111– , (1987).

[9] H. HUDDE, *Acoustical higher-order modes scattering matrix of circular nonuniform lossy tubes without flow*, J. Acoust. Soc. Amer. **85**, 2316– , (1989).

[10] Y. ANDO, *On the sound radiation from semi-infinite circular pipe of certain wall thickness*. Acustica, **22**, 219–225, (1969).

[11] G. W. JOHNSTON and K. OGIMOTO, *Sound radiation from a finite length unflanged circular duct with uniform axial flow. Theoretical analysis*, J. Acust. Soc. Amer., **68**, 1858–1870 (1980).

[12] G. W. JOHNSTON and K. OGIMOTO, *Sound radiation from a finite length unflanged circular duct with uniform axial flow. Computer radiation characteristics*, J. Acoust. Soc. Amer., **68**, 6, 1871–1883 (1980).

[13] G. F. CARRIER, *Sound transmission from a tube with flow*, Quarterly of Applied Mathematics, **13**, 453–461, (1956).

[14] C. L. MORFEY, *Sound transmission and generation in a duct with flow*, J. Sound Vib., **14**, 37–55, (1971).

[15] D. L. LANSING, J. A. DRISCHLER, C. G. PUSEY, *Radiation of sound from an unflanged circular duct with flow*, J. Acoust. Soc. Amer., **48**, 75(A), (1970).

[16] A. D. RAWLINS, *Radiation of sound from an unflanged rigid cylindrical duct with an acoustically absorbing internal surface*, Proc. R. Soc. Lond. A. **361**, 65–91 (1978).

[17] A. D. RAWLINS, *Radiation of sound from an acoustically lined duct*, Euromech 94 Conference held at C.N.R.S. Marseille.

[18] B. J. TESTER, *The optimization of modal sound azzenuation in ducts, in the absence of mean flow*, J. Sound Vib., **27**, 477–513, (1973).

[19] E. SKUDRZYK, *The foundations of acoustics*. Springer-Verlag, Wien–N. York 1971.

[20] A. SNAKOWSKA, *The acoustic far field of an arbitrary Bessel mode radiating from the semi infinite unflanged cylindrical wave guide*,

[21] G. N. WATSON, *A treatise on the theory of Bessel functions*, Cambridge University Press, Cambridge, 1958.

Received on July 12, 1991

ARCHIVES OF ACOUSTICS
17, 4, 543–553 (1992)

PROPERTIES OF A SOUND SOURCE WITH GAUSS VELOCITY AMPLITUDES DISTRIBUTION. FAR FIELD

R. WYRZYKOWSKI and A. CZYRKA

Department of Acoustics
Institute of Physics
Pedagogical University of Rzeszów
(35-310 Rzeszów, ul. Rejtana 16)

1. Introduction

It is well known that the uniform velocity distribution on a baffled piston results in a directivity pattern with lateral lobes. To improve that directivity, it is necessary to look for variable velocity distribution. The first one computed was Gauss curve distribution [8]. The directivity index has the form of the Hankel transform (zero order) of the velocity distribution [6]. For that reason the Gauss distribution has no lateral lobes in the directivity pattern — the transform of Gauss curve is a Gauss curve, too. In the paper [7] we have computed approximately for that source the directivity pattern R, the real part of relative impedance θ and the imaginary part χ. We denote by "a" the radius of a baffled piston. The velocity amplitude distribution $u(r)$ (r — polar coordinate on the piston) takes then the form

$$u(r) = u_0 \cdot e^{-(\frac{n \cdot r}{a})^2}, \tag{1}$$

In the above formula "n" denotes a gauge factor. In the paper [7] the approximate method of computations used was based on the assumption that the contribution to the value of the integral transform for $r > a$ is negligible. In that situation we can extend the corresponding integrals to infinity. Of course the accuracy of the approximation is better when n is greater. In that manner we obtain integrals easy to be computed in a closed analytical form.

In the present paper we give the accurate computations — we compute the corresponding integrals in the limits from 0 to "a" and compare the results with the appoximate ones. For that reason we accept the following velocity distribution on the piston

$$u(r) = \begin{cases} u_0 \cdot e^{-(\frac{n \cdot r}{a})^2} & 0 \leq r \leq a \\ 0 & r > a \end{cases}. \tag{2}$$

Nevertheless, to maintain the continuity of our reasoning we begin by reminding the basic formulae of the approximate theory [7]. This is necessary also from another point of view. In the paper [7] we did not use the gauge factor n and the corresponding formulae must now we written in a corrected form. The near field of such a source was computed in [9].

2. Theoretical basis of computations and summary of the approximate method

According to the paper [6], the directivity pattern of a source with symmetry center and the velocity distribution $u(r)$ has the form

$$R(ka \cdot \sin\gamma) = \frac{2 \cdot \pi}{Q} \int_0^a u(r) \cdot J_0(kr \cdot \sin\gamma) \cdot r \cdot dr. \tag{3}$$

In the above formula Q denotes the volume output of the source. $J_0()$ is the Bessel function of zero order, k the wave number, γ the angle between the field point direction and the "z" axis perpendicular to the piston at its center. The formula (3) represents the Hankel transform of zero order of the function $u(r)$ [8] in the case when $u(r)$ equals 0 for $r > a$. In our case (2) the directivity pattern equals

$$R(ka \cdot \sin\gamma) = \frac{2 \cdot \pi \cdot u_0}{Q} \int_0^a e^{-(\frac{n \cdot r}{a})^2} J_0(kr \cdot \sin\gamma) \cdot r \cdot dr, \tag{4}$$

If we take the upper limit of the integral (4) "∞" instead of "a", we get the approximate value

$$R(ka \cdot \sin\gamma) = \frac{2 \cdot \pi \cdot u_0}{Q} \int_0^\infty e^{-(\frac{n \cdot r}{a})^2} \cdot J_0(kr \cdot \sin\gamma) \cdot r \cdot dr. \tag{5}$$

The source output Q equals (for the approximate case)

$$Q = 2 \cdot \pi \cdot u_0 \int_0^\infty e^{-(\frac{n \cdot r}{a})^2} \cdot r \cdot dr. \tag{6}$$

Computing the elementary integral (6), we get

$$Q = \pi \cdot u_0 \cdot \left(\frac{a}{n}\right)^2. \tag{7}$$

The integral in the formula (3) is given in tables of integrals [2 p. 731] and with Eq. (7) we get the directivity index (5) in the form

$$R(ka \cdot \sin\gamma) = e^{-(\frac{ka \cdot \sin\gamma}{2n})^2}. \tag{8}$$

It is, as we may expect, a Gauss distribution, too.

As we know, by increasing "n" we decrease the error of the approximate method, but simultaneously we deteriorate the directivity. We will see it exactly, later on, in the discussion of the results.

Now we begin the computation of the real part θ of the specific impedance of the above considered source and its imaginary part χ. In the case of a uniform velocity distribution we have [6]

$$\theta(ka) = \frac{k^2 \cdot S}{2 \cdot \pi} \cdot \int_0^{\frac{\pi}{2}} R^2(ka \cdot \sin\gamma) \cdot \sin\gamma \cdot d\gamma, \tag{9}$$

where S denotes the area of the piston. In the case of variable velocity distribution we

must introduce in the formula (9) a coefficient κ normalizing $\lim_{ka\to\infty}\theta$ to unity. Then

$$\theta(ka) = \frac{k^2 \cdot S}{2 \cdot \pi} \cdot \kappa \cdot \int_0^{\frac{\pi}{2}} R^2(ka \cdot \sin\gamma) \cdot \sin\gamma \cdot d\gamma. \tag{10}$$

It is sufficient to examine the classic reasoning leading to the formula (9) to understand that it was computed by equating the acoustic power radiated on the source to the entire power in the far field. In the first case, that power expressed by θ is proportional to the mean value of the square of velocity amplitude. In the second case it is proportional to the square of the output, i.e., to the square of the mean value of the velocity amplitude. Therefore the coefficient κ equals

$$\kappa = \frac{(u_m)^2}{(u)_m^2} \tag{11}$$

Sometimes it is possible to compute κ immediately from the condition

$$\lim_{ka\to\infty} \theta(ka) = 1. \tag{12}$$

Of course the formula (10) is a general one and, depending on the substitution — accurate or approximate value of $R(ka\sin\gamma)$, we get the accurate or approximate value of $\theta(ka)$.

We know two methods of computing the imaginary part from the real part θ. The first one consists in computing the Hilbert transform of the real part:

$$\chi(ka) = \frac{1}{\pi} \int_{-\infty}^{+\infty} \frac{\theta(x)}{x - ka} \cdot dx. \tag{13}$$

The second one, developed by RDZANEK [5] consists in substituting, in the formula (10) $\cosh\psi$ instead of $\sin\gamma$ and integrating from 0 to ∞.

$$\chi(ka) = \frac{k^2 \cdot S}{2 \cdot \pi} \cdot \int_0^{\infty} R^2(ka \cdot \cosh\psi) \cdot \cosh\psi \, d\psi. \tag{14}$$

The formulae (13) and (14) give us an accurate or approximate value depending on the accepted value of R. Returning to the approximate method, we confine our computations to the results given in the paper [7]. We have the coefficient computed from the formula (11) in the form

$$\kappa = \frac{2}{n^2}. \tag{15}$$

The following formulae are simpler if we introduce the so-called diffraction parameter w

$$w = \frac{ka}{\sqrt{2}}. \tag{16}$$

We write, according to (7)

$$\theta(w) = 2 \cdot \frac{w}{n} \cdot D\left(\frac{w}{n}\right) \tag{17}$$

where the so-called Dawson integral or Dawson formula [1] is given in the form

$$D(x) = e^{-x^2} \cdot \int_0^x \cdot e^{t^2} \cdot dt \tag{18}$$

The imaginary part of the specific impedance was computed in [7] by means of the Hilbert transform (13) and has the form

$$\chi = \sqrt{\pi} \cdot \frac{w}{n} \cdot e^{-(\frac{w}{n})^2} \tag{19}$$

The calculated values of R, θ and χ (for the approximated method) will be shown in corresponding figures together with the accurate ones. An interesting result is obtained by equating Eq. (19) to (14); of course we must substitute in the last one the value (16) for κ. Writing x instead of ψ, we get

$$\int_0^\infty e^{-t^2 \cdot \cosh^2 x} \cdot \cosh x \cdot dx = \frac{\sqrt{\pi}}{t} \cdot e^{-t^2}. \tag{20}$$

The formula (20) gives a new definite integral, until now not computed and not given in any tables.

3. Accurate method — directivity index

Our starting point is now the formula (4) where we have the source output Q. That output must be computed exactly i.e., instead of the formula (6) we write the analogous integral but in the limits from "0" to "a". We obtain in that way

$$Q = 2 \cdot \pi \cdot u_0 \int_0^a e^{-(\frac{n \cdot r}{a})^2} \cdot r \cdot dr \tag{21}$$

The integral in (21) is an elementary one and owing to that output Q takes the form

$$Q = \pi \cdot u_0 \cdot \left(\frac{a}{n}\right)^2 \cdot (1 - e^{-n^2}) \tag{22}$$

Substituting Eq. (22) to the formula (4) for the directivity index, we get it in the form

$$R(ka \cdot \sin\gamma) = \frac{2 \cdot (\frac{n}{a})^2}{1 - e^{-n^2}} \int_0^a e^{-(\frac{n \cdot r}{a})^2} \cdot J_0(kr \cdot \sin\gamma) \cdot r \cdot dr \tag{23}$$

In the formula (23) we introduce a new variable

$$x = \frac{r}{a}, \tag{24}$$

and get

$$R(ka \cdot \sin\gamma) = \frac{2 \cdot n^2}{1 - e^{-n^2}} \int_0^1 e^{-n^2 \cdot x^2} \cdot J_0(ka \cdot \sin\gamma \cdot x) \cdot x \cdot dx \tag{25}^*$$

The r.h.s. of the formula (25) may be integrated. To simplify the integration we denote

$$ka \cdot \sin\gamma = b. \tag{26}$$

and

$$x = \frac{1}{b} \cdot y. \tag{27}$$

* The author is grateful to dr J. Janczar for analytical integration of (25).

Then:

$$R(b) = \frac{2 \cdot n^2}{(1 - e^{-n^2})b^2} \int_0^b e^{\frac{-n^2}{b^2} \cdot y^2} y \cdot J_0(y)\, dy. \tag{28}$$

We use the integration by parts and obtain:

$$R(b) = \frac{1}{e^{n^2} - 1} \sum_{m=0}^{\infty} (2n^2)^{m+1} \cdot \frac{J_{m+2}(b)}{b^{m+1}}. \tag{29}$$

One must check whether the directivity pattern equals "one" for $\sin\gamma = 0$. In that case we have $b = 0$ and [2]:

$$\lim_{b \to \infty} \frac{J_{m+2}(b)}{b^{m+1}} = \frac{1}{(n+1)! \cdot 2^{m+1}}. \tag{30}$$

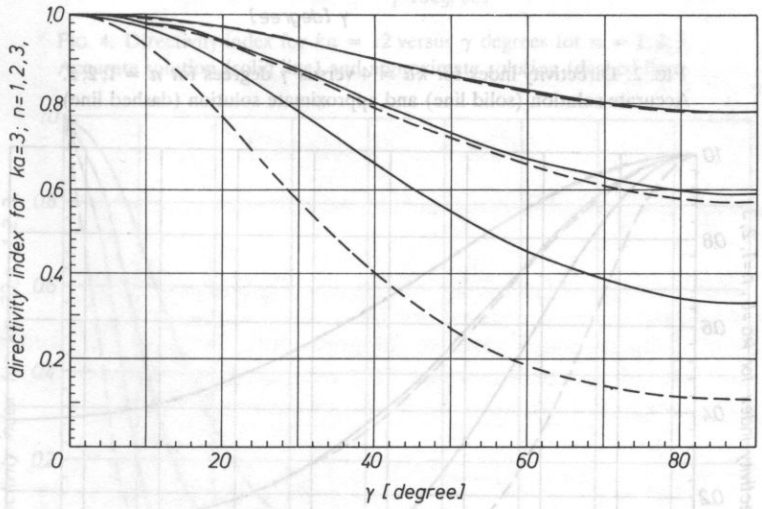

FIG. 1. Directivity index for $ka = 3$ versus γ degrees for $n = 1; 2; 3$. Accurate solution (solid line) and approximate solution — (dashed line).

The directivity pattern equals then:

$$R(0) = \frac{1}{e^{n^2} - 1} \sum_{m=1}^{\infty} \frac{(n^2)^m}{m!} = \frac{1}{e^{n^2} - 1}(e^{n^2} - 1) = 1. \tag{31}$$

Of course we have for $b \ll 1$

$$R(b) \approx 1. \tag{32}$$

For $b \gg 1$ and $b > 2n^2$ we have approximately:

$$R(b) \approx \frac{2n^2}{e^{n^2} - 1} \cdot \frac{J_1(b)}{b}, \tag{33}$$

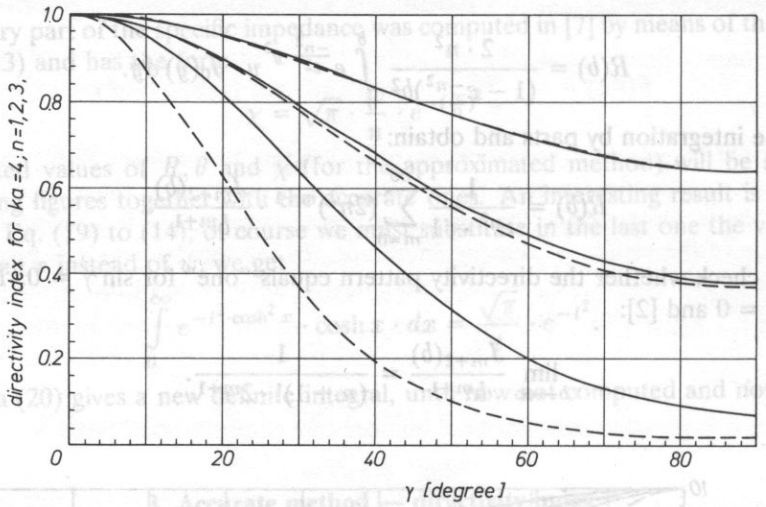

FIG. 2. Directivity index for $ka = 4$ versus γ degrees for $n = 1; 2; 3$. Accurate solution (solid line) and approximate solution (dashed line).

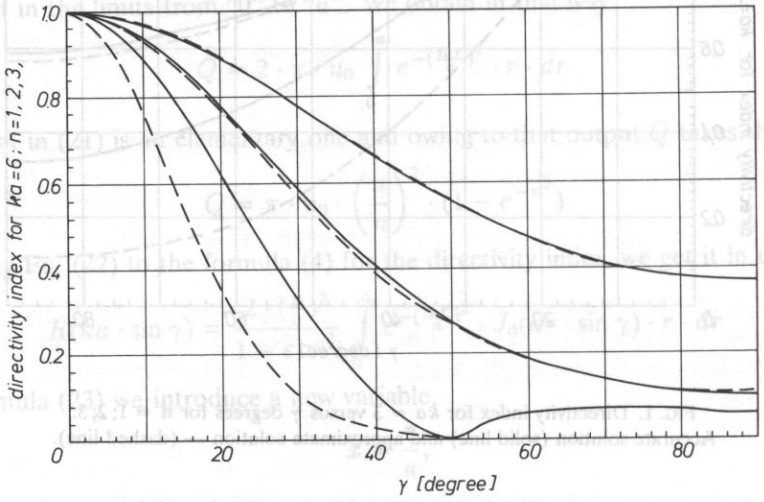

FIG. 3. Directivity index for $ka = 6$ versus γ degrees for $n = 1; 2; 3$. Accurate solution (solid line) and approximate solution (dashed line).

or finally:

$$R(ka\sin\gamma) \approx \frac{2n^2}{e^{n^2}-1} \cdot \frac{J_1(ka\sin\gamma)}{ka\sin\gamma}. \tag{34}$$

Of course, for convenience we may always write formally:

$$R(ka\sin\gamma) = \frac{R^{\infty}(ka\cdot\sin\gamma)}{1-e^{-n^2}} \cdot F(n, ka\cdot\sin\gamma), \tag{35}$$

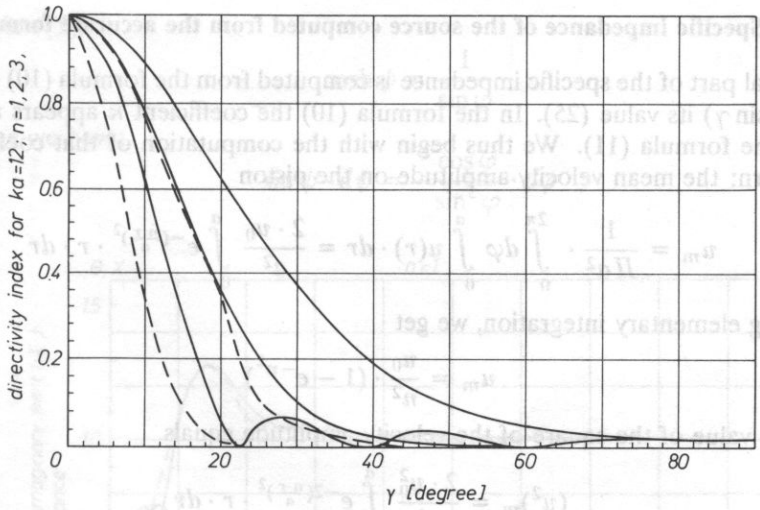

FIG. 4. Directivity index for $ka = 12$ versus γ degrees for $n = 1; 2; 3$. Accurate solution (solid line) and approximate solution (dashed line).

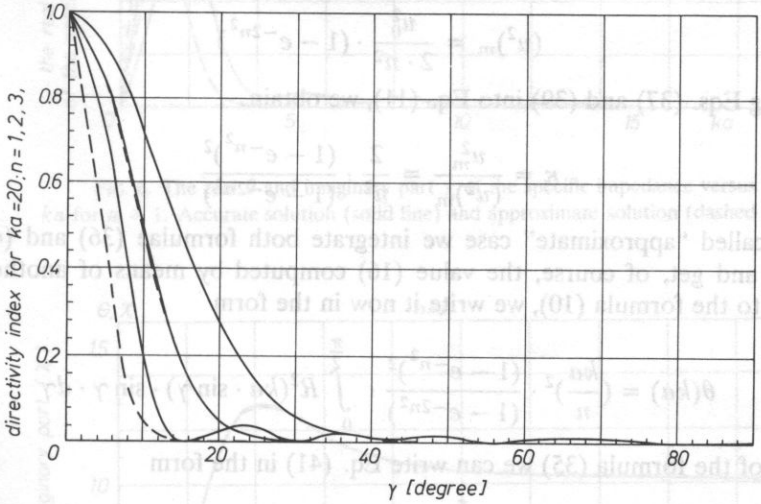

FIG. 5. Directivity index for $ka = 20$ versus γ degrees for $n = 1; 2; 3$. Accurate solution (solid line) and approximate solution (dashed line).

where $R^{\infty}(ka \cdot \sin\gamma)$ denotes the approximate value.

The enclosed figures (Fig. 1–5) represent the directivity index versus the angle γ for different values of ka. The continuous line represents the „accurate" values, the dashed line the approximated ones. It is easily seen that the difference between both values is considerable for $n = 1$, still observable, but small for $n = 2$ and practically does not exist for $n = 3$. We notice also that that difference decreases when ka increases. We see, therefore, that for $n = 2$ and $ka > 6$ it is possible to use approximate formulae instead of accurate ones.

4. Specific impedance of the source computed from the accurate formulae

The real part of the specific impedance is computed from the formula (10) substituting for $R(ka\sin\gamma)$ its value (25). In the formula (10) the coefficient κ appears and express itself by the formula (11). We thus begin with the computation of that coefficient. We have in turn: the mean velocity amplitude on the piston

$$u_m = \frac{1}{\Pi a^2} \cdot \int_0^{2\pi} d\varphi \int_0^a u(r) \cdot dr = \frac{2 \cdot u_0}{a^2} \int_0^a e^{-(\frac{n \cdot r}{a})^2} \cdot r \cdot dr \tag{36}$$

Performing elementary integration, we get

$$u_m = \frac{u_0}{n^2} \cdot (1 - e^{-n^2}) \tag{37}$$

The mean value of the square of the velocity amplitude equals

$$(u^2)_m = \frac{2 \cdot u_0^2}{a^2} \int_0^a e^{-2(\frac{n \cdot r}{a})^2} \cdot r \cdot dr \tag{38}$$

The integral (38) is an elementary one, too and we get

$$(u^2)_m = \frac{u_0^2}{2 \cdot n^2} \cdot (1 - e^{-2n^2}) \tag{39}$$

Substituting Eqs. (37) and (39) into Eq. (11), we obtain

$$\kappa = \frac{u_m^2}{(u^2)_m} = \frac{2}{n^2} \cdot \frac{(1 - e^{-n^2})^2}{(1 - e^{-2n^2})} \tag{40}$$

In the so-called "approximate" case we integrate both formulae (36) and (40) from 0 to infinity and get, of course, the value (16) computed by means of another method. Returning to the formula (10), we write it now in the form

$$\theta(ka) = (\frac{ka}{n})^2 \cdot \frac{(1 - e^{-n^2})^2}{(1 - e^{-2n^2})} \cdot \int_0^{\frac{\pi}{2}} R^2(ka \cdot \sin\gamma) \cdot \sin\gamma \cdot d\gamma \tag{41}$$

By means of the formula (35) we can write Eq. (41) in the form

$$\theta(ka) = (\frac{ka}{n})^2 \cdot \frac{1}{1 - e^{-2n^2}} \cdot \int_0^{\frac{\pi}{2}} e^{-\frac{1}{2}(\frac{ka \cdot \sin\gamma}{n})^2} \cdot F^2(n, ka \cdot \sin\gamma) \cdot \sin\gamma \cdot d\gamma \tag{42}$$

We are here computing the imaginary part of the specific impedance ka by means of the formula (14), i.e., by substituting in Eq. (42) $\cosh\psi$ instead of $\sin\gamma$ and integrating from 0 to infinity

$$\chi(ka = (\frac{ka}{n})^2 \cdot \frac{1}{1 - e^{-2n^2}} \cdot \int_0^{\infty} e^{-\frac{1}{2}(\frac{ka \cdot \cosh\psi}{n})^2} \cdot F^2(n, ka \cdot \cosh\psi) \cdot \cosh\psi \cdot d\psi \tag{43}$$

The numerical evaluation of (43) is difficult owing to the infinite limit of the integral, and strongly increasing function $\cosh\psi$. To avoid this difficulty we may apply the following

substitution [5]:

$$\cosh\psi = \frac{1}{\sin\varphi} \tag{44}$$

Of course we have:

$$\sin\psi \cdot d\psi = -\frac{\cos\varphi}{\sin^2\varphi} \cdot d\varphi \tag{45}$$

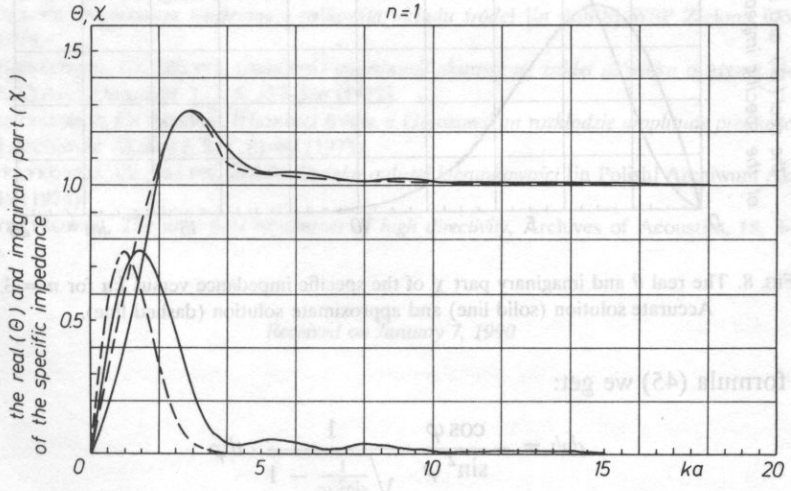

FIG. 6. The real θ and imaginary part χ of the specific impedance versus ka for $n = 1$. Accurate solution (solid line) and approximate solution (dashed line).

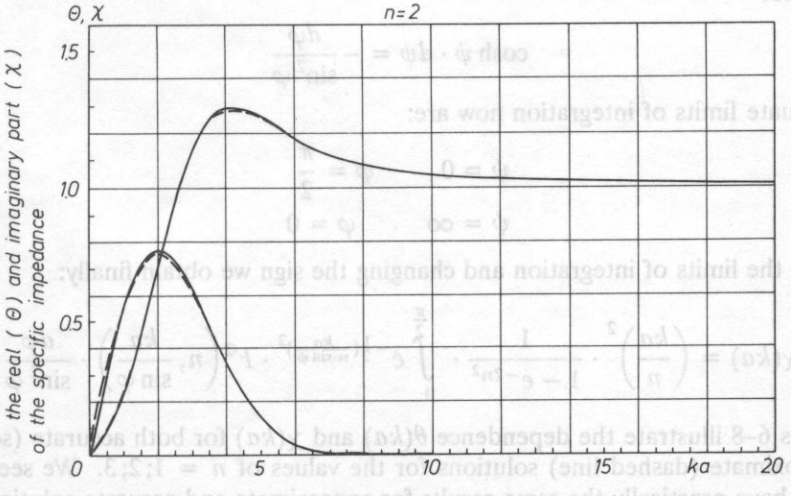

FIG. 7. The real θ and imaginary part χ of the specific impedance versus ka for $n = 2$. Accurate solution (solid line) and approximate solution (dashed line).

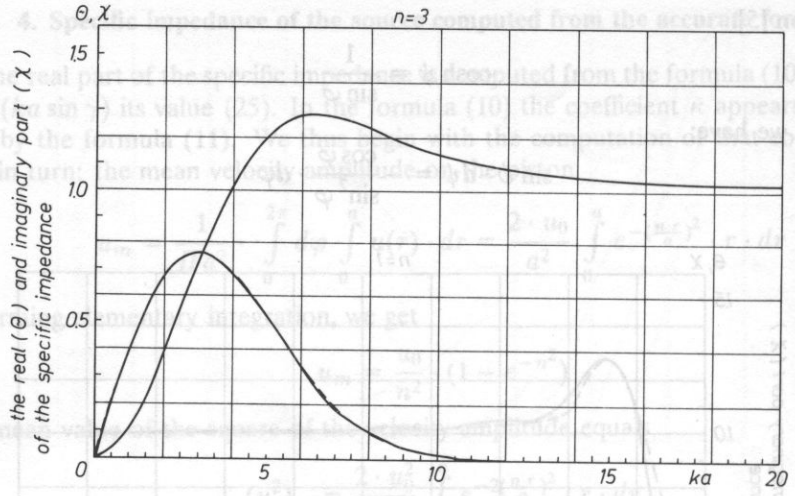

FIG. 8. The real θ and imaginary part χ of the specific impedance versus ka for $n = 3$. Accurate solution (solid line) and approximate solution (dashed line).

From the formula (45) we get:

$$d\psi = -\frac{\cos\varphi}{\sin^2\varphi} \cdot \frac{1}{\sqrt{\frac{1}{\sin^2\varphi} - 1}} \cdot d\varphi \tag{46}$$

or:

$$d\psi = -\frac{d\varphi}{\sin\varphi} \tag{47}$$

We get also:

$$\cosh\psi \cdot d\psi = -\frac{d\varphi}{\sin^2\varphi} \tag{48}$$

The adequate limits of integration now are:

$$\begin{aligned} \psi &= 0 \qquad \varphi = \frac{\pi}{2} \\ \psi &= \infty \qquad \varphi = 0 \end{aligned} \tag{49}$$

Reversing the limits of integration and changing the sign we obtain finally:

$$\chi(ka) = \left(\frac{ka}{n}\right)^2 \cdot \frac{1}{1 - e^{-2n^2}} \cdot \int_0^{\frac{\pi}{2}} e^{-\frac{1}{2}\left(\frac{ka}{n \cdot \sin\psi}\right)^2} \cdot F^2\left(n, \frac{ka}{\sin\varphi}\right) \cdot \frac{d\varphi}{\sin^2\varphi} \tag{50}$$

Figures 6–8 illustrate the dependence $\theta(ka)$ and $\chi(ka)$ for both accurate (solid line) and approximate (dashed line) solutions for the values of $n = 1; 2; 3$. We see that for $n = 2$ we have practically the same results for approximate and accurate solutions — for $n = 3$ there are no differences. We see also that for $ka > 6$ and $n = 2$ the computed source has very good directivity qualities.

References

[1] M. ABRAMOWITZ, J. STEGUN, *Handbook of mathematical functions*, Dover Publications, N.Y. 1963.

[2] И. С. ГРАДШТЕИН, И. М. РИЖИК, *Таблицы интегралов*, Гос. Издат. Физ. Мат. Лит. Москва 1963.

[3] JANKE, EMDE, LOSCH, *Tables of higher functions*, McGraw Hill Book Company, N.Y. Toronto, London 1962.

[4] А. П. ПРУДНИКОВ, Ю. А. БУЧКОВ, О. И. МАРИЧЕВ, *Интегралы и ряды*, Наука, Москва 1983.

[5] W. RDZANEK, *Impedancja wzajemna i całkowita układu źródeł* [in Polish] WSP Zielona Góra, Zielona Góra 1979.

[6] R. WYRZYKOWSKI, Cz. SOŁTYS, *Obliczanie impedancji akustycznej źródeł dz'więku o znanej kierunkowości* [in Polish] Arch. Akustyki, **7**, 3–4, 327–336 (1972).

[7] R. WYRZYKOWSKI, Cz. SOŁTYS, *Własności źródła o Gaussowskim rozkładzie amplitudy prędkości drgań* [in Polish] Archiwum Akustyki, **8**, 1, 81–89 (1973).

[8] R. WYRZYKOWSKI, Cz. SOŁTYS, *Źródła dźwięku o dużej kierunkowości* [in Polish] Archiwum Akustyki, **9**, 3, 313–319 (1974)

[9] R. WYRZYKOWSKI, *The near field of sources of high directivity*, Archives of Acoustics, **15**, 3–4, 289–303 (1990).

Received on January 7, 1990